NASA CONTRACTOR REPORT

NASA CR-1639

INFLUENCE OF SUCTION ON SHOCK WAVE-TURBULENT BOUNDARY LAYER INTERACTIONS FOR TWO-DIMENSIONAL AND AXIALLY SYMMETRIC FLOWS

by William R. Seebaugh and Morris E. Childs

Prepared by
UNIVERSITY OF WASHINGTON
Seattle, Wash. 98105
for Ames Research Center

NATIONAL AERONAUTICS AND SPACE ADMINISTRATION • WASHINGTON, D. C. • SEPTEMBER 1970

1. Report No. NASA CR-1639 Calif no.	2. Government Accession No.	3. Recipient's Catalog No.
4. Title and Subtitle "INFLUENCE OF SUCTION ON SHOCK WAVE-TURBULENT BOUNDARY LAYER INTERACTIONS FOR TWO-DIMENSIONAL AND AXIALLY SYMMETRIC FLOWS."		5. Report Date September 1970 6. Performing Organization Code
7. Author(s) William R. Seebaugh and Morris E. Childs		8. Performing Organization Report No. 10. Work Unit No.
9. Performing Organization Name and Address Department of Mechanical Engineering, University of Washington, Univ. Seattle, Washington 98105		11. Contract or Grant No. NGR 48-002-047 Grant
12. Sponsoring Agency Name and Address Ames Research Center National Aeronautics and Space Administration		13. Type of Report and Period Covered Contractor Report Sept. 16, 1967-June 30, 1969 14. Sponsoring Agency Code
15. Supplementary Notes		

16. Abstract

An analytical and experimental investigation has been conducted to study interactions of conical shock waves and turbulent boundary layers representative of those occurring on the cowl surfaces of axially symmetric inlets with supersonic internal compression. The analytical method considers the effects of boundary-layer removal from the region of shock wave-boundary layer interaction. Provision was made in the experimental apparatus for suction through normal perforations located upstream of or within the regions of interaction.

In the development of the analytical model, a control volume was defined about the region of interaction, the velocity profiles upstream and downstream of the interaction region were assumed to be power laws, and the integral continuity and momentum equations were written for the control volume. For a given suction configuration, specification of a suction flow rate permitted solution for the boundary-layer thickness and power-law velocity-profile parameter downstream of the interaction region. Analytical results are presented in the form of boundary-layer thickness ratios across the interaction region and power-law parameters downstream of the interaction region.

Experimental data were obtained for adiabatic wall conditions at free-stream Mach numbers of 2.82 and 3.78, at a Reynolds number based on the upstream boundary-layer thickness of 6×10^4. Flowfield and boundary-layer properties obtained upstream of, within, and downstream of the interaction regions are presented for a number of shock-wave strengths and suction flow rates. The effects of Mach number, shock-wave strength, and suction flow rate on the occurrence of shock-induced boundary-layer separation were also investigated. The results and trends predicted by the analytical solutions are compared to the experimental data for solid- and perforated-wall cases. The limits of application of the flow models for internal flowfield analysis are delineated.

17. Key Words (Suggested by Author(s))	18. Distribution Statement
shock wave-boundary layer interaction, boundary layer suction	"Unclassified-Unlimited"

19. Security Classif. (of this report)	20. Security Classif. (of this page)	21. No. of Pages	22. Price*
Unclassified	Unclassified	142	$3.00

*For sale by the Clearinghouse for Federal Scientific and Technical Information Springfield, Virginia 22151

TABLE OF CONTENTS

LIST OF ILLUSTRATIONS

INFLUENCE OF SUCTION ON SHOCK WAVE-TURBULENT BOUNDARY LAYER INTERACTIONS FOR TWO-DIMENSIONAL AND AXIALLY SYMMETRIC FLOWS*

By William R. Seebaugh and Morris E. Childs
Department of Mechanical Engineering
University of Washington

SUMMARY

An analytical and experimental investigation has been conducted to study interactions of conical shock waves and turbulent boundary layers representative of those occurring on the cowl surfaces of axially symmetric inlets with supersonic internal compression. The analytical method considers the effects of boundary-layer removal from the region of shock wave-boundary layer interaction. Provision was made in the experimental apparatus for suction through normal perforations located upstream of or within the regions of interaction.

In the development of the analytical model, a control volume was defined about the region of interaction, the velocity profiles upstream and downstream of the interaction region were assumed to be power laws, and the integral continuity and momentum equations were written for the control volume. For a given suction configuration, specification of a suction flow rate permitted solution for the boundary-layer thickness and power-law velocity-profile parameter downstream of the interaction region. Analytical results are presented in the form of boundary-layer thickness ratios across the interaction region and power-law parameters downstream of the interaction region for a range of upstream Mach numbers, upstream profile parameters, suction flow rates, and incident shock strengths.

Experimental data were obtained for adiabatic wall conditions at free-stream Mach numbers of 2.82 and 3.78, at a Reynolds number based on the upstream boundary-layer thickness of 6×10^4. Flowfield and boundary-layer properties obtained upstream of, within, and downstream of the interaction regions are presented for a number of shock-wave strengths and suction flow rates. The effects of Mach number, shock-wave strength, and suction flow rate on the occurrence of shock-induced boundary-layer separation were also investigated.

The results and trends predicted by the analytical solutions are compared to the experimental data for solid- and perforated-wall cases. The limits of application of the flow models for internal flowfield analysis are delineated.

---

* This report is based on a dissertation submitted by William R. Seebaugh in partial fulfillment of the requirements for the degree of Doctor of Philosophy.

INTRODUCTION

When a shock wave impinges upon a turbulent boundary layer, the resulting shock wave-boundary layer interaction may have a large influence on the flow in the neighborhood and downstream of the interaction region. Shock wave-boundary layer interactions may cause disturbances of sufficient magnitude to adversely affect the performance of aerodynamic devices such as air inlets for supersonic aircraft. Suitable methods of estimating flow characteristics in the presence of such disturbances must be available to engineers responsible for the design of aerodynamic configurations on which shock wave-boundary layer interactions occur.

One objective of an aerodynamic analysis of a supersonic inlet is the prediction of the velocity and pressure distributions of the air entering the turbojet compressor or ramjet combustion chamber. These distributions are strongly affected by the boundary-layer development, which in turn is influenced by shock wave-boundary layer interactions occurring upstream. A sketch of a mixed compression supersonic inlet designed for axially symmetric flow is shown in figure 1. Shock waves impinge upon the cowl and centerbody surfaces at several locations within the inlet. Each shock wave-boundary layer interaction results in changes in the thickness of the boundary layer and in the shape of the velocity profile. The boundary layer downstream of an interaction region may be more susceptible to separation when subjected to further adverse pressure gradients, and may thicken rapidly. If the strength of an incident shock is sufficiently high, the boundary layer will separate from the surface near the shock impingement point. If not controlled, these effects may result in lower total pressure recovery and increased flow distortion.

Certain aspects of shock wave-turbulent boundary layer interactions have been studied rather extensively for two-dimensional flow with solid walls. Experimental investigations, such as that conducted by Bogdonoff and his coworkers at Princeton University (ref. 1) have defined the basic characteristics of the problem, including the effects of the strength of the incident shock wave, for a Mach number of 3.0. The pressure rise required for incipient separation of a turbulent boundary layer was investigated by Kuehn (ref. 2) for Mach numbers between 2.6 and 3.9 over a range of Reynolds numbers. The effects of shock-wave impingement on the properties of the downstream boundary layer at Mach numbers between 2.0 and 4.2 were investigated by Pinckney (ref. 3). Integral analytical solutions for the downstream boundary-layer properties were proposed by Reshotko and Tucker (ref. 4), Benson and Maslowe (ref. 5), and Kutschenreuter et al. (ref. 6).

In previous analytical investigations of boundary-layer development in axially symmetric hypersonic inlets (ref. 5, for example), it has been assumed that the ratio of boundary-layer thickness to duct radius is small and two-dimensional flow procedures have been used for all shock wave-boundary layer interaction calculations. Results of hypersonic inlet model tests at free-stream Mach numbers above about 5 (ref. 7), however, have shown that boundary layers in the throat regions of inlets with supersonic internal compression can extend completely across the duct. Relatively thick boundary layers can also be expected in small inlet test models when the freestream Reynolds numbers are much lower than those for the full-scale flight conditions, compounding the difficulty of extrapolation of test-model data. Shock wave-boundary layer interactions in axially symmetric duct flows with boundary-layer thicknesses on the order of 5 to 30 percent of the duct radius have not been considered in detail in previous investigations.

Boundary-layer control has been found to be a very effective means of obtaining higher total pressure recovery and lower flow distortion for supersonic inlet applications. Removal of a portion of the boundary layer through porous walls*, perforations* and slots, or scoops increases the pressure rise that the boundary layer can withstand without separating, reduces the thickness of the layer, and changes the shape of the velocity profile.

The influence of suction on shock wave-boundary layer interactions was investigated experimentally by Strike and Rippey (ref. 8), Kutschenreuter et al. (ref. 9), and Wainwright (ref. 10) using two-dimensional test models with various perforated-plate suction surfaces. The results of these studies indicated that separation could be eliminated by removing a sufficient portion of the boundary-layer flow; however, for references 8 and 9 the perforated plates that were used in the studies extended far upstream of the interaction region. The effects of the location of the suction surface relative to the shock-impingement point were considered in the study reported in reference 10, but quantitative results were not given. Neither analytical methods nor detailed data for suction concentrated within the interaction region were available when the present study was initiated.

The objectives of the present investigation were:

(1) To develop a method of estimating the changes in turbulent boundary-layer characteristics that occur when either a two-dimensional (oblique) shock wave or an axially symmetric (conical) shock wave impinges upon the boundary layer. The method must consider the effects of suction in the region of interaction.

---

* In this report, "porous wall" refers to a wall made of a porous material, with very small holes. The term "perforated wall," as opposed to porous wall, refers to a surface with a distribution of holes with diameters equal to a substantial fraction of the local boundary-layer thickness.

(2) To obtain experimental data describing the characteristics of shock wave-boundary-layer interactions in cases of axial symmetry with and without suction in the region of interaction.

(3) To determine if the additional adverse pressure gradients present in axially symmetric flows affect the pressure ratio at which boundary-layer separation is initially observed.

(4) To increase the level of understanding of the influence of boundary-layer suction on shock-induced separation.

SYMBOLS

C	flow-nozzle discharge coefficient
D	flow-nozzle upstream diameter
h	height
I	pressure integral
$\dot{I}_{B_x}$	momentum flux associated with suction flow
L	length of interaction region
$\dot{m}_B$	suction (bleed) mass-flow rate
$\dot{m}_{BL}$	boundary-layer mass-flow rate
M	Mach number
N_L	power-law parameter for minimum least-square error on logarithmic plot of velocity ratio versus height
N	power-law parameter for which the mass-flow rate in the boundary layer is equal to the measured mass-flow rate
P,p	static pressure
R	duct radius
Re	Reynolds number
T	temperature
U	axial velocity component
x	axial coordinate
y	radial coordinate, measured from wall
α_1	flow-deflection angle across incident shock wave (two-dimensional value for conical shock waves)
β	flow-nozzle diameter ratio
δ	boundary-layer thickness
δ^*	boundary-layer displacement thickness
γ	ratio of specific heats

Subscripts

1 upstream limit of interaction region

2 between incident and reflected shock waves

3 downstream limit of interaction region

e boundary layer edge

o wind tunnel reference condition

t total conditions

∞ freestream

ANALYSIS

Analytical Objectives

The objective of the analytical investigation is the development of a method of calculating the changes in turbulent boundary-layer characteristics that occur when either a two-dimensional (oblique) shock wave or an axially symmetric (conical) shock wave impinges upon the boundary layer. The method considers the effects of mass bleed from the region of interaction. The details of the flow fields shown in the schlieren photographs of references 1 and 3 (fig. 1) are used as a basis for the formulation of the two-dimensional flow models. For unseparated interactions, the flow external to the boundary layer is turned toward the wall by the incident shock wave. The external flow is turned back approximately parallel to the wall by the reflected shock wave, resulting in a decrease in the boundary-layer thickness across the interaction region. The Mach numbers, static pressures, and flow directions of the external flow in the region between the incident and reflected shock waves and downstream of the interaction region are approximately equal to the values obtained from the oblique shock-wave relations. The axially symmetric flow models account for the curvature of the inviscid flow streamlines between the incident and reflected shock waves.

The following requirements were considered in the formulation of the analysis of the interaction of a shock wave and a turbulent boundary layer for unseparated flow:

(1) correct representation of the geometry of the interaction region, including the boundary-layer thickness ratio, shock-wave angles, and the distance between the incident and reflected shock waves at the edge of the boundary layer,

(2) accurate prediction of the change in a boundary-layer velocity-profile parameter which is based on mass-flow equivalence,

(3) minimum dependence on empirical correlations,

(4) correct prediction of effects of moderate deviations from adiabatic wall conditions, and

(5) suitability for combination with currently available boundary-layer and inviscid flow methods.

It was a reasonable expectation that all of the above requirements could be satisfied for unseparated interactions by postulating an integral control-volume model for which the details within the interaction region were neglected and certain logical approximations to the real flow were made. Two basic configurations are considered:

(1) two-dimensional flow over a flat plate with a plane incident shock wave, and

(2) axially symmetric flow in a straight circular duct with a conical incident shock wave.

Three boundary-layer suction models were developed, in addition to the solid wall case, for each basic flow configuration:

(1) porous-wall suction, for which no x-momentum is associated with the bleed flow,

(2) perforated-wall or slot suction, in which the x-momentum associated with the suction flow is considered in the analysis, and

(3) scoop suction, involving the removal of a portion of the boundary layer by means of a scoop whose lip extends into the flow relative to the surface upstream of the scoop entrance.

Flow models and the corresponding analyses are developed in the following sections for each of the flow and suction configurations introduced above. Numerical results are presented for initial Mach numbers of 2, 3, and 4 over a range of suction flow rates and incident shock strengths. Comparisons of the analytical results and experimental data obtained concurrently and from other sources are presented in a later section.

Flow Models

Two-dimensional flow.--With consideration given to the previous description of the flow through the region of interest and the methods of analysis proposed in references 4, 5, 6 and 11, the following assumptions are made in the formulation of the two-dimensional flow models illustrated in figure 2:

(1) The boundary-layer thickness and velocity-profile shape, inviscid flow conditions, and shock-wave coordinates upstream of the interaction region are known.

(2) The boundary-layer velocity profiles at stations 1 and 3 can be approximated by power laws of the form

$$\frac{u}{u_e} = \left(\frac{y}{\delta}\right)^{\frac{1}{N}} \tag{1}$$

(3) The entrainment of mass from the external flow into the boundary layer through the region of interaction is negligible.

(4) Mass transfer across the wall between stations 1 and 3 can be taken into account by a single term in the integral continuity equation.

(5) Frictional forces are negligible through the region of interaction.

(6) The momentum transfer associated with the mass transfer across the wall can be accounted for by a single term in the integral momentum equation.

(7) The flow properties and streamline directions at the edge of the boundary layer are known from the oblique shock relations.

(8) The static pressure rise begins downstream of the point where the incident shock enters the boundary layer and the reflected shock emerges downstream of tne region of the static pressure rise.

(9) The flow just downstream of the reflected shock wave is parallel to the wall.

(10) The total temperature variation through the boundary layer is given by the Crocco relation.

Axially symmetric flow.--The flow models considered for the axially symmetric shock wave-boundary layer interaction are illustrated in figure 3. A shock wave, such as that generated by a cone at zero angle of attack, reflects from the turbulent boundary layer that is developing on the inner surface of a duct. An inviscid analysis (ref. 12) provides the theoretical point of shock impingement on the wall of the duct and the ideal static-pressure distribution at the wall (fig. 3). A continuous compression occurs downstream of the reflected shock in axially symmetric flow, whereas the pressure in this region remains constant for the corresponding two-dimensional case. The strength of the reflected shock increases with distance from the point of reflection. The pressure distributions illustrated in figure 3 are for a conical shock in uniform flow; however, the results of inviscid calculations for inlets with supersonic internal compression (ref. 12) show similar characteristics for shock-wave reflections occurring in non-uniform flow fields. The flow external to the boundary layer is

assumed to be determined from inviscid flow theory. Since the static pressure in the region between the incident and reflected shock waves is not constant for conical flow and other axially symmetric flows, the external flow streamlines are curved. With this modification, the assumptions stated for the two-dimensional flow model also apply to the axially symmetric case.

Boundary layer suction models.--The interaction region flow models for zero boundary-layer suction are shown in figures 2a and 3a, respectively, for two-dimensional and axially symmetric flow. By allowing mass to be removed from the interaction region, the same geometrical representation can be applied to the porous-wall and perforated-wall or slot suction models. For porous-wall suction, no x-momentum is associated with the suction flow. In the perforated-wall or slot suction model, it is assumed that the x-momentum flux across the control surface through the perforations or the slot is equal to the x-momentum associated with the flow in a streamtube crossing station 1 of the control volume. At station 1, this streamtube, with mass flux equal to the suction flow rate, is bounded by the wall and the appropriate streamline in the upstream boundary layer.

The scoop suction model involves the removal of a portion of the boundary layer by means of a scoop, as shown in figures 2b and 3b. It is assumed in the scoop model that the upstream x-momentum of the portion of the boundary layer captured by the scoop is removed from the interaction region. The downstream boundary-layer height is measured from the lip of the scoop, and the remainder of the wall forming the scoop is assumed to be straight.

The experimental data presented in this report indicate the presence of two reflected shock waves separated by a region of flow expansion for several of the stronger interactions. The assumptions listed above, particularly those concerning mass entrainment and the geometry of the interaction region, become less descriptive of the experimental data as the shock-wave strength increases beyond that associated with the occurrence of the additional waves. The validity of the flow models for all situations will be discussed after comparing the predicted results and the data.

Methods of Solution

In this section, a method is formulated for deriving the boundary-layer thickness and velocity-profile parameter downstream of the regions of interaction of oblique and conical shock waves with a turbulent boundary layer for each of the suction flow models described above. The general method of analysis involves an iterative solution of the integral continuity and momentum equations for the control volume. The necessary mass and momentum integrals are evaluated by a numerical integration procedure.

Detailed developments of the equations and solution procedures are given in Appendices A and B. The solutions were obtained on an IBM 7094 digital computer.

Two-dimensional flow.--For the control volume shown in figure 2, the continuity equation may be written in the form

$$\int_0^{\delta_1} \rho u dy = \int_0^{\delta_3} \rho u dy + \dot{m}_B \tag{2}$$

where $\dot{m}_B$ includes any mass transfer between stations 1 and 3, and is considered positive outward. The corresponding momentum equation is

$$p_1\delta_1 - p_3\delta_3 - p_2(\delta_1 - \delta_3) = \int_0^{\delta_3} \rho u^2 dy - \int_0^{\delta_1} \rho u^2 dy + \dot{I}_{B_x} \tag{3}$$

where $\dot{I}_{B_x}$ represents the x-momentum associated with the mass transfer $\dot{m}_B$, and is assumed positive outward. Introduction of the ideal gas equation of state and the definitions of δ^*, θ, M, etc., results in the following forms of the continuity and momentum equations:

$$\frac{\delta_1}{\delta_3} = \frac{p_3 M_{e_3} \sqrt{1 + \frac{\gamma-1}{2} M_{e_3}^2} \left(1 - \frac{\delta^*}{\delta}\right)_3}{\left(1 - \frac{\dot{m}_B}{\dot{m}_{BL}}\right) p_1 M_{e_1} \sqrt{1 + \frac{\gamma-1}{2} M_{e_1}^2} \left(1 - \frac{\delta^*}{\delta}\right)_1} \tag{4}$$

and

$$\frac{\delta_1}{\delta_3} = \frac{\frac{p_2}{p_1} - \frac{p_3}{p_1} - \gamma M_{e_3}^2 \frac{p_3}{p_1} \left(1 - \frac{\delta^*}{\delta} - \frac{\theta}{\delta}\right)_3}{\frac{p_2}{p_1} - 1 - \gamma M_{e_1}^2 \left(1 - \frac{\delta^*}{\delta} - \frac{\theta}{\delta}\right)_1 + \frac{\dot{I}_{B_x}}{p_1\delta_1}} \tag{5}$$

The term $\dot{I}_{B_x}/p_1\delta_1$ is evaluated in Appendix A for the various mass transfer configurations. This term is zero for zero suction flow and for the porous-wall suction model:

$$\left(\frac{\dot{I}_{B_x}}{p_1\delta_1}\right)_{\text{Zero suction}} = 0 \tag{6}$$

and

$$\left(\frac{\dot{I}_{B_x}}{p_1\delta_1}\right)_{\text{Porous-wall}} = 0 \tag{7}$$

The x-momentum term for perforated-wall or slot suction is given by

$$\left(\frac{\dot{I}_{B_x}}{p_1\delta_1}\right)_{\substack{\text{Perforated-wall}\\ \text{or slot}}} = \gamma M_{e_1}^2 \int_0^{\frac{y_u}{\delta_1}} \frac{\rho u^2}{\rho_{e_1} u_{e_1}^2}\, d\left(\frac{y}{\delta}\right) \tag{8}$$

where y_u/δ_1 represents the flow area (for unit width normal to the x-y plane) of the suction flow at the upstream conditions and is given by the solution of

$$\int_0^{\frac{y_u}{\delta_1}} \frac{\rho u}{\rho_{e_1} u_{e_1}}\, d\left(\frac{y}{\delta}\right) = \frac{\dot{m}_B}{\dot{m}_{BL}} \left(1 - \frac{\delta^*}{\delta}\right)_1 \tag{9}$$

The control volume for the two-dimensional scoop suction model is given in figure 2b. The governing equations are derived in Appendix A. The continuity equation is identical (4) and the momentum equation is shown to be

$$\frac{\delta_1}{\delta_3} = \frac{\frac{p_2}{p_1} - \frac{p_3}{p_1} - \gamma M_{e_3}^2 \frac{p_3}{p_1}\left(1 - \frac{\delta^*}{\delta} - \frac{\theta}{\delta}\right)_3}{\left(\frac{p_2}{p_1} - 1\right)\left(1 - \frac{y_s}{\delta_1}\right) - \gamma M_{e_1}^2 \left(1 - \frac{\delta^*}{\delta} - \frac{\theta}{\delta}\right)_1 + \frac{\dot{I}_{B_x}}{p_1\delta_1}} \tag{10}$$

The x-momentum term for scoop suction has the form

$$\left(\frac{\dot{I}_{B_x}}{p_1\delta_1}\right)_{\text{Scoop}} = \gamma M_{e_1}^2 \int_0^{\frac{y_s}{\delta_1}} \frac{\rho u^2}{\rho_{e_1} u_{e_1}^2}\, d\left(\frac{y}{\delta}\right) \tag{11}$$

where y_s/δ_1 is the non-dimensional scoop height, determined from the solution of

$$\int_0^{\frac{y_s}{\delta_1}} \frac{\rho u}{\rho_{e_1} u_{e_1}} \, d\left(\frac{y}{\delta}\right) = \frac{\dot{m}_B}{\dot{m}_{BL}} \left(1 - \frac{\delta^*}{\delta}\right)_1 \tag{12}$$

The continuity and momentum equations were solved by a successive approximation procedure after equating the right-hand sides of (4) and (5) for all cases except scoop suction, and (4) and (10) for scoop suction. Equations (A 3) and (A 4), Appendix A, are integrated numerically to relate δ^* and θ to the power-law parameter for each approximation, effectively yielding two equations in the unknowns δ_3 and N_3.

Axially symmetric flow.--The integral continuity and momentum equations for axially symmetric flow are similar to those given above for the two-dimensional case. All integrals are taken over the annular region from $r = R - \delta$ to $r = R$ (fig. 3). The cross-sectional geometry of the interaction region is similar to that for the two-dimensional flow model, except that the boundary streamline of Region 2 is generally curved. Analyses for the three mass transfer configurations are now developed for axially symmetric flow.

The continuity equation for the control volume of figure 3 has the form

$$\int_{R-\delta_1}^{R} 2\pi\rho u r dr = \int_{R-\delta_3}^{R} 2\pi\rho u r dr + \dot{m}_B \tag{13}$$

where $\dot{m}_B$ is considered positive outward. Similarly, the momentum equation becomes

$$\pi(2R\delta_1 - \delta_1^2)p_1 - \pi(2R\delta_3 - \delta_3^2)p_3 - \int_{R-\delta_1}^{R-\delta_3} 2\pi p_{e_2} \, r dr$$

$$= \int_{R-\delta_3}^{R} 2\pi\rho u^2 \, r dr - \int_{R-\delta_1}^{R} 2\pi\rho u^2 \, r dr + \dot{I}_{B_x} \tag{14}$$

where $\dot{I}_{B_x}$ is analogous to the similar term for two-dimensional flow, and where p_{e_2} is the variable pressure along the boundary streamline.

As shown in Appendix B, equations (13) and (14) are rewritten in terms of the integration variable y (fig. 3). This transformation facilitates the numerical integrations required to obtain the mass and momentum integrals from the power-law velocity-profile data. After substituting the ideal gas equation of state and the various Mach number functions, the governing equations become (Appendix B)

$$2\int_0^{\frac{\delta_1}{R}} \frac{\rho u}{\rho_{e_1} u_{e_1}} \left(1 - \frac{y}{R}\right) d\left(\frac{y}{R}\right) - \frac{2p_3 M_{e_3}}{p_1 M_{e_1}} \sqrt{\frac{1 + \frac{\gamma-1}{2} M_{e_3}^2}{1 + \frac{\gamma-1}{2} M_{e_1}^2}} \int_0^{\frac{\delta_3}{R}} \frac{\rho u}{\rho_{e_3} u_{e_3}} \left(1 - \frac{y}{R}\right) d\left(\frac{y}{R}\right) - \frac{\dot{m}_B}{\dot{m}_o} = 0 \tag{15}$$

and

$$\left[2\frac{\delta_1}{R} - \left(\frac{\delta_1}{R}\right)^2\right] - \left[2\frac{\delta_3}{R} - \left(\frac{\delta_3}{R}\right)^2\right] \frac{p_3}{p_1} - 2\int_{1-\delta_1/R}^{1-\delta_3/R} \frac{p_{e_2}}{p_1} \frac{r}{R}\, d\left(\frac{r}{R}\right)$$

$$- 2\gamma M_{e_3}^2 \frac{p_3}{p_1} \int_0^{\delta_3/R} \frac{\rho u^2}{\rho_{e_3} u_{e_3}^2} \left(1 - \frac{y}{R}\right) d\left(\frac{y}{R}\right) + 2\gamma M_{e_1}^2 \int_0^{\delta_1/R} \frac{\rho u^2}{\rho_{e_1} u_{e_1}^2} \left(1 - \frac{y}{R}\right) d\left(\frac{y}{R}\right)$$

$$- \gamma M_{e_1}^2 \frac{\dot{I}_{B_x}}{\dot{I}_o} = 0 \tag{16}$$

where the suction mass flow and the associated momentum term are referred, respectively, to the duct mass flow

$$\dot{m}_o = \rho_{e_1} u_{e_1} \pi R^2 \tag{17}$$

and the duct momentum term

$$\dot{I}_o = \rho_{e_1} u_{e_1}^2 \pi R^2 \tag{18}$$

For the two-dimensional flow model, the external pressure and Mach-number are known from the oblique shock-wave equations and are independent

of the downstream boundary-layer thickness. The analogous situation would not generally occur for axially symmetric flow, however, a flow model with a constant pressure boundary in Region 2 (fig. 3) is considered because it is useful in checking the methods that are then applied to the more general cases. The pressure integral in equation (16) is given by

$$I = 2 \int_{1-\delta_1/R}^{1-\delta_3/R} \frac{p_{e_2}}{p_1} \frac{r}{R} \, d\left(\frac{r}{R}\right) \tag{19}$$

For a straight boundary streamline with constant pressure p_2, (19) becomes

$$(I)_{\substack{\text{Constant} \\ \text{Pressure}}} = \frac{p_2}{p_1} \left[2 \frac{\delta_1}{R} - \left(\frac{\delta_1}{R}\right)^2 - 2 \frac{\delta_3}{R} + \left(\frac{\delta_3}{R}\right)^2\right] \tag{20}$$

as given in Appendix B.

When the external flow streamlines in the region between the incident and reflected shock are curved, the properties downstream of the reflected shock are initially unknown. The integral equations for the boundary layer must then be solved simultaneously with relations for the static pressure, Mach number, and flow angle along the external flow streamline at the edge of the boundary layer. The external flow properties downstream of the reflected shock are obtained using the oblique shock-wave equations, assuming that the inviscid flow immediately downstream of the reflected shock is parallel to the wall.

The necessary information for the external streamline may be determined by method-of-characteristics calculations for flows such as encountered in supersonic inlets (ref. 12). For the results that follow, the flow model illustrated in figure 3 was employed and the inviscid flow streamline data were calculated using conical flow theory.

Since the suction flow rate is specified as a fraction of the upstream boundary-layer mass flow, a conversion is necessary to give the mass flow ratio in equation (15). As shown in Appendix B,

$$\frac{\dot{m}_B}{\dot{m}_o} = 2 \left(\frac{\dot{m}_B}{\dot{m}_{BL}}\right) \int_0^{\delta_1/R} \frac{\rho u}{\rho_{e_1} u_{e_1}} \left(1 - \frac{y}{R}\right) d\left(\frac{y}{R}\right) \tag{21}$$

The term $\dot{I}_{B_x} / \dot{I}_o$ is evaluated in Appendix B for the three mass transfer models. This term is zero when $\dot{m}_B$ equals zero and also for the porous-wall suction model:

$$\left(\frac{\dot{I}_{B_x}}{\dot{I}_o}\right)_{\text{Zero Suction}} = 0 \tag{22}$$

and

$$\left(\frac{\dot{I}_{B_x}}{\dot{I}_o}\right)_{\text{Porous-wall}} = 0 \tag{23}$$

The x-momentum term for perforated-wall or slot suction is given by

$$\left(\frac{\dot{I}_{B_x}}{\dot{I}_o}\right)_{\substack{\text{Perforated-wall} \\ \text{or slot}}} = 2\int_0^{\frac{y_u}{R}} \frac{\rho u^2}{\rho_{e_1} u_{e_1}^2}\left(1 - \frac{y}{R}\right) d\left(\frac{y}{R}\right) \tag{24}$$

where y_u/R is analogous to y_u/δ_1 for two-dimensional flow and is given by the solution of

$$2\int_0^{\frac{y_u}{R}} \frac{\rho u}{\rho_{e_1} u_{e_1}}\left(1 - \frac{y}{R}\right) d\left(\frac{y}{R}\right) = \frac{\dot{m}_B}{\dot{m}_o} \tag{25}$$

The control volume used for axially symmetric scoop suction is illustrated in figure 3b. As shown, the duct radius downstream of the interaction region is reduced by an amount equal to the scoop height. Accounting for this change in duct radius, the continuity equation may be stated in the form

$$2\int_0^{\frac{\delta_1}{R}} \frac{\rho u}{\rho_{e_1} u_{e_1}}\left(1 - \frac{y}{R}\right) d\left(\frac{y}{R}\right) - 2\left(\frac{R''}{R}\right)^2 \frac{p_3 M_{e_3}}{p_1 M_{e_1}}\sqrt{\frac{1 + \frac{\gamma-1}{2} M_{e_3}^2}{1 + \frac{\gamma-1}{2} M_{e_1}^2}}\int_0^{\frac{\delta_3}{R''}} \frac{\rho u}{\rho_{e_3} u_{e_3}} \times$$

$$\left(1 - \frac{y''}{R''}\right) d\left(\frac{y''}{R''}\right) - \frac{\dot{m}_B}{\dot{m}_o} = 0 \tag{26}$$

where the suction mass-flow term is given by equation (21). The corresponding momentum equation is then

$$\left[2\frac{\delta_1}{R}-\left(\frac{\delta_1}{R}\right)^2\right]-\left[2\frac{y_s}{R}-\left(\frac{y_s}{R}\right)^2\right]-\left[2\frac{\delta_3}{R''}-\left(\frac{\delta_3}{R''}\right)^2\right]\left(\frac{R''}{R}\right)^2\frac{p_3}{p_1}-2\int_{1-\delta_1/R}^{R''/R-\delta_3/R}\frac{p_{e_2}}{p_1}\frac{r}{R}d\left(\frac{r}{R}\right)$$

(27)

$$-2\left(\frac{R''}{R}\right)^2\gamma M_{e_3}^2\frac{p_3}{p_1}\int_0^{\frac{\delta_3}{R''}}\frac{\rho u^2}{\rho_{e_3}u_{e_3}^2}\left(1-\frac{y''}{R''}\right)d\left(\frac{y''}{R''}\right)\quad+\quad 2M_{e_1}^2\int_0^{\frac{\delta_1}{R}}\frac{\rho u^2}{\rho_{e_1}u_{e_1}^2}\left(1-\frac{y}{R}\right)d\left(\frac{y}{R}\right)$$

$$-\gamma M_{e_1}^2\frac{\dot{I}_B}{\dot{I}_o}\frac{x}{} = 0 \qquad (27)$$

The x-momentum term for axially symmetric scoop suction has the form

$$\left(\frac{\dot{I}_B}{\dot{I}_o}\frac{x}{}\right)_{\substack{\text{Scoop}\\\text{Suction}}} = 2\int_0^{\frac{y_s}{R}}\frac{\rho u^2}{\rho_{e_1}u_{e_1}^2}\left(1-\frac{y}{R}\right)d\left(\frac{y}{R}\right) \qquad (28)$$

where the scoop height y_s/R is determined from the solution of

$$2\int_0^{\frac{y_s}{R}}\frac{\rho u}{\rho_{e_1}u_{e_1}}\left(1-\frac{y}{R}\right)d\left(\frac{y}{R}\right) = \frac{\dot{m}_B}{\dot{m}_o} \qquad (29)$$

The following solution procedure is employed for the interaction of a conical shock wave and a turbulent boundary layer:

(1) The Mach number, flow angle, and static pressure are calculated as functions of distance along the external flow streamline.

(2) Using oblique shock-wave theory, the Mach number and static pressure downstream of the reflected shock are calculated as functions of distance along the external flow streamline.

(3) A first approximation to the solution is obtained by solving the corresponding two-dimensional problem.

(4) The axially symmetric continuity and momentum equations are solved by a successive approximation procedure, accounting for changes in external-flow streamline properties in each calculation.

Numerical Results

In this section, parametric results obtained with the solution methods described in the previous section are presented for two-dimensional and axially symmetric shock wave-boundary layer interactions without suction. Additional results are given for the porous-wall suction, perforated-wall or slot suction, and scoop suction flow models. Mach numbers from 2.0 to 4.0 and incident shock-wave flow-deflection angles up to 11 degrees are considered. As in reference 11, a theoretical adiabatic-wall recovery factor equal to 0.896 is used in all calculations.

Two-dimensional flow.--Predictions of the boundary-layer thickness ratio δ_3/δ_1 for zero suction and a porous-suction flow rate of 0.05 times the upstream boundary-layer mass flow may be compared in figure 4a. The upstream power-law parameter N_1 is 7.0, which is representative of typical flat-plate turbulent boundary-layer velocity profiles for the Mach number range of 2.0 to 4.0 The results for δ_3/δ_1 with zero suction exhibit the correct dependence on incident shock strength (ref. 11), that is, decreasing over a range of incident shock-wave deflection angles, reaching a minimum, and then increasing for higher strength shocks. The incident shock-wave deflection angles of interest in supersonic inlet flows are generally lower than those corresponding to the minimum values of δ_3/δ_1 because of the necessity for high pressure recovery, that is, low shock strength, in the inviscid flow.

The power-law exponents (N_3) downstream of the interaction region for zero and 5 percent porous-suction flow rates are given in figure 4b for N_1 equal to 7.0. These results indicate that the use of suction increases N_3 at a given shock strength, and that an increase in shock strength causes a reduction in N_3 for all cases. The dependence of N_3 on the upstream Mach number decreases with increasing M_{e_1}.

A bleed flow rate of 5 percent of the initial mass flow is considered representative of the maximum rate that is consistent with the porous-wall suction model. Higher rates would require large bleed holes or an extended porous region upstream of the interaction region. With large bleed holes, the perforated-wall suction model provides a closer approximation to the actual

flow configuration since the x-momentum associated with suction through large holes is significant. For a configuration with an extended porous region upstream of the interaction region, modifications to the flow models of the present study to allow for mass entrainment and skin-friction effects would be necessary.

The effects of perforated-wall or slot suction on δ_3/δ_1 and N_3 are shown in figure 5 for the upstream conditions $M_{e_1} = 3$ and $N_1 = 7$. By comparing perforated-wall suction results at several suction flow rates with the predictions shown for porous-wall suction, it was determined that a suction rate of 20 percent of the upstream boundary layer was required to obtain comparable boundary-layer thickness ratios. A 20 percent bleed rate is believed to be more representative of requirements for supersonic inlet flows than lower flow rates, and the results presented here are based on this bleed rate.

The effects of scoop suction are shown in figure 6 for a suction rate equal to 20 percent of the upstream mass flow. The bleed rate for scoop suction was selected to allow a direct comparison of results with those of the perforated-wall or slot analysis.

The influence of the upstream power-law parameter on the results for two-dimensional flow was examined for the range of N_1 from 5.0 to 11.0 at constant values of $M_{e_1} = 3.0$ and $\alpha_1 = 6$ degrees. The effect of N_1 on the resulting boundary-layer thickness ratio (fig. 7a) is quite small for all flow models. The dependence of the downstream power-law parameter on N_1 is large, and nearly linear (fig. 7b).

Ratios of displacement and momentum thicknesses across the interaction region are given in figure 8 as a function of α_1 for the upstream conditions $M_{e_1} = 3.0$ and $N_1 = 7.0$. The minimum values of the integral thickness ratios occur at incident shock-wave flow-deflection angles that are lower than those for the minima of δ_3/δ_1. With no suction, the integral thickness ratios are always greater than the corresponding values of δ_3/δ_1.

The effects of the suction rate on δ_3/δ_1 and N_3 are shown in figure 9 for the two-dimensional configurations. The ratio δ_3/δ_1 decreases much more rapidly and N_3 increases much more rapidly for porous suction than for the other cases.

Ratios of displacement thickness for the three suction models are given as a function of bleed-flow fraction in figure 9. The total effective displacement of the external flow downstream of the interaction region for scoop

suction is represented by $(\delta_3^* + y_s)/\delta_1^*$. When the scoop height is included, the effective displacement of the downstream boundary layer for scoop suction is considerably greater than that for the other suction models. The effective displacement increases with increasing bleed rate and decreasing upstream Mach number. For supersonic inlet applications, the abrupt loss in flow area for the inviscid flow and the additional disturbances that may be generated at the lip of the scoop could have adverse effects, particularly if the scoop is used in the throat region of the inlet.

Axially symmetric flow.--To facilitate comparisons with predictions for the corresponding two-dimensional configurations, results for axially symmetric flow are also presented as functions of the incident shock-wave flow-deflection angle. The inviscid flow streamline at the edge of the boundary layer was calculated from conical flow theory, assuming uniform flow upstream of the incident shock wave. The correspondence between the shock-wave flow-deflection angles and cone half-angles is shown in figure 10 for the Mach numbers of interest.

The effects of the differences between two-dimensional and axially symmetric flows are illustrated in figure 11 for an upstream Mach number of 3.0 and power-law parameter equal to 7.0. The deflection angle of 3.16 degrees corresponds to the shock from a 10-degree cone at $M_{e_1} = 3.0$. The results of the analysis are given for (1) two-dimensional flow, (2) axially symmetric flow with $\delta_1/R = 0.1$ and a constant pressure boundary at the edge of the control volume, and (3) axially symmetric flow with $\delta_1/R = 0.1$ and a conical streamline boundary. The influence of the changes in mass flow per unit radius with distance from the wall is small, as shown by a comparison of results for cases (1) and (2). In contrast to this small effect, the increase in p_3/p_1 caused by the compression in the conical flow and the stronger reflected shock (case 3) results in changes of about 10 percent relative to two-dimensional predictions (case 1). The differences in interaction-region lengths for the three methods also result in changes in the position of the reflected shock wave. The analysis predicts an upstream shift in shock position relative to that obtained from inviscid theory for all cases.

The influence of the ratio of upstream boundary-layer thickness to duct radius with zero suction is shown in figure 12 for values of upstream Mach number and power-law parameter equal to 3.0 and 7.0, respectively. The combined effects of the varying overall pressure ratio p_3/p_1 and the change in flow area per unit radius with distance from the wall cause significant changes in δ_3/δ_1 and N_3 relative to the corresponding two-dimensional flows. As δ_1/R is increased, the minimum value of δ_3/δ_1 decreases and occurs at successively lower shock strengths. The influence of increasing δ_1/R is similar to that of increasing the shock strength for two-dimensional flow, and is

primarily due to the increase in the value of p_3/p_1 resulting from the compression along the conical streamline at the edge of the boundary layer and the stronger reflected shock wave.

Results for the three types of boundary-layer suction are presented in figure 13 for δ_1/R equal to 0.1. The dependence of δ_3/δ_1 on shock strength is similar for the two-dimensional and axially symmetric cases. As with two-dimensional flow, the introduction of suction causes an increase in N_3 for all axially symmetric suction configurations.

EXPERIMENTAL INVESTIGATION

Experimental Objectives

The experimental investigation described in this report was undertaken in order to obtain basic data on the interaction of a conical shock wave and a turbulent boundary layer. The experimental configuration was considered to be particularly suitable for the investigation of shock wave-boundary layer interaction phenomena because the three-dimensional secondary flows associated with the corners and sidewalls of two-dimensional wind tunnels and test models were completely eliminated. The primary emphasis was placed on the determination of differences between the present axially symmetric flow and the corresponding two-dimensional flows studied by previous investigators, and on the effects of suction on the interaction-region characteristics and the occurrence of flow separation.

Experimental results were obtained at nominal Mach numbers of 3 and 4 for a range of suction flow rates from zero to 13 percent of the initial boundary-layer mass flow. The cone angle of the shock-wave generator was varied to give a range of shock strengths corresponding to deflection angles through the incident shock waves from approximately 3 to 10 degrees.

The shock wave-boundary layer interactions generated within the present apparatus were similar to those that occur in axially symmetric inlets with supersonic internal compression, but were idealized to the extent of nearly uniform upstream flow, straight wall contours, conical incident shock waves, and a relatively simple boundary-layer suction configuration. It is believed that the results obtained in this study could be logically extended to the more general interactions that occur in inlets and other flow devices.

Description of Experimental Apparatus

The experimental apparatus was a steady flow wind tunnel that was designed specifically for the study of shock wave-boundary layer interactions in axially symmetric flow. The general configuration consisted of a transparent

plastic converging-diverging nozzle with exit diameter of 2.030 in., a conical metal centerbody, and a constant diameter transparent plastic test section (fig. 14). The contours of the axially symmetric nozzles were designed by the method of characteristics. Two nozzles with nominal exit Mach numbers of 3 and 4 were constructed. The starting properties for the characteristics calculations were obtained by specifying parabolic wall contours in the throat region and assuming conical source flow to a Mach number of 1.127 for the Mach 3 nozzle and to 1.145 for the Mach 4 design. The characteristics nets were carried out to Mach numbers of 2.94 and 3.95, respectively, for the Mach 3 and 4 nozzles.

The test sections consisted of transparent plastic tubes of constant inner diameter (2.030 in.), axial segments of which could be enclosed by an interchangeable outer ring (fig. 15). After completing the tests with solid tunnel walls, circumferential rows of 0.052- or 0.064-in. diameter bleed holes were drilled into the test section as shown. A maximum porosity of 42% over a length of 0.275 in. was obtained with 228 0.064-in. holes in four rows around the section. The slot around the outside of the section provided the volume required for the bleed plenum chamber. The lines connecting the test section to the suction flow metering and pumping system were attached to the bleed-collection ring (fig. 16).

The centerbody configuration consisted of a common rear support section with interchangeable conical tips on the upstream end. The centerbody served as the shock-wave generator and also as the forward portion of the wind-tunnel diffuser. A sharp corner was provided at the end of each cone in order to allow clear definition of the regions of the flow that were influenced by the change in body slope. The axial position of the tip of the centerbody could be changed to allow a continuous variation in the shock-impingement location on the wall. The centerbody was held at the center of the test section by four support pins located downstream of the cone base. A second set of supports at the aft end of the subsonic diffuser was used to align the centerbody axis parallel to the tunnel axis. This was accomplished by injecting colored alcohol into the nozzle through a static pressure orifice and observing the ring of liquid that formed on the wall near the beginning of the pressure rise caused by the conical shock wave. The downstream centerbody supports were adjusted until the plane of the liquid ring was normal to the tunnel axis.

The test air was supplied from an air compressor to a drying, filtering, and heating system located just upstream of the tunnel. The drier consisted of a steel tank that was filled to the desired level with a silica gel type dessicant. The drying unit could maintain the outlet air dew-point below $-75^{\circ}F$ for about 10 hours at the maximum air flow rate of 0.85 pounds a second. The dessicant was periodically regenerated by passing air heated to $350^{\circ}F$ through the tank while heating the exterior surface by means of a series of steam coils. Dessicant powder and any other solid particles were removed by a filter located on the downstream side of the drier. The air could be

heated from the supply temperature of 80°F to a maximum of 350°F by steam and electric heaters. The pressure was reduced from the supply line pressure of approximately 100 lb_f/in^2 to the desired tunnel total pressure by two regulators mounted in series in the line.

The wind-tunnel exhaust line was mounted on one port of a 150 cubic foot tank that was evacuated by four steam ejectors operating at a pressure difference of 150 lb_f/in^2. Additional vacuum capacity was provided by three pumps with a total capacity of approximately 10 ft^3/sec. The exhaust tank pressure was controlled by adjusting hand valves on the ejector air-inlet manifold and the vacuum pump inlet lines.

Instrumentation and Data Reduction

Tunnel parameters.--The tunnel total pressure was measured by means of a static pressure orifice located in the plenum chamber wall. Total pressures below 40 psig (atmospheric reference) were read on a mercury manometer, and higher values were read on a pressure gage. The maximum error in the tunnel total pressure was estimated to be about 0.7% of the reading. The tunnel plenum (total) temperature was measured with an unshielded iron-constantan thermocouple. The estimated maximum error in the total temperature measurement was 1% of the absolute temperature.

Surface static pressure.--Twenty-five 0.0135-in. diameter static-pressure orifices with spacing varying from 0.05 to 0.20 in. were installed in a single row in each test section, with a dense distribution near the theoretical shock-impingement location. Three additional pairs of orifices were located at 90-degree intervals around the circumference to aid in symmetry verification. The orifices were connected to an absolute strain-gage pressure transducer with a range of 0-10 psia by lengths of stainless steel and plastic tubing. A typical installation is illustrated in figure 17a. The output of the transducer was read on a precision null potentiometer. The same instrumentation was used for measurement of the static pressures at the inlet and throat of the suction flow metering nozzle. The maximum error for the static pressures, including potentiometer error, was about 2% of the reading.

Pitot probe surveys.--Pitot-pressure measurements were obtained using a long curved probe with a flattened tip (fig. 17b) connected to a differential strain-gage pressure transducer with a range of $\pm$ 25 psi (atmospheric reference). The transducer output was read on a potentiometer. The maximum error after conversion to absolute pressure was about 3% of the absolute reading. The probe-tip opening was 0.003-in. high and 0.017-in. wide, and the overall height of the tip of the probe was 0.008 in. (fig. 17b). Pitot pressure profiles were obtained at the centerline positions of the surface static-pressure orifices. The distance between surveys was either 0.1 or 0.2 in.

Mach numbers were calculated from the ratio of pitot pressure to surface static pressure for all points on the profiles. The distance from the wall to the freestream was defined as the transverse coordinate of the point at which the Mach number was just equal to or greater than 0.999 times the value at the next point on the profile. In a similar manner, the boundary-layer thickness δ for each profile was set equal to the coordinate at which the Mach number was just equal to or greater than 0.99 times the freestream Mach number. No interpolation between points on the profiles was performed to determine the point at exactly 0.99 M_∞ since the spacing between data points was sufficiently small (0.005 in.) to guarantee acceptable accuracy with the method used. A second value of Mach number for points outside of the boundary layer was calculated from the ratio of pitot pressure to local freestream total pressure. An estimate of the local freestream total pressure downstream of an interaction region was obtained from the product of the tunnel total pressure and the theoretical total pressure recovery across the incident and reflected shock waves. The two Mach number curves were nearly coincident outside of the boundary layer for profiles not within regions of shock wave-boundary layer interaction, indicating that the variations in static pressure across the boundary layer were small for those profiles.

Boundary-layer velocity profiles and integral properties were determined from the Mach number distributions, assuming constant static pressure and total temperature across the boundary layer. A best-fit power-law parameter, N_L, was obtained by computing the straight line of minimum least-square error on a logarithmic plot of U/U_e vs. y/δ. A second power-law parameter, N, was determined by matching the mass flow of the power-law profile to the measured value.

Boundary-layer suction flow.--The boundary-layer suction mass-flow rate was measured using a long-radius flow nozzle that was constructed according to ASME standards (ref. 13). The nozzle was calibrated in place by metering the flow with a previously calibrated square-edged orifice. The results obtained from the calibration are shown in figure 18. The total temperature of the suction flow was measured with an unshielded iron-constantan thermocouple. The nozzle used had a lower resolution limit of 0.002 lb_m/sec, and an estimated maximum error of $\pm$ 5% of the measured flow rate.

Results and Discussion

A summary of the test conditions and data obtained during the test program is given in Table I. Experimental results are presented in the form of pitot pressure surveys, surface static pressures, velocity profiles, flow field patterns determined from the analysis of the pitot pressure surveys and surface static-pressure profiles, and boundary-layer thickness and integral properties. Pitot pressure survey stations and static pressure orifice locations are identified by the distance in inches downstream of a zero reference

station 7.0 inches upstream of the entrance to the subsonic diffuser. The range of survey locations was from 2.40 to 4.21 inches.

Sample pitot pressure profiles taken in shock wave-boundary layer interaction regions are shown in figure 19. The first set of profiles (fig. 19a) gives typical results for an unseparated interaction. The upstream profile (A) shows the edge of the boundary layer (at $M_e/M_\infty = 0.99$) and the incident shock wave, which appears as a near-discontinuity about 0.01 inch thick. The shock wave is defined by a double line, with the transverse distance between the lines indicating the width of the pressure change as it appears on the pitot pressure profiles. The pitot pressure increases rapidly as the probe moves above the shock into a region of lower Mach number. The opposite situation occurs for the profiles downstream of the point of emergence of the reflected shock wave from the boundary layer. For profile B, the pitot pressure decreases as the probe moves above the shock into a higher Mach number region, increases gradually, and then decreases again through the region of increasing Mach number within the expansion originating at the cone base. The pitot pressure approaches the cone base pressure when the probe is directly behind the cone. Profile C shows the pattern obtained after the cone-base crosses the reflected shock. Profiles D and E (fig. 19b) were taken in the region immediately downstream of a separated interaction. Moving in the direction of increasing y, profile D shows a compression just outside of the boundary layer. This compression is defined by the sharp decrease in pitot pressure, corresponding to an increase in Mach number in the y-direction. The fairly rapid rise in pitot pressure indicates a decrease in Mach number in the y-direction, which corresponds to a left-running expansion originating near the edge of the boundary layer. The next decrease in pitot pressure indicates another shock wave, which is followed by the cone base expansion and wake as in profile B. The flow pattern that is constructed from profiles D and E shows two left-running shocks with an expansion between them, indicating that the flow separated and reattached further downstream. Rapid changes in the flow pattern can be defined by profiles similar to those shown in figure 19 with a spacing between profiles of about 0.1 inch.

Wind tunnel calibration.--Measurements with solid tunnel walls were made at Mach numbers of 2.82 and 3.78. Several tests were conducted without boundary-layer trips and results were compared with properties for various trip configurations. The best trip configurations, triangular vortex generators of 0.008- to 0.013-inch thickness, were used for all further tests (fig. 14). The tunnel total pressures were selected to give approximately equal values of R_{e_δ} at x=3.3 in., which was the theoretical shock-impingement point. The resulting unit Reynolds number was 5.6×10^6 ft^{-1}, and the Reynolds number based on the boundary-layer thickness of 0.138 in. (average of several tests) just upstream of the interaction region was about 6×10^4 for both Mach numbers. With a duct radius of 1.015 in., the average ratio δ_1/R was 0.136.

Transverse Mach number profiles at or near the most-forward pitot probe location for the nominal Mach 3 and 4 nozzles are shown in figure 20a. The

Mach numbers between the wall and the freestream height, denoted by h_∞, were computed from the pitot pressure and wall static pressure. The remaining distributions from h_∞ to the tunnel centerlines were determined from the ratio of pitot pressure to tunnel total pressure. The test section freestream Mach number for the nominal Mach 3 nozzle is 2.82, and the variation from this value across the entire test section is $\pm$ 0.7%. The test section Mach number for the nominal Mach 4 nozzle is 3.78, with a variation of $\pm$ 1.2%.

The axial Mach number distributions at the nozzle centerlines are given in figure 20b. The Mach numbers shown were computed from the ratio of pitot pressure to tunnel total pressure. The pitot pressures were measured by a single straight pitot tube with a 0.013-inch diameter opening. The tube was attached to the centerbody strut and the location was measured on the centerbody positioning micrometer. All distributions exhibit weak wave patterns superimposed on a trend of decreasing Mach number with axial distance. The perturbations from the mean line decrease with distance for the Mach 4 nozzle. The last point on each centerline distribution corresponds approximately to the most forward position at which a transverse pitot survey was made.

The boundary-layer Mach number profiles are shown on a large scale in figure 21. The number of points within the boundary layer is considered adequate for the integrations needed to determine integral boundary-layer properties.

Boundary-layer velocity profiles corresponding to the Mach number profiles described above are given in figure 22. The dashed lines passing through the data points correspond to the best-fit profiles with profile parameter N_L. This profile reflects the minimum least-square error on a logarithmic scale and is not required to pass through the data point at the boundary-layer edge. The solid lines represent the power-law profiles, with parameter N, giving the measured boundary-layer mass flux or displacement thickness. The close agreement between the data points and the power-law profiles indicates that the power law is a good representation of turbulent boundary-layer velocity distributions.

The boundary-layer properties for the two test sections are summarized in figure 23. Comparison of these properties shows that the boundary-layer thicknesses at M_∞ = 2.82 and 3.78 are very nearly equal. The data points given in figure 23 show that perturbations about mean trends occur in all computed parameters. These effects are primarily a result of small changes in the transverse Mach number distribution near the edge of the boundary layer caused by the weak waves identified in figure 20b. The trend of decreasing power-law parameters with axial distance reflects the slight adverse pressure gradient induced by the boundary-layer growth in the constant-area test sections. The power-law parameters are in the range between 7 and 10, indicating turbulent flow at all stations and Mach numbers.

Solid-wall interactions at $M_\infty = 2.82$.--The half angle of the conical shock-wave generator was varied from 10 to 16 degrees at Mach 2.82. The strengths of the incident shock waves correspond to flow-deflection angles from approximately 3 to 8 degrees.

Surface pressures and pitot surveys: Pitot pressure profiles taken upstream of, within, and downstream of the interaction region for a 10-degree cone at $M_\infty = 2.82$ are shown in figure 24a. The first four profiles show the edge of the boundary layer and the incident shock wave, and the reflected shock wave is clearly defined on the profiles from x = 3.50 in. through x = 4.00 in. For the profile at x = 4.00 in., the pitot pressure decreased as the probe moved above the shock wave into a region of higher Mach number, increased gradually, and then decreased again through the region of increasing Mach number within the expansion originating at the base of the cone. The expansion wave crossed the reflected shock wave on the profile at x = 4.20 in.

The wave patterns, the measured boundary-layer thickness upstream of the incident shock wave and downstream of the reflected shock wave, and the measured surface static-pressure distribution are given in figure 24b for the 10-degree cone. The pressure distribution is compared to that obtained by a method-of-characteristics calculation. The flow pattern and pressure distribution exhibit typical characteristics of a weak unseparated interaction (ref. 1). The incident and reflected shock waves are distinct and the measured surface static pressures spread about one boundary-layer thickness forward of the theoretical pressure rise.

The pressure discontinuity of the inviscid distribution, which was computed for the nominal cone angle (10 degrees), was located at the intersection of the projection of the measured incident shock wave and the wall and corresponds to a flow-deflection angle through the conical incident shock wave of 2.9 degrees. The flow-deflection angle was also determined by measuring the wave angle of the incident shock wave from the locations on the pitot profiles, and by determining the Mach number behind the shock wave with consideration given to the total pressure loss through the shock wave. The results were 2.5 and 3.5 degrees, respectively, giving an apparent uncertainty of $\pm$ 0.5 degree about the nominal value. Because of this uncertainty, the nominal shock-wave strength is used in all further descriptions and for the comparison of analytical and experimental results.

Increasing the cone half angle to 12 degrees at $M_\infty = 2.82$, with a corresponding deflection angle of 4.6 degrees, did not alter the general characteristics of the pitot-pressure profiles or the surface static-pressure distribution (fig. 25) relative to those obtained for the 10-degree cone. The ocurrence of a distinct reflected shock wave and the relatively small upstream spreading of the surface static pressures from the inviscid predictions indicate that the flow was not separated. After several hours of operation, a very thin oil ring formed on the tunnel wall just downstream of the beginning of the surface static-pressure rise, in the position illustrated in figure

25b. A similar phenomenon was observed by Chapman et al. (ref. 14) for shock wave-boundary layer interactions in two-dimensional flow. The rings could be made more distinct by injecting colored alcohol into the test section through a static pressure orifice. The liquid rings were used as a visual check on the alignment of the centerbodies within the wind tunnel. When the rings were normal to the tunnel axis, the variations in Mach number behind the incident shock waves were 0.01 or less for test profiles at several circumferential locations for a given cone angle.

The pitot-pressure profiles and interaction-region chracteristics for a 13-degree cone at $M_\infty = 2.82$ (fig. 26) are similar to those shown for the two previous cases, and again indicate attached flow at all probe locations. The flow-deflection angle for the 13-degree cone was 5.3 degrees.

Certain characteristics of separated flow are exhibited by the flow field and surface static-pressure distributions for a 14-degree cone (6.2-degree deflection angle) at $M_\infty = 2.82$ (fig. 27). The rather indistinct left-running compression leaving the boundary layer near the point of intersection of the incident shock wave and the boundary layer is believed to be a separation shock wave. The appearance of a separation shock wave is consistent with the increase in the spreading of the surface static-pressure rise to about 3.5 boundary-layer thicknesses upstream of the projected intersection of the incident shock wave and the wall. The separation shock is followed immediately by a left-running expansion that originates at the intersection of the incident shock wave and the boundary layer. The expansion is followed in turn by a relatively weak compression that corresponds to the reattachment shock wave shown in schlieren photographs of separated two-dimensional interactions (ref. 1). The separated-flow region for the 14-degree cone was apparently very small since the pitot pressure surveys did not indicate a reversed-flow region of measurable extent. The surface static-pressure distribution shows only a long region of nearly constant pressure gradient, and not the characteristic "hump" generally observed for separated two-dimensional interactions (ref. 2).

Separation is clearly identified for a 15-degree cone (7.1-degree deflection angle) at Mach 2.82 by the presence of a small region of constant pitot pressure near the wall on the profile of x = 3.20 in. (fig. 28a). There is also a hump in the wall static-pressure distribution (fig. 28b). The separation shock wave is more sharply defined than for the 14-degree cone. The reattachment wave appears on two profiles (x = 3.40 and 3.50 in.) before it crosses the strong right-running expansion from the cone base. The beginning of the surface static-pressure rise and the location of the liquid ring were at approximately the same axial station for the 14- and 15-degree cones.

Approximate separation and reattachment points were determined by plotting the Mach number variations against the axial coordinate at fixed distances from the wall (fig. 29). The intersections of lines of constant y with the M = 0 axis were cross-plotted and extrapolated to y = 0. The upstream

and downstream intersections of the extrapolated curves with the wall were identified, respectively, as the separation and reattachment points. The separated region between these points, shown on figure 28b, brackets the profile that indicates reversed flow at y = 0.005 inch (x = 3.20 in.).

The pressure ratio at the separation point, as determined by the manner described above, is somewhat higher than the corresponding pressure given by Bogdonoff (ref. 15) for two-dimensional flow. It is also evident that the hump in the static pressure distribution of figure 28 begins upstream of the indicated separation point. These results suggest that the actual separation point may be upstream of the indicated location. In addition, the lines of constant y just downstream of the separated region tend to level off and then rise rather sharply with increasing x instead of rising steadily as might be expected. This also raises a question about the reattachment location. These factors suggest that the method used to determine the length of the separated region may not be precise when the height of the separated region is of the order of the pitot probe height. The procedure of figure 29 does, however, definitely indicate the presence of a region of reversed flow.

Increasing the cone angle to 16 degrees at $M_\infty = 2.82$ resulted in additional small changes in the flow characteristics (fig. 30). The separation shock wave crosses the incident shock wave before the latter reaches the edge of the boundary layer, as clearly shown at x = 2.91 in., figure 30a. The hump in the static pressure distribution is more pronounced; however, the beginning of the separated region, determined in figure 31, does not agree with the location of the hump or the results of reference 15, again indicating the inability to precisely determine the separation and reattachment points. The liquid ring appeared at the same relative location as in the previous cases. In addition to the well-defined ring, individual liquid droplets were observed to move upstream along the wall in the separated-flow region. The deflection angle through the incident shock wave was 8.1 degrees for the 16-degree cone, which was the strongest shock wave tested at $M_\infty = 2.82$.

The surface static-pressure distributions for the Mach 2.82 interactions are summarized in figure 32. The three weakest shock waves (10-, 12-, and 13-degree cones) show rounded distributions. The distribution for the 14-degree cone corresponds to the appearance of the multiple shock-wave system characteristic of separated flow. The profiles for the highest strength shocks exhibit the humps in the pressure distributions used by Kuehn (ref. 2) to identify separated flows. The 15- and 16-degree interactions were clearly separated, even though the maximum pressure rise for each case was reduced below the level of that for the 13- and 14-degree cone by the expansion from the cone base.

Boundary-layer properties: Typical boundary-layer velocity profiles are shown in figure 33. The dashed lines passing through the data points correspond to the best-fit profiles with profile parameter N_L. This profile reflects the minimum least-square error on a logarithmic scale. The solid lines represent the power-law profiles with parameter N giving the measured

boundary-layer mass flux. The close agreement between the data points and the power-law profiles for the upstream data indicates that the power law gives a good representation of turbulent boundary-layer velocity distribution for these profiles. This agreement can be made arbitrarily close by reducing the number of points on the profile, that is, by choosing the boundary-layer edge at a lower value of M_e/M_∞. This procedure, however, results in reductions in the displacement thickness for ratios less than 0.99, indicating that 0.99 is very close to the proper value when correlations are based on displacement thickness.

The second set of profiles was obtained near the end of the interaction regions for the 10- and 16-degree cones. The profile is somewhat distorted for the 10-degree cone, but is still well-represented by the power-law profiles. For the 16-degree cone, however, the power-law profiles are less representative of the actual profile shape. This factor will be considered when evaluating the analytical methods presented in a previous section.

The third pair of profiles was obtained relatively far downstream of the interaction region for the 10-degree cone, and just downstream of reattachment for the 16-degree cone. These profiles are not similar to the upstream profiles, and have developed inflection points that cannot be represented by power laws.

The streamwise variations in measured boundary-layer properties are shown in figure 34 for the 6 cone angles at $M_\infty = 2.82$. The data points taken upstream of the interaction regions end near the projected intersections of the incident shock wave and the edge of the boundary layer. Similarly, the downstream data begin near the point of emergence of the reflected shock wave from the boundary layer. In the interest of clarity, upstream boundary-layer properties are not shown for all cases; however, the scatter shown is typical of that obtained for the six shock strengths considered. The conical flow merged continuously with the boundary layer within the interaction region and no boundary-layer properties could be defined in that interval.

The boundary layer downstream of the interaction region was not influenced by the expansion from the base of the cone for the 10- 12-, and 13-degree cones. The results for these cases indicate that the additional compression in this region retards the redevelopment of an equilibrium boundary-layer profile. The displacement and momentum thicknesses downstream of the interaction regions are larger for the large cone angles. This trend of increasing thickness parameters for high-strength shock waves was also observed for two-dimensional flow (ref. 3) as was the continued decrease in power-law parameter with increasing shock strength (fig. 34). The increase in boundary-layer mass flow across the interaction region for the weaker shock waves was approximately equal to that obtained with no shock wave (fig. 23), and increased above this value for the separated interactions. The maximum mass-flow increase was about 15 percent of the value just upstream of the interaction region.

Solid-wall interactions at $M_\infty = 3.78$.--The range of cone half angles tested at Mach 3.78 was from 8 to 15 degrees, corresponding to flow deflection angles from approximately 3 to 9 degrees. The data obtained at Mach 3.78 were similar to the results given for $M_\infty = 2.82$.

Surface pressures and pitot surveys: The pitot pressure profiles for an 8-degree cone at $M_\infty = 3.78$ (fig. 35) show a typical unseparated interaction. The nominal flow-deflection angle for this case is 2.6 degrees, indicating a rather weak shock-wave system. The lack of sharpness of the incident wave caused difficulty in measuring the shock-wave angle. The deflection angle obtained through measurement of the incident shock wave strength from the pitot pressure profiles was about 1.0 degree lower than the nominal value for this case, whereas the angle determined from the Mach number behind the shock wave was only 0.2 degree above the nominal value.

Increasing the cone half angle to 10 degrees at $M_\infty = 3.78$ (4.3-degree deflection angle) resulted in only small changes in the pitot pressures and flow field (fig. 36). The pressure rise through the reflected shock wave initially occurred in two steps (profiles at x = 3.49 and 3.59 ins.). This feature of the flow is not believed to be indicative of separated flow since the waves coalesce within a short distance and the measured surface static-pressure rise begins only about one boundary-layer thickness upstream of the projected impingement point of the incident shock wave.

As previously observed at $M_\infty = 2.82$, a flow pattern indicative of separated flow is obtained at $M_\infty = 3.78$ without the occurrence of a hump in the surface static-pressure distribution or measurable regions of constant pitot pressure. Analysis of the pitot pressure distributions for a 13-degree cone at Mach 3.78 (fig. 37a) gives the flow pattern shown in figure 37b. The separation and reattachment shocks are more clearly defined than those observed for the 14-degree cone at $M_\infty = 2.82$ (fig. 27). The static pressure rise begins about 3.3 boundary-layer thicknesses upstream of the projected intersection of the incident shock and the wall. The distribution shows a long region of nearly constant pressure gradient but no hump. The nominal flow-deflection angle through the incident shock wave was 7.2 degrees for this case.

Increasing the cone half angle to 14 degrees (8.2-degree flow deflection angle) resulted in a separated interaction, and with it, a slight hump in the surface static-pressure distribution as shown in figure 38. The pressure rise began only slightly further upstream for this case than for the 13-degree cone at $M_\infty = 3.78$. The separation and reattachment points for the 14-degree cone were determined as shown in figure 39. For this case, the indicated separation point is less than 0.1 in. downstream of the location determined using the results of reference 15.

The highest cone angle tested at $M_\infty = 3.78$ was 15 degrees, which gave a flow-deflection angle equal to 9.2 degrees (fig. 40). For a shock of this strength the static pressure distribution exhibits a more pronounced hump than for the previous cases, and the pitot pressure profiles define a larger separated flow region (fig. 41). The height of the separated region is about twice the probe height, and the indicated separation point is consistent with the location of the hump in the pressure distribution and data reported by Bogdonoff (ref. 15). Because of the small cone diameter (a result of tunnel blockage limitations) the expansion from the base of the cone reached the boundary layer very near the end of the interaction region. The pressure decrease associated with the expansion was not large enough to affect the occurrence of separation; however, the boundary-layer properties downstream of $x = 3.3$ were influenced by the interaction of the expansion with the reflected wave system and the boundary layer.

The surface static-pressure distributions obtained at $M_\infty = 3.78$, summarized in figure 42, are similar to those given for Mach 2.82 (fig. 32). The weak shocks again result in rounded distributions, and the distributions for the strongest incident waves indicate separated flow.

Boundary-layer properties: Boundary-layer profiles for the 10- and 15-degree cones at Mach 3.78 are shown in figure 43. As for $M_\infty = 2.82$, the upstream profiles and the profile near the end of the interaction region for the 10-degree case are well represented by power-law distributions, and the remainder have developed inflection points that cannot be represented by power laws.

The boundary-layer thickness and integral properties are shown as functions of streamwise distance in figure 44 for 5 cone angles at $M_\infty = 3.78$. The format for presentation is identical to that of figure 34. For the weaker shock waves (8- and 10-degree cones) the boundary layer downstream of the interaction region was not influenced by the expansion from the base of the cone. The expected increase in thickness parameters and simultaneous decrease in power-law parameter with increasing shock-wave strength were verified. For the 15-degree cone, all integral properties downstream of the interaction region were influenced by the expansion from the base of the cone. The boundary-layer mass-flow increase across the interaction region was significant only for the three highest shock strenghts, reaching a maximum of about 15 percent of the upstream value.

Oil rings were observed near the beginning of the static pressure increases for the 10-, 13-, 14-, and 15-degree cones at $M_\infty = 3.78$; however, no evidence of upstream movement of liquid within the separated flow regions was observed during the Mach 3.78 tests.

Incipient separation.--The conditions for incipient separation for two-dimensional and axially symmetric flows are compared in figure 45 in terms of the flow-deflection angles through the incident shock waves and the pressure ratios across the interaction regions. The curves for two-dimensional flow

are cross-plots of the data reported by Kuehn (ref. 2) and correspond to the overall pressure ratio existing just before the first appearance of a hump in the surface static-pressure distribution at each Reynolds number. The values of α_1 for incipient separation obtained during the present study are the deflection angles associated with the highest cone angles without separated flow at each Mach number, as indicated by the static-pressure distributions and the occurrence of regions of constant pitot pressure near the wall. The downstream pressure, p_3, is the surface static pressure at the station where the last identifiable compression wave left the edge of the boundary layer. Since the downstream end of the reflected wave system is rather indistinct, the selection of p_3 is somewhat arbitrary.

The comparisons shown in figure 45 clearly show that the boundary layer separated at lower values of α_1 for the conical shock waves. This result is attributed primarily to the larger pressure ratio across the interaction region for axially symmetric flow at a given value of α_1.

The influence of the respective test facilities and data reduction procedures on the comparisons in figure 45 should be small since the model sizes, instrumentation locations, and boundary-layer thicknesses for the two experiments were nearly identical. The boundary-layer edge Mach number was equal to 0.99 times the freestream value for both experiments, and the same methods of detecting separation were used.

Perforated-wall tests at $M_\infty = 2.82$.--Various perforation patterns were obtained by successively adding bleed holes in rows around the test section, beginning with one row of 54 0.052 in. diameter holes. The location of the incident shock wave was from 0.2 to 0.4 inch upstream from the position used in the solid-wall tests. Perforated-wall test data are presented for cone angles at which the flow was separated with zero suction.

Surface pressure and pitot surveys: A suction flow rate equal to 2.8% of the upstream boundary-layer mass flow was obtained for the 15-degree cone at $M_\infty = 2.82$ with one row of 54 0.052 in. diameter bleed holes (fig. 46). The holes were located at a cross-section where the pressure ratio was about 2.2 with zero suction, which was within the original separated region (figs. 28, 29), and the bleed plenum pressure was sufficiently low to ensure choked flow through the bleed holes. The shock-wave pattern and static pressure distribution for zero suction are shown in figure 46 by the dashed lines. The reflected shock-wave system with 2.8% suction flow was reduced somewhat in extent and displaced downstream of the location for zero suction. The initial static-pressure gradient along the surface was reduced near the beginning of the interaction region, but increased between the original separation point and the location at which the expansion from the cone base reached the wall. A hump was still present at the previously separated region, but no regions of constant pitot pressure were visible on the pitot pressure profiles. The

hump apparently was due to the bleed effects. By comparing these results to the corresponding data obtained without suction, it was concluded that the present interaction was not separated.

Using the 1 row-54 hole perforation configuration with the 16-degree cone gave a suction flow rate of 3.6% of the upstream boundary-layer flow when the bleed holes were located within the separated-flow region obtained with zero suction (fig. 47). Comparison with the results for zero suction (figs. 30, 31) shows a reduction in the streamwise extent of the interaction region and in the upstream spreading of the surface static-pressure rise. The flow does, however, appear to be slightly separated near x = 2.91 in.

A suction flow rate of 6.4% of the upstream boundary-layer flow was obtained with the 16-degree cone by using 2 rows of 54 0.052-in. diameter bleed holes located near the point of reattachment for zero suction. The flow pattern (fig. 48) is of a rather different character than for the previous cases. A very weak shock wave, attributed to the local flow disturbance introduced by the turning suction flow, originates near the bleed holes and merges with the strong reflected shock wave at x = 3.4 in. The noncoalescing shock-wave pattern observed for the previous cases has been eliminated, as has the hump in the surface static-pressure distribution. The upstream extent of the pressure rise has been reduced by about 50% relative to that obtained for zero suction. These factors indicate that the flow remained attached through the interaction region.

The influence of the suction flow-rate on the surface static-pressure distribution for the 16-degree cone is summarized in figure 49. As shown, increasing the suction rate resulted in a gradual reduction in the size of the hump, and an increase in the peak pressure reached downstream of the interaction region.

Data were obtained for an 18-degree cone at Mach 2.82 with suction flow rates of 9.7% and 13.5% of the boundary-layer mass flow upstream of the interaction regions (figs. 50 and 51, respectively). Comparison of the results for the two cases shows that the reflected shock-wave system begins further downstream and that the hump in the pressure distribution is smaller for the higher suction rate. Both interactions are separated, as indicated by the reversals in the pitot pressure readings for several profiles upstream of the suction zones, the multiple shock-wave patterns, and the humps in the static-pressure distributions.

Boundary-layer properties: Typical boundary-layer profiles obtained with suction at $M_\infty = 2.82$ are shown in figure 52. The x-coordinates for the cases with suction flow were adjusted to superimpose the incident shock waves. The profiles represent the data at an equivalent x-station downstream of the interaction region for the 16-degree cone with zero suction and with boundary-layer removal fractions of 3.6% and 6.4%. Increasing the suction rate from zero results in a progressive decrease in boundary-layer thickness accompanied

by an increase in the fullness of the velocity profile. These changes are also reflected in reductions in displacement and momentum thicknesses (fig. 53), and in the mass flow contained within the boundary layer.

Perforated-wall tests at $M_\infty = 3.78$.--Test data with perforated walls were obtained at Mach 3.78 for one initially attached flow (10-degree cone) and one initially separated configuration (15-degree cone).

Surface pressures and pitot surveys: Pitot pressure profiles for the 10-degree cone at Mach 3.78 with a bleed flow rate equal to 3.6% of the upstream boundary-layer mass flow are presented in figure 54a. A row of 54 0.064-inch diameter holes followed by a second row of 58 0.052-inch diameter holes formed the bleed hole pattern (fig. 54b). The bleed holes were choked for this case. The centerbody was positioned so that the bleed holes were at a position where the average pressure ratio was about 2.0.

The disturbances introduced by the bleed flow are visible on the profiles from $x = 2.90$ to 3.49. They coalesce with the downstream shock wave near $x = 3.59$. The only discernible difference between the present flow field and that of the zero-suction case was the reduction of the spreading of the downstream or reflected shock wave.

Significant changes in all aspects of the flow field and boundary-layer properties relative to the previous cases for the 10-degree cone at $M_\infty = 3.78$ were obtained with a bleed flow rate equal to 8.5 percent of the upstream boundary-layer mass flow. This flow rate was obtained with 4 rows of 0.064-inch diameter holes (total of 228 holes), giving the maximum porosity of 42 percent over the 0.275 inch long bleed zone (fig. 55). The pitot profiles indicate that the disturbances from the bleed holes coalesced into a weak shock wave that merged with the reflected shock wave just outside of the boundary layer. As shown in figure 55b, removal of 8.5 percent of the boundary-layer mass flow resulted in the appearance of a hump in the surface static-pressure distribution of the type observed for separated flows without suction. The first row of holes was not choked, but the bleed plenum pressure was sufficiently lower than the local static pressure at the bleed hole inlets to guarantee that no recirculation into the test section occurred. The condition obtained for this case represents the maximum possible bleed flow rate attainable with no bleed flow recirculation for the 10-degree cone at $M_\infty = 3.78$ since any further increase in the number of bleed perforations would have resulted in a bleed plenum pressure greater than the test section internal pressure over the bleed zone.

A summary of the surface static-pressure distributions with various perforation configurations for a 10-degree cone at $M_\infty = 3.78$ is presented in figure 56. Profile 340 was obtained with a solid wall. The perforated-wall cases show humps in the distributions of the type that have been used in the past to identify separated flows. The size of the hump in the profiles

increased with increasing suction rate. With this exception, the characteristics of the distributions were not strongly affected by the suction flow rate.

A suction flow rate equal to 3.1% of the upstream boundary-layer mass flow was obtained for the 15-degree cone at $M_\infty = 3.78$ with one row of 54 0.064-in. diameter bleed holes. The bleed holes were located at a cross-section where the pressure ratio was about 2.7 and the bleed plenum pressure was sufficiently low to ensure choked flow through the bleed holes. The pitot pressure profiles (fig. 57a) and surface static-pressure distribution (fig. 57b) indicate that the flow remained attached through the interaction region, whereas the flow was separated at the same conditions with zero suction. The multiple shock-wave pattern of the zero suction case (shown as dashed lines) was reduced to a single reflected shock wave similar to that obtained for unseparated interactions without suction, and the upstream spreading of the surface static-pressure rise was reduced by about 40%. When suction was applied for the 15-degree cone, the reduction in the boundary-layer thickness relative to the solid-wall case allowed the expansion from the base of the cone to pass downstream of the intersection of the reflected shock wave and the boundary-layer edge. The influence of the expansion on the flow pattern and boundary-layer properties immediately downstream of the interaction region is, therefore, believed to be negligible for the perforated-wall tests.

Removal of 5.2% of the upstream boundary-layer flow causes further changes in the flow field for the 15-degree cone at $M_\infty = 3.78$, as shown in figure 58. Two rows of bleed holes formed the perforation pattern, and the holes were choked during the test. The upstream influence, as reflected by the surface static-pressure distribution, was somewhat lower than that observed for 3.1% suction.

A maximum suction flow of 13.1% of the upstream boundary-layer mass flow was obtained with the 15-degree cone and a 4-row 42% porosity perforation configuration of 0.064-in. diameter holes. The bleed plenum pressure was not low enough to choke the upstream holes but in view of the observed values of wall static and bleed plenum pressures it is highly unlikely that recirculation occurred from the plenum into the low-pressure region of the test section. The flow pattern (fig. 59) shows an additional shock wave, originating near the upstream bleed holes, and a rather thin boundary-layer downstream of the interaction region. The upstream spreading of the surface static-pressure rise was reduced to 50% of that for zero suction.

The effects of suction rate on the surface static-pressure distribution, shown in figure 60, are more pronounced for the 15-degree than for the 10-degree cone. The solid-wall (334) case represents a separated interaction. A suction rate of 2.5% of the upstream boundary layer (319) apparently was sufficient to attach the flow when the bleed zone (26 0.064-inch holes) was within the interaction region. The peak pressure increased with increasing

suction rate in the lower range (0 to 5.2%), and then began to decrease at the highest rate tested (405, 13.1%).

The effect of the location of the bleed zone relative to the incident shock wave was studied by translating the centerbody. Results of static pressure measurements at $M_\infty = 3.78$ for bleed upstream of the pressure rise induced by a 15-degree cone-shock wave are given in figure 61. The flow appeared to remain attached for 3.6% bleed. This rate is comparable to the rates obtained for attached flow with suction within the interaction region (fig. 60); however, when the bleed zone was upstream of the interaction region approximately 4 times as many holes were required to realize the suction flow rate obtained with 1 row of holes at a pressure ratio of about 2.0. It is evident from these results that suction within the interaction region would be more effective for supersonic inlet applications when the problem of removal of the low-pressure bleed flow is considered. The results of tests of a high-performance axially symmetric inlet (ref. 16) also show that suction within regions of shock wave-boundary layer interaction yields better inlet performance than suction ahead of shock-impingement locations.

Boundary-layer properties: Representative boundary-layer velocity profiles downstream of the interaction region for the 10-degree cone with and without suction are shown in figure 62. Removal of 3.6% of the boundary-layer mass flow resulted in insignificant changes in the thickness and velocity-profile shape relative to the solid-wall case. Increasing the suction flow rate to 8.5% resulted in a reduction in boundary-layer thickness with a corresponding increase in the fullness of the profile.

The displacement thickness and momentum thickness downstream of the interaction region for 8.5% suction were considerably smaller than the values for zero or 3.6% suction (fig. 63). The values of N for power-law profiles were correspondingly higher for the higher suction flow rate. The boundary-layer mass flow was reduced by an amount approximately equal to the suction rate; however, the rate of boundary-layer growth downstream of the interaction region was not changed.

Additional velocity profiles are shown in figure 64 for the 15-degree cone. Increasing the suction rate resulted in progressive reductions in boundary-layer thickness. The boundary-layer properties downstream of the interaction region for the 15-degree cone with and without suction may be compared in figure 65. The results with 3.1% suction indicate a significant improvement, in terms of reduced δ and increased N, in the characteristics of the boundary-layer relative to the separated zero-suction case. The differences decreased rapidly with distance, however, as the expansion from the base of the cone caused the flow to accelerate. The presence of the expansion also makes a comparison of the difference in mass-flow rates determined from the upstream and downstream profiles to the measured value rather difficult. Additional improvements in the boundary-layer characteristics downstream of the interaction region were obtained by increasing the suction flow rate.

COMPARISON OF THEORY AND EXPERIMENT

The results of the analysis developed during the present study are compared to data obtained by Pinckney (ref. 3) for two-dimensional interactions with solid walls, and to the data presented in this report for axially symmetric flow with solid and perforated walls.

Two-Dimensional Flow

Detailed experimental information on the effects of suction on the changes in boundary-layer properties across the region of interaction with an oblique shock wave is not currently available for any of the suction models discussed in this report.

The results of calculations for a two-dimensional interaction with a solid wall are compared with experimental data reported by Pinckney (ref. 3) in figure 66. The experimental shock-wave positions were taken from a schlieren photograph. The shock-wave generator angle was given as 6 degrees; however, the peak surface static-pressure rise corresponds to an effective flow-deflection angle of about 7 degrees. Since the analytical method is more sensitive to pressure ratio than shock-wave angle, $\alpha_1 = 7$ degrees was used for the comparison. The schlieren photograph and surface static-pressure distribution indicate that the flow was not separated. The boundary-layer characteristics downstream of the reflected shock wave are given at two stations, as shown in figure 66. The point of emergence of the reflected shock wave from the boundary layer could not be determined accurately. For this reason, the analytical results and experimental data are compared by linearly extrapolating the experimental values of δ_3/δ_1 and N_3 to the theoretical reflected shock-wave position (station 3, fig. 2a). The predicted results for δ_3/δ_1 and N_3 are within 8 percent of the extrapolated experimental data.

The possibility of influences of mass entrainment and the attendant momentum transfer on the results for two-dimensional flow without suction were examined for the case shown in figure 66. From the experimental results reported in reference 3, an increase in boundary-layer mass flow equal to about 4% of the upstream value was obtained. A flow model with mass addition and momentum transfer, assumed to occur across the upper control surface (fig. 2a), was postulated. The continuity and momentum equations, Equations (3) and (4), apply to this flow model when the mass term $m_B/\dot{m}_{BL}$ is negative, the momentum term $\dot{I}_{B_x}/p_1\delta_1$ is given by (A 24) of Appendix A, and the pressure-area term for region 2 is assumed to equal the value for zero mass addition. Calculations for the upstream data corresponding to figure 66 with 4% mass addition indicate that δ_3/δ_1 increased by about 2% and N_3 increased by about 6%. Changes of this magnitude are within the uncertainty of the data and it is concluded

that inclusion of the effects of entrainment from the external flow is not required for the weak interaction considered here.

Additional comparisons to the data obtained by Pinckney (ref. 3) are summarized in figure 67. The circular symbols represent the thickness ratios obtained by extrapolating the downstream boundary-layer thickness to station 3 of the theoretical flow model (fig. 2a). The solid lines were calculated by the present theory. As shown, the agreement between the theoretical predictions and the extrapolated data is excellent for Mach 3.02 and reasonable for Mach 1.99. The downstream data points for Mach 4.24 were obtained at relatively large distances from station 3, and the extrapolation procedure appears to be the cause of the relatively poor agreement.

Axially Symmetric Flow

Solid-wall interactions.--Analytical results for a 10-degree cone at Mach 3.78 with zero suction are compared to experimental data in figure 68. The experimental incident and reflected shock waves appear as bands of finite width, and the occurrence of a single reflected shock wave indicates that the flow was not separated. The predicted interaction length is somewhat larger than that determined experimentally. The predicted thickness downstream of the interaction is about 8 percent lower than the measured value, and the theoretical power-law parameter is about 20 percent above the experimental result. The analysis predicts the slope of the reflected shock wave as it leaves the edge of the boundary layer. This slope is indicated by the solid line on figure 68.

The results of analytical calculations are compared to solid-wall experimental data in figure 69 for Mach 2.82 and figure 70 for Mach 3.78. The theoretical curves were determined using average values of the upstream boundary-layer thickness and mass-flow equivalent power-law parameter for all data obtained at both Mach numbers. The points to the left of the vertical dashed lines represent unseparated flows, whereas the remaining flows for each Mach number exhibited characteristics of separated interactions with the accompanying upstream spreading of the surface static-pressure rise.

The agreement between the analytical and experimental results is considered to be good (within 20%) for the unseparated interactions for which the analytical flow models were derived. As shown in figures 69 and 70, the differences between analysis and experiment increase markedly with increasing shock strength when the experimental data exhibit characteristics indicative of separated flow. For these cases, the assumed geometry of the flow model is no longer similar to the actual interaction. The pressure-area term in the momentum equation, equation (14), does not account for the multiple-wave reflected shock system when a conical streamline boundary is specified in the analysis. The assumption of negligible mass entrainment is not entirely valid for the stronger interactions, as evidenced by the mass-flow increases shown in figures 34 and 44. Proper accounting for mass-entrainment effects is

difficult partly because of the influence of the data-reduction procedure, that is, the choice of the edge of the boundary layer at $M_e/M_\infty = 0.99$ downstream of a strong interaction where the profiles are highly distorted. The influence of the other assumptions used in the analysis is considered to be of less importance than those concerning the geometry of the interaction region and mass entrainment.

Perforated-wall interactions.--Comparisons of predictions for the perforated-wall or slot suction flow model and experimental data for the 15- and 16-degree cones at Mach 2.82 are shown in figures 71 and 72, respectively. The upstream properties for the analytical results correspond to the average values obtained for all cases at Mach 2.82 with zero suction. The agreement between analysis and experiment for the 15-degree cone is rather poor; however, one case was separated and the other was very near separation so that the patterns do not correspond closely to the flow models used in the analysis. With the exception of N_3, the agreement for the boundary-layer properties improves with increasing suction flow rate for the 16-degree cone. The flow was attached throughout the interaction region for 6.4% suction, and the upstream spreading of the surface static-pressure rise was reduced to such an extent that the flow model of the analysis more closely describes the flow pattern obtained experimentally. The agreement was good for the external flow parameter M_3 over the range of suction rates tested for both 15- and 16-degree cones.

Similar comparisons are shown in figure 73 for the 10-degree cone at Mach 3.78. All experimental data represent attached flows for which the flow model and experimental flow field have a similar structure. Removal of 3.6% of the boundary-layer mass flow did not change the properties downstream of the interaction region. At the higher suction rate (8.5%), significant reductions in the downstream thicknesses were realized. The agreement between analysis and experiment for all boundary-layer properties improves with increasing suction flow rate.

The most extensive comparisons between predictions and experimental data were made for the 15-degree cone at Mach 3.78. These comparisons are shown in figure 74. Removal of 3.1% of the boundary-layer mass flow prevented separation but did not completely eliminate the upstream spreading of the surfaces static-pressure rise. At higher suction rates, the analytical flow model more closely describes the flow patterns obtained experimentally and the agreement is excellent.

CONCLUDING REMARKS

The results presented in this report support the following conclusions:

(1) The additional adverse pressure gradients present in axially symmetric flows reduced the shock wave strength at which separation was initially observed relative to results for two-dimensional flow, as reported by Kuehn (ref. 2). The identification of a "hump" in the surface static-pressure distribution did not appear to be a reliable indication of completely attached flow for the present tests since in some instances characteristics indicative of separated flow with important changes in the flow pattern were observed before the appearance of a hump in the pressure distribution, while in some unseparated flows with boundary-layer bleed the pressure distribution exhibited a hump.

(2) The observable effects of separation may be completely eliminated for separations as long as two boundary-layer thicknesses in extent by removing a small portion of the boundary-layer mass flow from the interaction region.

(3) The power-law velocity profile was found to provide a good representation of the measured boundary-layer velocity distributions upstream of the incident shock waves and immediately downstream of the interaction regions for unseparated interactions. The analytical predictions are in good agreement with the experimental results for interactions without extensive upstream spreading of the surface static-pressure rise.

(4) Suction within the interaction region was more effective in suppressing the effects of separation for supersonic inlet applications than suction ahead of the shock impingement location when the problem of removal of the low-pressure suction flow was considered. This is in agreement with the discussion of reference 10, but not with the conclusions reached by Strike and Rippey (ref. 8). The observations of the present study regarding the location of bleed perforations are also supported by the results of tests of a high-performance axially symmetric inlet (ref. 16).

APPENDIX A

Analysis for Two-Dimensional Flow

The equations for the two-dimensional shock wave-boundary layer interaction without mass or momentum transfer are given in references 5 and 6. Similar equations are derived here for interactions with mass transfer and momentum transfer due to mass transfer.

Consider the application of the principles of conservation of mass and momentum to the control volume of figure 2. Including any mass transfer between station 1 and station 3 in the term $\dot{m}_B$, which is considered positive outward, application of the principle of conservation of mass gives

$$\int_o^{\delta_1} \rho u dy = \int_o^{\delta_3} \rho u dy + \dot{m}_B \tag{A 1}$$

Similarly, application of the principle of conservation of momentum to the same control volume gives

$$p_1\delta_1 - p_3\delta_3 - p_2(\delta_1-\delta_3) = \int_o^{\delta_3} \rho u^2 dy - \int_o^{\delta_1} \rho u^2 dy + \dot{I}_{B_x} \tag{A 2}$$

where the term $\dot{I}_{B_x}$ represents the x-momentum associated with the mass transfer $\dot{m}_B$, assumed positive outward, and the wall shear force has been neglected.

The boundary-layer displacement thickness is given by

$$\delta^* \equiv \int_o^{\delta} \left(1 - \frac{\rho u}{\rho_e u_e}\right) dy \tag{A 3}$$

and the momentum thickness by

$$\theta \equiv \int_o^{\delta} \frac{\rho u}{\rho_e u_e} \left(1 - \frac{u}{u_e}\right) dy \tag{A 4}$$

where the subscript e refers to the local boundary-layer edge conditions.

Rearrangement of (A 3) and (A 4) gives

$$\int_0^{\delta} \rho u dy = \rho_e u_e \ (\delta - \delta^*) \tag{A 5}$$

and

$$\int_0^{\delta} \rho u^2 dy = \rho_e u^2{}_e \ (\delta - \delta^* - \theta) \tag{A 6}$$

Introducing the ideal-gas equation of state, the Mach number, and the total temperature, and assuming constant static pressure through the boundary layer, the density-velocity terms become

$$\rho_e u_e = p M_e \sqrt{\frac{\gamma}{R T_{t_e}}} \sqrt{1 + \frac{\gamma - 1}{2} M_e^2} \tag{A 7}$$

and

$$\rho_e u^2{}_e = \gamma p M^2{}_e \tag{A 8}$$

The initial boundary-layer mass flux is denoted by $\dot{m}_{BL}$:

$$\dot{m}_{BL} = \int_0^{\delta_1} \rho u dy \tag{A 9}$$

Rearranging (A 1) and substituting this definition

$$1 - \frac{\dot{m}_B}{\dot{m}_{BL}} = \frac{\int_0^{\delta_3} \rho u dy}{\int_0^{\delta_1} \rho u dy} \tag{A 10}$$

Substituting (A 5) and (A 7) into (A 10)

$$1 - \frac{\dot{m}_B}{\dot{m}_{BL}} = \frac{p_e M_{e_3} \sqrt{\frac{\gamma}{RT_{t_3}}} \sqrt{1 + \frac{\gamma-1}{2} M^2_{e_3}} \, (\delta_3 - \delta^*_3)}{p_1 M_{e_1} \sqrt{\frac{\gamma}{RT_{t_1}}} \sqrt{1 + \frac{\gamma-1}{2} M^2_{e_1}} \, (\delta_1 - \delta_1^*)}$$

Assuming that the total temperature along the boundary-layer edge is constant, and rearranging

$$\frac{\delta_1}{\delta_3} = \left(\frac{1}{1 - \frac{\dot{m}_B}{\dot{m}_{BL}}}\right) \frac{p_3 M_{e_3} \sqrt{1 + \frac{\gamma-1}{2} M^2_{e_3}} \, (1 - \frac{\delta^*}{\delta})_3}{p_1 M_{e_1} \sqrt{1 + \frac{\gamma-1}{2} M^2_{e_1}} \, (1 - \frac{\delta^*}{\delta})_1} \qquad \text{(A 11)}$$

which is the desired continuity equation as given in the text.

Dividing (A 2) by $p_1\delta_3$ and rearranging

$$\frac{p_2\delta_1}{p_1\delta_3} - \frac{\delta_1}{\delta_3} - \frac{1}{p_1\delta_3}\int_o^{\delta_1} \rho u^2 dy + \frac{\dot{I}_{B_x}}{p_1\delta_3} = \frac{p_2}{p_1} - \frac{p_3}{p_1} - \frac{1}{p_1\delta_3}\int_o^{\delta_3} \rho u^2 dy$$

Substituting (A 6) and (A 8) and rearranging further

$$\frac{\delta_1}{\delta_3} = \frac{\frac{p_2}{p_1} - \frac{p_3}{p_1} - \gamma M^2_{e_3} \frac{p_3}{p_1} (1 - \frac{\delta^*}{\delta} - \frac{\theta}{\delta})_3}{\frac{p_2}{p_1} - 1 - \gamma M^2_{e_1} (1 - \frac{\delta^*}{\delta} - \frac{\theta}{\delta})_1 + \frac{\dot{I}_{B_x}}{p_1\delta_1}} \qquad \text{(A 12)}$$

which is the desired momentum equation as given in the text. The term $\dot{I}_{B_x}/p_1\delta_1$ is now evaluated for several mass transfer configurations.

Porous-wall suction. -- For the case of mass removal by suction through a porous wall, the transfer of x-momentum across the control surface is zero and

$$\left(\frac{\dot{I}_{B_x}}{p_1 \delta_1}\right)_{\text{Porous-wall}} = 0 \tag{A 13}$$

Perforated-wall of slot suction. -- For the case of mass removal by suction through a series of perforations or a slot, the x-momentum transferred across the control surface (positive outward by convention) is set equal to the x-momentum associated with the suction flow at station 1:

$$\dot{I}_{B_x} = \int_0^{y_u} \rho u^2 dy$$

where y_u is the distance defined by

$$\dot{m}_B = \int_0^{y_u} \rho u dy$$

Then, with (A 9) and (A 5), the above equation becomes

$$\int_0^{y_{u/\delta_1}} \frac{\rho u}{\rho_{e_1} u_{e_1}} d\left(\frac{y}{\delta}\right) = \frac{\dot{m}_B}{m_{BL}} \left(1 - \frac{\delta^*}{\delta}\right)_1 \tag{A 14}$$

The non-dimensional momentum flux term then becomes, with (A 8)

$$\left(\frac{\dot{I}_{B_x}}{p_1 \delta_1}\right)_{\substack{\text{Perforated-Wall} \\ \text{or Slot}}} = \gamma M^2_{e_1} \int_0^{y_{u/\delta_1}} \frac{\rho u^2}{\rho_{e_1} u^2_{e_1}} d\left(\frac{y}{\delta}\right) \tag{A 15}$$

where y_u/δ_1 is determined from the solution of (A 14).

The perforated-wall or slot suction model was initially derived for the slot geometry shown by the dashed lines in figure 2a, and the x-momentum flux across the control surface (A 15) was calculated for this geometry. This flow model is also applied to perforated walls with holes normal to the surface when the hole diameter is a substantial fraction of the boundary-layer thickness. For such large perforations, the x-momentum flux associated with the

suction flow is considered to be significant and of the same order of magnitude as that associated with the slot shown in figure 2a.

Scoop suction. -- The control volume for the scoop suction model is somewhat different than for the previous cases and is illustrated in figure 2b. The continuity equation for scoop suction is given by

$$\int_0^{\delta_1} \rho u dy - \int_0^{y_s} \rho u dy = \int_0^{\delta_3} \rho u dy' \tag{A 16}$$

and the momentum equation is

$$p_1(\delta_1 - y_s) - p_2(\delta_1 - \delta_3 - y_s) - p_3\delta_3 = \int_0^{\delta_3} \rho u^2 dy' - \int_{y_s}^{\delta_1} \rho u^2 dy \tag{A 17}$$

Defining the suction mass-flow fraction, as for the previous models,

$$\frac{\dot{m}_B}{\dot{m}_{BL}} = \frac{\int_0^{y_s} \rho u dy}{\int_0^{\delta_1} \rho u dy} \tag{A 18}$$

Substitution of the definitions of δ^*, θ, etc. and rearrangement give

$$\frac{\delta_1}{\delta_3} = \left(\frac{1}{1 - \frac{\dot{m}_B}{\dot{m}_{BL}}}\right) \frac{p_3 M_{e_3} \sqrt{1 + \frac{\gamma-1}{2} M^2_{e_3}} \left(1 - \frac{\delta^*}{\delta}\right)_3}{p_1 M_{e_1} \sqrt{1 + \frac{\gamma-1}{2} M^2_{e_1}} \left(1 - \frac{\delta^*}{\delta}\right)_1} \tag{A 19}$$

which is identical to (A 11).

After dividing by $p_1\delta_3$ and rearranging, (A 17) becomes

$$\frac{p_2}{p_1}\frac{\delta_1}{\delta_3} - \frac{\delta_1}{\delta_3} - \frac{p_2}{p_1}\frac{y_s}{\delta_1}\frac{\delta_1}{\delta_3} + \frac{y_s}{\delta_1}\frac{\delta_1}{\delta_3} - \frac{1}{p_1\delta_3}\int_{y_s}^{\delta_1} \rho u^2 dy = \frac{p_2}{p_1} - \frac{p_3}{p_1} - \frac{1}{p_1\delta_3}\int_0^{\delta_3} \rho u^2 dy'$$

The integral on the left-hand side may be written

$$\int_{y_s}^{\delta_1} \rho u^2 dy = \int_{o}^{\delta_1} \rho u^2 dy - \int_{o}^{y_s} \rho u^2 dy$$

Combination with (A 6) and (A 8) and further rearrangement give

$$\frac{\delta_1}{\delta_3} = \frac{\frac{p_2}{p_1} - \frac{p_3}{p_1} - \gamma M^2_{e_3} \frac{p_3}{p_1} \left(1 - \frac{\delta^*}{\delta} - \frac{\theta}{\delta}\right)_3}{\left(\frac{p_2}{p_1} - 1\right)\left(1 - \frac{y_s}{\delta_1}\right) - \gamma M^2_{e_1} \left(1 - \frac{\delta^*}{\delta} - \frac{\theta}{\delta}\right)_1 + \frac{\dot{I}_{B_x}}{p_1 \delta_1}} \qquad \text{(A 20)}$$

where the x-momentum flux term has the form

$$\left(\frac{\dot{I}_{B_x}}{p_1 \delta_1}\right)_{Scoop} = \gamma M^2_{e_1} \int_{o}^{y_s/\delta_1} \frac{\rho u^2}{\rho_{e_1} u^2_{e_1}} d\left(\frac{y}{\delta}\right) \qquad \text{(A 21)}$$

where y_s/δ_1 is determined from the solution of (A 18), which may be rewritten in the form of (A 14) to give

$$\int_{o}^{y_s/\delta_1} \frac{\rho u}{\rho_{e_1} u_{e_1}} d\left(\frac{y}{\delta}\right) = \frac{\dot{m}_B}{\dot{m}_{BL}} \left(1 - \frac{\delta^*}{\delta}\right)_1 \qquad \text{(A 22)}$$

Mass addition from region 2 external flow. -- It has been observed experimentally (ref. 11) that some mass transfer into the boundary layer occurs in the region between the incident and reflected shock waves (region 2, fig. 2). Assuming that the external flow conditions are not affected by this mass transfer, the associated x-momentum transfer term is given by

$$\dot{I}_{B_x} = \dot{m}_B u_2 \cos \alpha_2 = \frac{\dot{m}_B}{\dot{m}_{BL}} \dot{m}_{BL} u_2 \cos \alpha_2 \qquad \text{(A 23)}$$

where α_2 is the flow direction angle in region 2.

Then, with (A 5), (A 7), and (A 9), the desired term becomes

$$\left(\frac{\dot{I}_B}{p_1 \delta_1 x}\right)_{\text{Region 2}} = \frac{\dot{m}_B}{\dot{m}_{BL}} \left(1 - \frac{\delta^*}{\delta}\right)_1 \gamma M_{e_1} M_{e_2} \cos \alpha_2 \sqrt{\frac{1 + \frac{\gamma-1}{2} M_{e_1}^2}{1 + \frac{\gamma-1}{2} M_{e_2}^2}} \qquad \text{(A 24)}$$

Interaction-region length. -- For zero bleed, porous-wall suction, and perforated-wall or slot suction, the length of the interaction region and the position of the reflected shock wave can be determined directly from the geometry (fig. 2):

$$\tan \alpha_1 = \frac{\delta_1 - \delta_3}{L}$$

Thus

$$L = \frac{\delta_1 - \delta_3}{\tan \alpha_1}$$

or

$$\frac{L}{\delta_1} = \frac{1}{\tan \alpha_1} \left(1 - \frac{\delta_3}{\delta_1}\right) \qquad \text{(A 25)}$$

Similarly, for scoop suction,

$$\frac{L}{\delta_1} = \frac{1}{\tan \alpha_1} \left(1 - \frac{\delta_3}{\delta_1} - \frac{y_s}{\delta_1}\right) \qquad \text{(A 26)}$$

APPENDIX B

Analysis for Axially Symmetric Flow

The integral continuity and momentum equations for axially symmetric flow are similar to those given in Appendix A for two-dimensional flow. All integrals are taken over the annular region from $r = R-\delta$ to $r = R$ (fig. 3). The cross-sectional geometry of the interaction region is similar to that for two-dimensional flow, except that the boundary streamline of region 2 is generally curved.

Application of the principle of conservation of mass to the annular control volume of figure 3 gives

$$\int_{R-\delta_1}^{R} 2\pi\rho u r dr = \int_{R-\delta_3}^{R} 2\pi\rho u r dr + \dot{m}_B \tag{B 1}$$

where $\dot{m}_B$ is positive out of the control volume.

Similarly, the momentum equation becomes

$$\pi(2R\delta_1-\delta_1^2)\, p_1 - \pi(2R\delta_3-\delta_3^2)\, p_3 - \int_{R-\delta_1}^{R-\delta_3} 2\pi p_{e_2} r dr = \int_{R-\delta_3}^{R} 2\pi\rho u^2 r dr - \int_{R-\delta_1}^{R} 2\pi\rho u^2 r dr + \dot{I}_{B_x} \tag{B 2}$$

where $\dot{I}_{B_x}$ represents the x-momentum associated with $\dot{m}_B$ (positive outward) and p_{e_2} is the pressure along the streamline boundary, which may be variable.

Consider the general integral term

$$\int_{R-\delta}^{R} f(\rho,u)\, r dr$$

and the transformation

$$y = R-r \tag{B 3}$$

Then

$$r = R-y$$

and

$$dr = -dy$$

The limits of integration become

$$r = R-\delta = R-y;\ y=\delta$$

and

$$r = R = R-y;\ y=0$$

Therefore

$$\int_{R-\delta}^{R} f(\rho, u)\ r dr = R^2 \int_{o}^{\delta/R} f(\rho, u)\left(1 - \frac{y}{R}\right)\ d\ \left(\frac{y}{R}\right) \tag{B 4}$$

Referring the continuity equation (B 1) to the duct mass flow $\dot{m}_o$

$$\dot{m}_o = \rho_{e_1} u_{e_1}\ \pi R^2 \tag{B 5}$$

and the momentum equation (B 2) to the term

$$\dot{I}_o = \rho_{e_1} u^2_{e_1}\ \pi R^2 \tag{B 6}$$

substituting (A 7) and (A 8) and rearranging, there results for constant T_{t_e}

$$2\int_{o}^{\delta_1/R}\frac{\rho u}{\rho_{e_1}u_{e_1}}\left(1-\frac{y}{R}\right)d\left(\frac{y}{R}\right)-\frac{2p_3M_{e_3}}{p_1M_{e_1}}\sqrt{\frac{1+\frac{\gamma-1}{2}M^2_{e_3}}{1+\frac{\gamma-1}{2}M^2_{e_1}}}\int_{o}^{\delta_3/R}\frac{\rho u}{\rho_{e_3}u_{e_3}}\times$$

$$\left(1-\frac{y}{R}\right)d\left(\frac{y}{R}\right)-\frac{\dot{m}_B}{m_o}=0 \qquad \text{(B 7)}$$

and

$$\left[2\frac{\delta_1}{R}-\left(\frac{\delta_1}{R}\right)^2\right]-\left[2\frac{\delta_3}{R}-\left(\frac{\delta_3}{R}\right)^2\right]\frac{p_3}{p_1}-2\int_{1-\delta_1/R}^{1-\delta_3/R}\frac{p_{e_2}}{p_1}\frac{r}{R}\,d\left(\frac{r}{R}\right)$$

$$-2\gamma M^2_{e_3}\frac{p_3}{p_1}\int_{o}^{\delta_3/R}\frac{\rho u^2}{\rho_{e_3}u^2_{e_3}}\left(1-\frac{y}{R}\right)d\left(\frac{y}{R}\right)+2\gamma M^2_{e_1}\int_{o}^{\delta_1/R}\frac{\rho u^2}{\rho_{e_1}u^2_{e_1}}\left(1-\frac{y}{R}\right)d\left(\frac{y}{R}\right)$$

$$-\gamma M^2_{e_1}\frac{\dot{I}_{B_x}}{I_o}=0 \qquad \text{(B 8)}$$

which are the desired equations as given in the text.

For the axially symmetric case, the mass transfer term $\dot{m}_B$ is referred to the duct mass flow $\dot{m}_o$. Since the suction flow rate is specified as a fraction of the upstream boundary-layer mass flow, a conversion is necessary to give the mass-flow ratio in equation (B 7). From the definitions of $\dot{m}_B$, $\dot{m}_o$, and $\dot{m}_{BL}$

$$\dot{m}_{BL}=\int_{R-\delta_1}^{R}2\pi\rho urdr$$

and

$$\dot{m}_o = \rho_{e_1} u^2_{e_1} \pi R^2$$

Therefore

$$\frac{\dot{m}_{BL}}{\dot{m}_o} = 2 \int_o^{\delta_1/R} \frac{\rho u}{\rho_{e_1} u_{e_1}} \left(1 - \frac{y}{R}\right) d\left(\frac{y}{R}\right)$$

The desired mass-flow term is then

$$\frac{\dot{m}_B}{\dot{m}_o} = 2 \left(\frac{\dot{m}_B}{\dot{m}_{BL}}\right) \int_o^{\delta_1/R} \frac{\rho u}{\rho_{e_1} u_{e_1}} \left(1 - \frac{y}{R}\right) d\left(\frac{y}{R}\right) \qquad \text{(B 9)}$$

The term $\dot{I}_{B_x}/\dot{I}_o$ in equation (B 8) is now evaluated for several mass-transfer configurations.

Porous-wall suction. -- For mass removal by suction through a porous wall, the transfer of x-momentum across the control surface is zero and

$$\left(\frac{\dot{I}_{B_x}}{\dot{I}_o}\right)_{\text{Porous-wall}} = 0 \qquad \text{(B 10)}$$

Perforated-wall or slot suction. -- For the case of mass removal by suction through a series of perforations or a slot, the x-momentum transferred across the control surface (positive outward by convention) is set equal to the x-momentum associated with the suction flow at station 1:

$$\dot{I}_{B_x} = \int_{r_u}^{R} 2\pi\rho u^2 \, r dr$$

where r_u is the radius defined by

$$\dot{m}_B = \int_{r_u}^{R} 2\pi\rho u r dr$$

Then, with (B 5)

$$\frac{\dot{m}_B}{\dot{m}_o} = \frac{\int_{r_u}^{R} 2\pi\rho\, u r dr}{\rho_{e_1} u_{e_1} \pi R^2} = 2 \int_{r_u/R}^{1} \frac{\rho u}{\rho_{e_1} u_{e_1}} \frac{r}{R}\, d\left(\frac{r}{R}\right)$$

Applying the transformation (B 4) there results

$$\frac{\dot{m}_B}{\dot{m}_o} = 2 \int_{o}^{y_u/R} \frac{\rho u}{\rho_{e_1} u_{e_1}} \left(1 - \frac{y}{R}\right) d\left(\frac{y}{R}\right) \qquad \text{(B 11)}$$

from which the distance ratio y_u/R is obtained.

The non-dimensional momentum-flux term required in (B 8) is given by

$$\frac{\dot{I}_{B_x}}{\dot{I}_o} = \frac{\int_{r_u}^{R} 2\pi\rho u^2 r dr}{\rho_{e_1} u_{e_1}^2 \pi R^2} = 2 \int_{r_u/R}^{1} \frac{\rho u^2}{\rho_{e_1} u_{e_1}^2} \frac{r}{R}\, d\left(\frac{r}{R}\right)$$

Applying (B 4), the desired momentum-flux term becomes

$$\left(\frac{\dot{I}_{B_x}}{\dot{I}_o}\right)_{\substack{\text{Perforated-}\\ \text{wall or slot}}} = 2 \int_{o}^{y_u/R} \frac{\rho u^2}{\rho_{e_1} u_{e_1}^2} \left(1 - \frac{y}{R}\right) d\left(\frac{y}{R}\right) \qquad \text{(B 12)}$$

where y_u/R is determined from the solution of (B 11).

Scoop suction. -- As for two-dimensional flow, the control volume for the axially symmetric scoop-suction model is different than for the previous cases (fig. 3b). The duct radius downstream of the interaction region is reduced by an amount equal to the scoop height. Accounting for this change in duct radius, the continuity equation may be stated in the form

$$2\pi \int_{R-\delta_1}^{R-y_s} \rho u r dr = 2\pi \int_{R''-\delta_3}^{R''} \rho u r dr \qquad \text{(B 13)}$$

The corresponding momentum equation is then

$$\pi(2R\delta_1-\delta_1^2)p_1 - \pi(2Ry_s-y_s^2)p_1 - \pi(2R''\delta_3-\delta_3^2)p_3$$
$$- \int_{R-\delta_1}^{R''-\delta_3} 2\pi p_{2_e} r dr = 2\pi \int_{R''-\delta_3}^{R''} \rho u^2 r dr - 2\pi \int_{R-\delta_1}^{R-y_s} \rho u^2 r dr \qquad \text{(B 14)}$$

Defining the suction flow by

$$\dot{m}_B = 2\pi \int_{R-y_s}^{R} \rho u r dr \qquad \text{(B 15)}$$

and substituting into (B 13)

$$2\pi \int_{R-\delta_1}^{R} \rho u r dr - \dot{m}_B = 2\pi \int_{R''-\delta_3}^{R''} \rho u r dr$$

Dividing by the duct mass flow $\dot{m}_o$, transforming by (B 4), and rearranging, the final form of the continuity equation for axially symmetric scoop suction becomes

$$2\int_o^{\delta_1/R} \frac{\rho u}{\rho_{e_1} u_{e_1}} \left(1-\frac{y}{R}\right) d\left(\frac{y}{R}\right) - 2\left(\frac{R''}{R}\right)^2 \frac{p_3 M_{e_3}}{p_1 M_{e_1}} \sqrt{\frac{1+\frac{\gamma-1}{2}M^2_{e_3}}{1+\frac{\gamma-1}{2}M^2_{e_1}}} \int_o^{\delta_3/R''} \frac{\rho u}{\rho_{e_3} u_{e_3}} \left(1-\frac{y''}{R''}\right) d\left(\frac{y''}{R''}\right)$$
$$- \frac{\dot{m}_B}{\dot{m}_o} = 0 \qquad \text{(B 16)}$$

Division of (B 14) by $\dot{I}_o$ (B 6) and subdivision of the second integral on the right, transformation by (B 4), and rearrangement gives the desired result

$$[2\frac{\delta_1}{R} - (\frac{\delta_1}{R})^2] - [2\frac{y_s}{R} - (\frac{y_s}{R})^2] - [2\frac{\delta_3}{R''} - (\frac{\delta_3}{R''})^2](\frac{R''}{R})^2 \frac{p_3}{p_1} - 2\int_{1-\delta_1/R}^{R''/R-\delta_3/R} \frac{p_{e_2}}{p_1}\frac{r}{R}\, d\,(\frac{r}{R})$$

$$- 2(\frac{R''}{R})^2 \gamma M^2_{e_3} \frac{p_3}{p_1}\int_o^{\delta_3/R''} \frac{\rho u^2}{\rho_{e_3} u^2_{e_3}}(1 - \frac{y''}{R''})d(\frac{y''}{R''}) + 2\gamma M^2_{e_1}\int_o^{\delta_1/R} \frac{\rho u^2}{\rho_{e_1} u^2_{e_1}}(1 - \frac{y}{R})d(\frac{y}{R})$$

$$- \gamma M^2_{e_1} \frac{\dot{I}_{B_x}}{I_o} = 0 \qquad \text{(B 17)}$$

The x-momentum flux term is given by

$$(\frac{\dot{I}_{B_x}}{I_o})_{\text{Scoop}} = 2\int_o^{y_s/R} \frac{\rho u^2}{\rho_{e_1} u^2_{e_1}}(1 - \frac{y}{R})\, d\,(\frac{y}{R}) \qquad \text{(B 18)}$$

where y_s/R is determined from the solution of

$$2\int_o^{y_s/R} \frac{\rho u}{\rho_{e_1} u_{e_1}}(1 - \frac{y}{R})\, d\,(\frac{y}{R}) = \frac{\dot{m}_B}{\dot{m}_o} \qquad \text{(B 19)}$$

Axially symmetric displacement and momentum thicknesses. -- Displacement and momentum thicknesses that are analogous to the two-dimensional values are define by the equations

$$\delta^* = R - [R^2 + \delta^2 - 2R\delta + 2\int_{R-\delta}^{R} \frac{\rho u}{\rho_e u_e} r dr]^{\frac{1}{2}} \qquad \text{(B 20)}$$

and

$$\theta = R - [R^2 - 2\int_{R-\delta}^{R} \frac{\rho u}{\rho_e u_e} r dr + 2\int_{R-\delta}^{R} \frac{\rho u^2}{\rho_e u^2_e} r dr]^{\frac{1}{2}} \qquad \text{(B 21)}$$

The final forms used in the solution are obtained by applying the transformation (B 4) to (B 20)

$$\frac{\delta^*}{R} = 1 - \left[1 + \left(\frac{\delta}{R}\right)^2 - 2\,\frac{\delta}{R} + 2\int_0^{\delta/R} \frac{\rho u}{\rho_e u_e}\left(1 - \frac{y}{R}\right)\, d\,\left(\frac{y}{R}\right)\right]^{\frac{1}{2}} \qquad \text{(B 22)}$$

and to (B 21)

$$\frac{\theta}{R} = 1 - \left[1 - 2\int_0^{\delta/R} \frac{\rho u}{\rho_e u_e}\left(1 - \frac{y}{R}\right)d\left(\frac{y}{R}\right) + 2\int_0^{\delta/R} \frac{\rho u^2}{\rho_e u^2_e}\left(1 - \frac{y}{R}\right)d\left(\frac{y}{R}\right)\right]^{\frac{1}{2}} \qquad \text{(B 23)}$$

REFERENCES

1. Bogdonoff, S.M., Kepler, C.E. and Sanlorenzo, E. A Study of Shock Wave Turbulent Boundary Layer Interaction at M = 3.0. Princeton University, Department of Aeronautical Engineering Report 222, July 1953.

2. Kuehn, D.M. Experimental Investigation of the Pressure Rise Required for the Incipient Separation of Turbulent Boundary Layers in Two-Dimensional Supersonic Flow, NASA Memorandum 1-21-59A, February 1959.

3. Pinckney, S.Z. Data on Effects of Incident-Reflecting Shocks on the Turbulent Boundary Layer. NASA TM X-1221, March 1966.

4. Reshotko, E. and Tucker, M. Effects of a Discontinuity on Turbulent Boundary-Layer-Thickness Parameters with Application to Shock-Induced Separation. NACA TN 3454, May 1955.

5. Benson, J.L. and Maslowe, S.A. Bluntness and Boundary Layer Displacement Effects on Hypersonic Inlet Flow Fields. AIAA Paper No. 65-617, June 1965.

6. Kutschenreuter, P.H., Jr., Brown, D.L., Hoelmer, W., et al. Investigation of Hypersonic Inlet Shock-Wave Boundary Layer Interaction, Part II: Continuous Flow Test and Analysis. AFFDL-TR-65-36, April 1966.

7. Cnossen, J.W. and O'Brien, R.L. Investigation of the Diffusion Characteristics of Supersonic Streams Composed Mainly of Boundary Layers. AIAA J. Aircraft, vol. 2, no. 6, November-December, 1965, p. 485.

8. Strike, W.T. and Rippey, J. Influence of Suction on the Interaction of an Oblique Shock with a Turbulent Boundary Layer at Mach Number 3. AEDC TN-61-129, October 1961.

9. Kutschenreuter, P.H., Zurschemeide, R.L., and Surber, L.E. An Investigation of Shock Wave-Boundary Layer Interaction with Suction. ASRMFD TM 61-30, January 1962.

10. Wainwright, J.B. Description of an Experimental Investigation of the Effects of Boundary Layer Bleed on Shock-Wave-Boundary Layer Interaction. University of Southern California Report 65-35, December 1962.

11. Pinckney, S.Z. Semiempirical Method for Predicting Effects of Incident-Reflecting Shocks on the Turbulent Boundary Layer. NASA TN D-3029, October 1965. See also: Pinckney, S.Z. Boundary Layer Changes Across an Incident-Reflecting Shock. AIAA Preprint 63116, April 1963.

12. Sorenson, V.L. Computer Program for Calculating Flow Fields in Supersonic Inlets. NASA TND-2897, July 1965.

13. Fluid Meters, Their Theory and Application. Fifth Ed., The American Society of Mechanical Engineers, New York, 1959.

14. Chapman, D.R., Kuehn, D.M., and Larson, H.K. Investigation of Separated Flows in Supersonic and Subsonic Streams with Emphasis on the Effect of Transition. NACA Report 1356, 1956.

15. Bogdonoff, S.M. Some Experimental Studies of the Separation of Supersonic Turbulent Boundary Layers. Princeton University Department of Aeronautical Engineering Report 336, June 1955.

16. Cubbison, R.W., Meleason, E.T., and Johnson, D.F. Effect of Porous Bleed in a High-Performance Axisymmetric, Mixed-Compression Inlet at Mach 2.50. NASA TM X-1692, November 1968.

TABLE I

TEST CONDITIONS AND DATA OBTAINED

Test	Model No.	M_{e_1}	P_{t_o} Lb/in^2	T_{t_o} ^oR	Re/ft	Run No.	Bleed Conf.	δ_c	C.B. Tip Pos.	Wall p	Pitot p	Pitot Loc.
1	25	2.82	34.3	543	5.58 x10^6	210-217	Solid	-	-	✓	7 Loc.	2.50-4.20
2	74	2.82	34.3	543	5.58 x10^6	392	Solid	-	-	-	29 Loc.	Center-Line
3	22	3.78	59.1	546	5.61 x10^6	179-189	Solid	-	-	✓	7 Loc.	2.50-4.21
4	73	3.78	59.1	546	5.61 x10^6	391	Solid	-	-	-	29 Loc.	Center-Line
5	46	2.82	34.3	539	5.63 x10^6	233-248	Solid	10^o	0.88	✓	15 Loc.	2.50-4.20
6	52	2.82	34.4	544	5.56 x10^6	249-264	Solid	12^o	1.02	✓	15 Loc.	2.50-4.20
7	81	2.82	34.4	547	5.46 x10^6	1000-1013	Solid	13^o	1.08	✓	13 Loc.	2.50-3.79
8	55	2.82	34.3	542	5.59 x10^6	265-279	Solid	14^o	1.16	✓	14 Loc.	2.50-4.00
9	49	2.82	34.2	540	5.59 x10^6	218-232	Solid	15^o	1.23	✓	14 Loc.	2.50-4.00

TABLE I, Continued

Test	Model No.	M_{e_1}	P_{t_o} Lb/in^2	T_{t_o} ^oR	Re/ft	Run No.	Bleed Conf.	δ_c	C.B. Tip Pos.	Wall p	Pitot p	Pitot Loc.
10	58	2.82	34.3	542	5.60 x10^6	281-294	Solid	16^o	1.30	✓	13 Loc.	2.50-3.79
11	43	3.78	59.0	547	5.42 x10^6	187 204	Solid	8^o	-.01	✓	15 Loc.	2.50-4.21
12	32	3.78	59.1	545	5.37 x10^6	149-164	Solid	10^o	0.26	✓	15 Loc.	2.50-4.21
13	40	3.78	59.0	543	5.44 x10^6	135-148	Solid	13^o	0.61	✓	13 Loc.	2.50-3.79
14	37	3.78	59.0	545	5.41 x10^6	165-178	Solid	14^o	0.75	✓	13 Loc.	2.52-3.79
15	34	3.78	59.1	542	5.20 x10^6	123-134	Solid	15^o	0.85	✓	11 Loc.	2.50-3.49
16	82	2.82	34.6	543	5.74 x10^6	1052-1064	Perfo-rated	15^o	0.98	✓	12 Loc.	2.50-3.59
17	83	2.82	34.5	535	5.69 x10^6	1033-1046	Perfo-rated	16^o	1.05	✓	13 Loc.	2.50-3.79
18	84	2.82	34.2	539	5.69 x10^6	1100-1112	Perfo-rated	16^o	0.95	✓	11 Loc.	2.50-3.50
19	85	2.82	34.4	542	5.69 x10^6	1121-1130	Perfo-rated	18^o	1.03	✓	9 Loc.	2.50-3.30

TABLE I, Concluded

Test	Model No.	M_{e_1}	P_{t_o} Lb/in^2	T_{t_o} ^oR	Re/ft	Run No.	Bleed Conf.	δ_c	C.B. Tip Pos.	Wall p	Pitot p	Pitot Loc.
20	86	2.82	34.5	538	5.65 x10^6	1137-1147	Perforated	18^o	1.03	✓	9 Loc.	2.50-3.30
21	68	3.78	59.0	555	5.50 x10^6	374-390	Perforated	10^o	-.09	✓	16 Loc.	2.40-4.21
22	78	3.78	59.0	549	5.48 x10^6	421-437	Perforated	10^o	-.09	✓	16 Loc.	2.40-4.21
23	60	3.78	59.0	544	5.45 x10^6	295-308	Perforated	15^o	0.50	✓	13 Loc.	2.41-3.59
24	69	3.78	59.0	552	5.47 x10^6	360-372	Perforated	15^o	0.50	✓	12 Loc.	2.41-3.49
25	77	3.78	59.0	560	5.35 x10^6	405-419	Perforated	15^o	0.50	✓	14 Loc.	2.40-3.79
26	-	3.78	59.0	560	5.35 x10^6	340	Solid	10^o	-.09	✓	-	-
						334	Solid	15^o	0.50			
						319	Perforated					

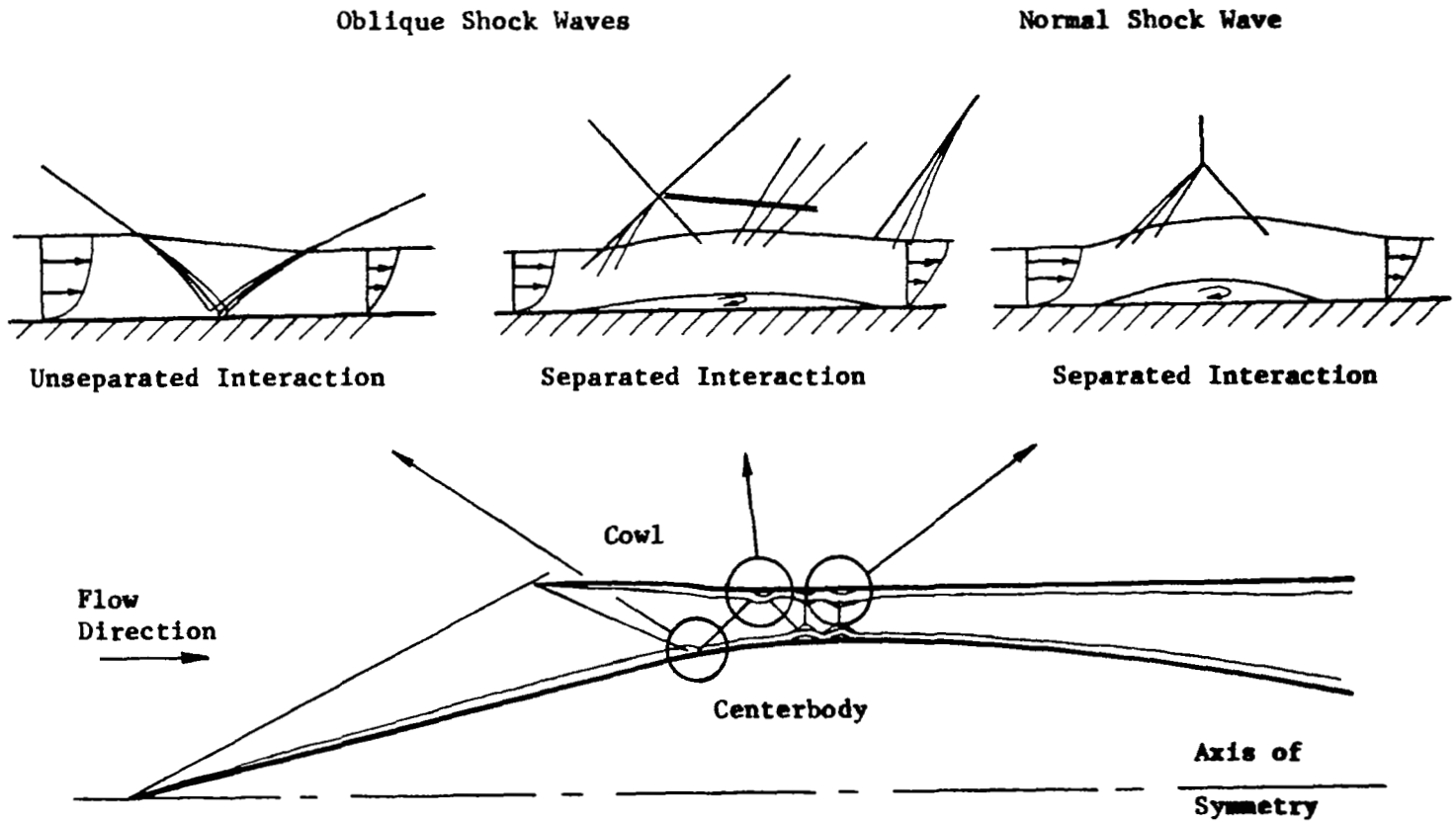

Figure 1. Schematic Representation of Internal-External Compression Supersonic Inlet.

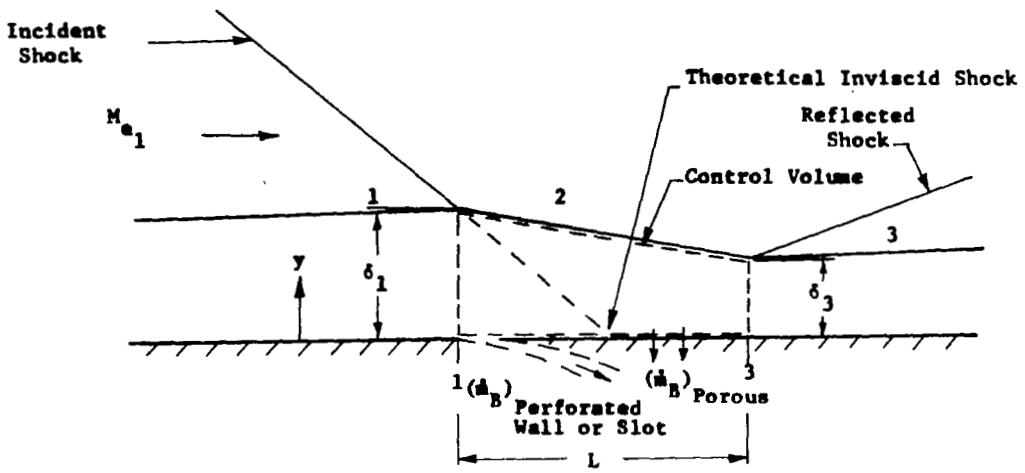

(a) Zero Bleed, Porous-Wall Suction, and Perforated-Wall or Slot Suction.

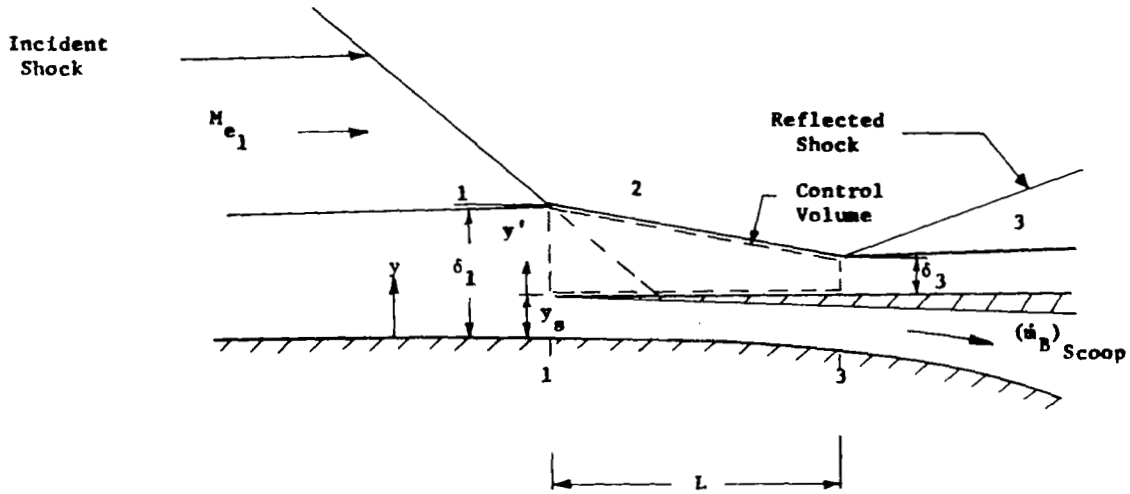

(b) Scoop Suction.

Figure 2. Two-Dimensional Flow Models.

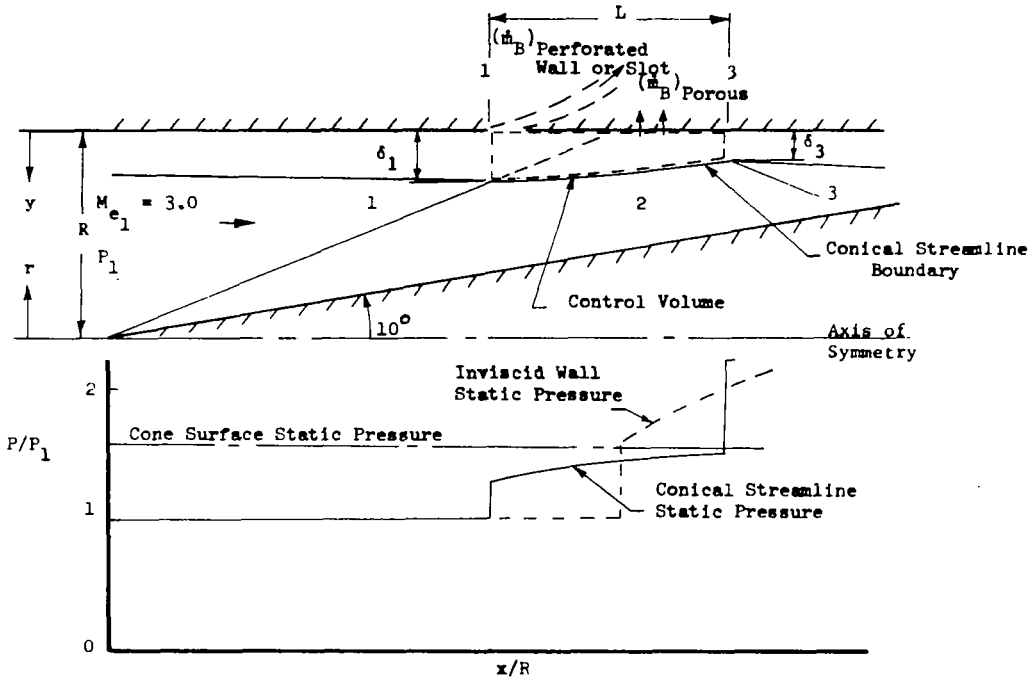

(a) Zero Bleed, Porous-Wall Suction, and Perforated-Wall or Slot Suction.

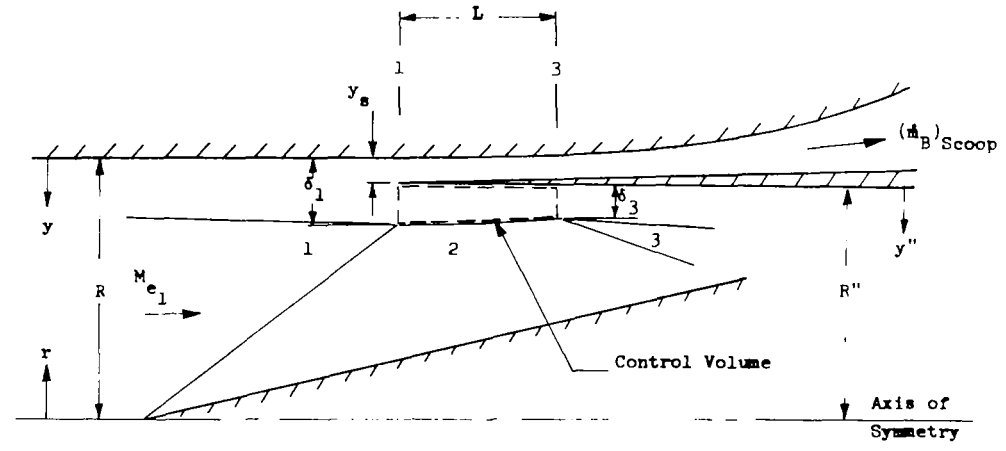

(b) Scoop Suction.

Figure 3. Axially Symmetric Flow Models.

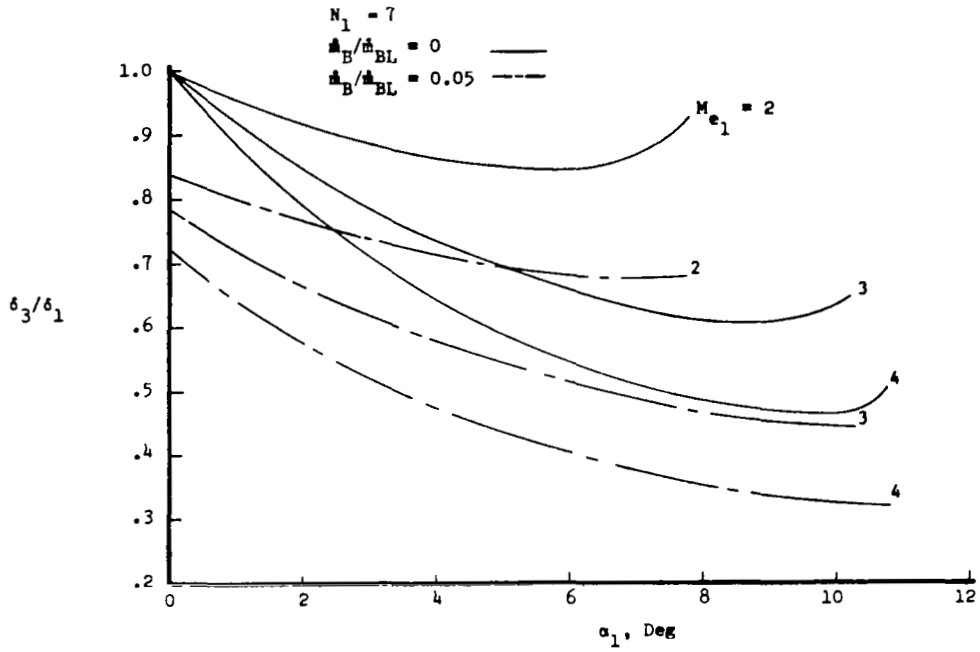

(a) Boundary-Layer Thickness Ratio.

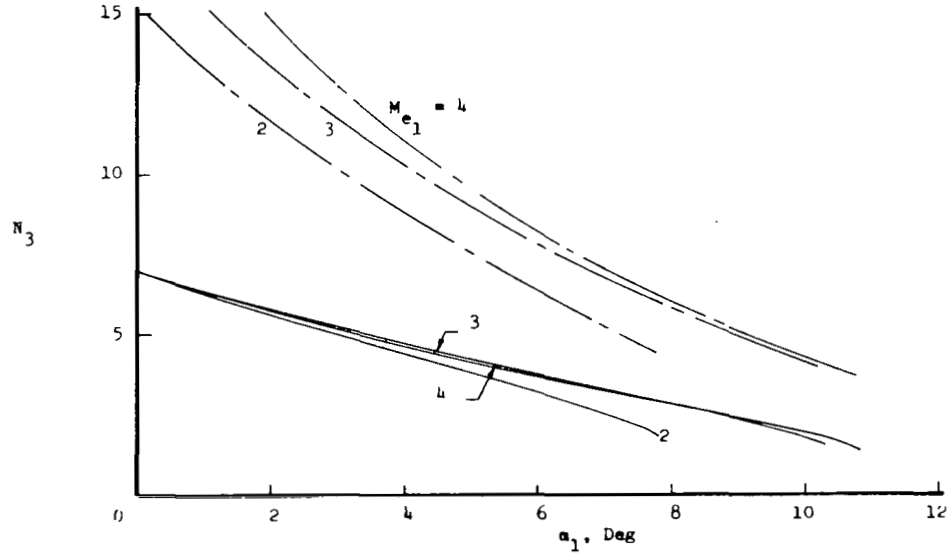

(b) Downstream Power-Law Parameter.

Figure 4. Boundary-Layer Properties for Solid Wall and Porous-Wall Suction, Two-Dimensional Flow.

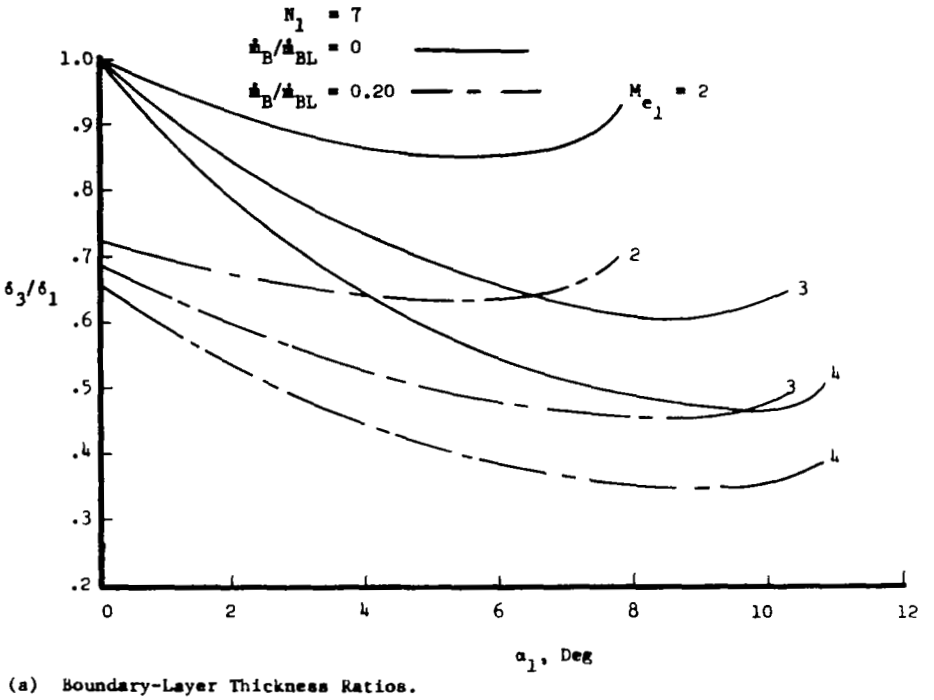

(a) Boundary-Layer Thickness Ratios.

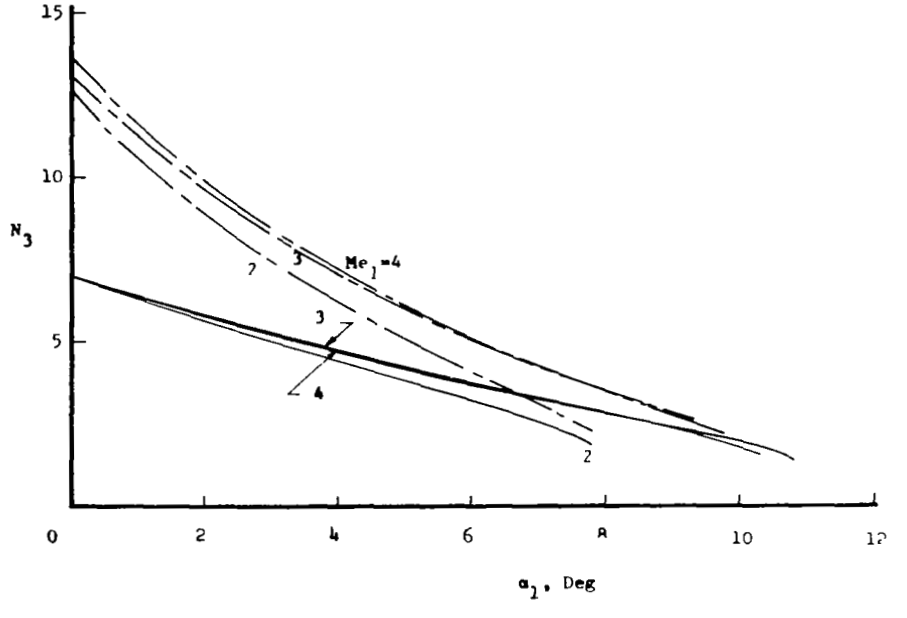

(b) Downstream Power-Law Parameters.

Figure 5. Boundary-Layer Properties for Solid-Wall and Perforated-Wall or Slot Suction, Two-Dimensional Flow.

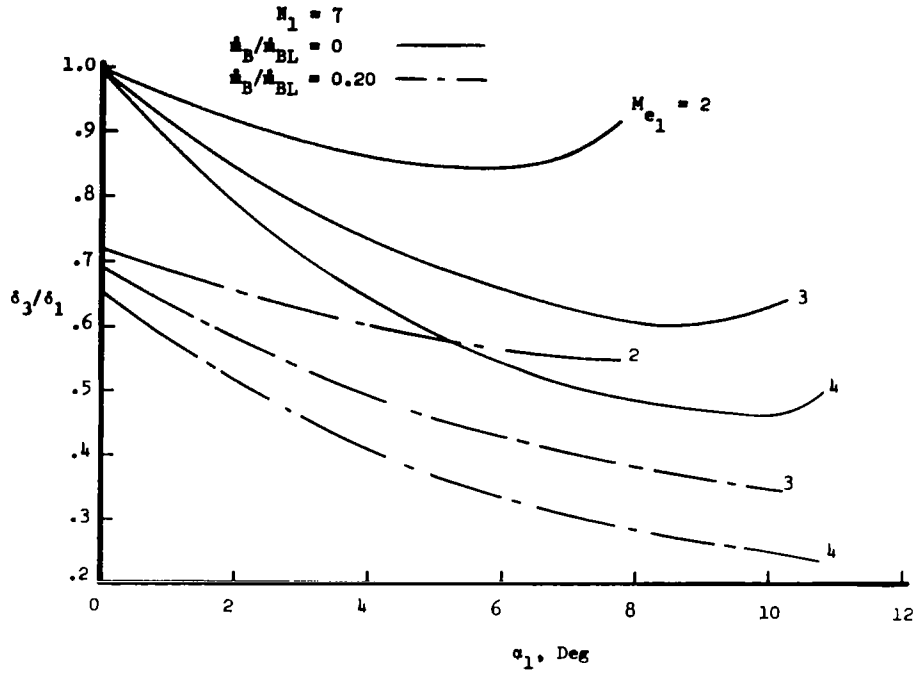

(a) Boundary-Layer Thickness Ratios.

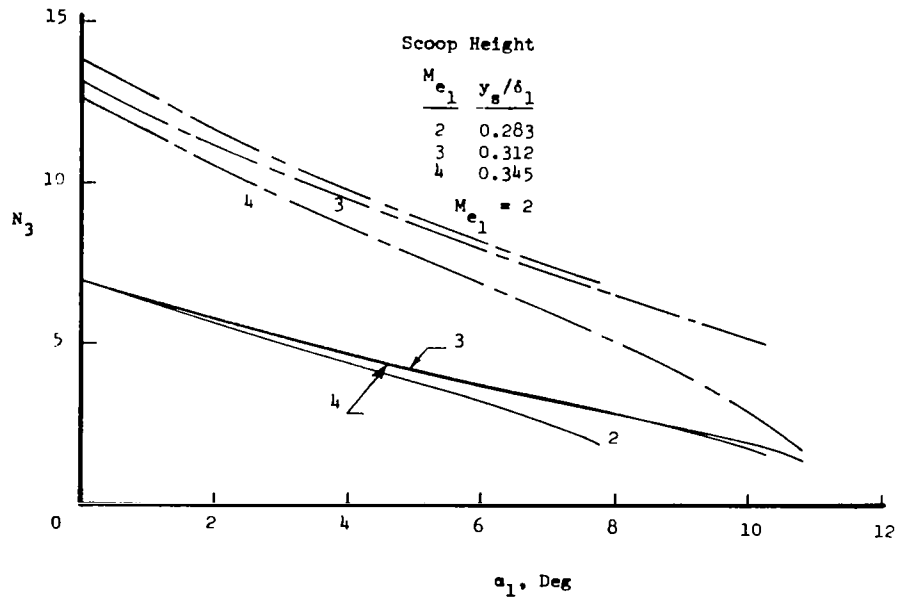

(b) Boundary-Layer Properties for Solid Wall and Scoop Suction, Two-Dimensional Flow.

Figure 6. Boundary-Layer Properties for Solid Wall and Scoop Suction, Two-Dimensional Flow.

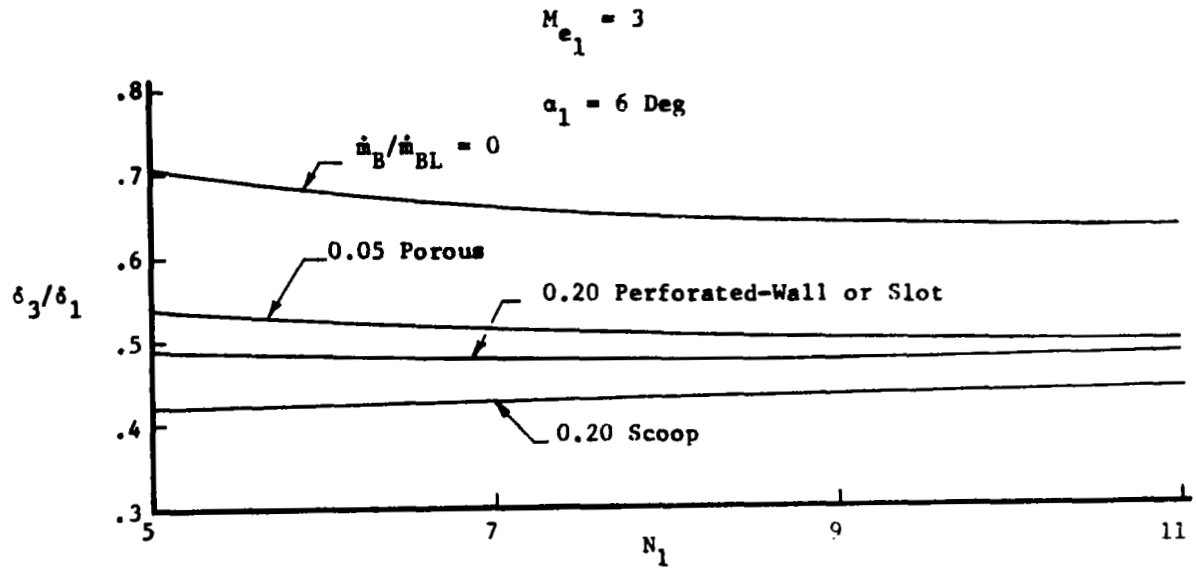

(a) Boundary-Layer Thickness Ratios.

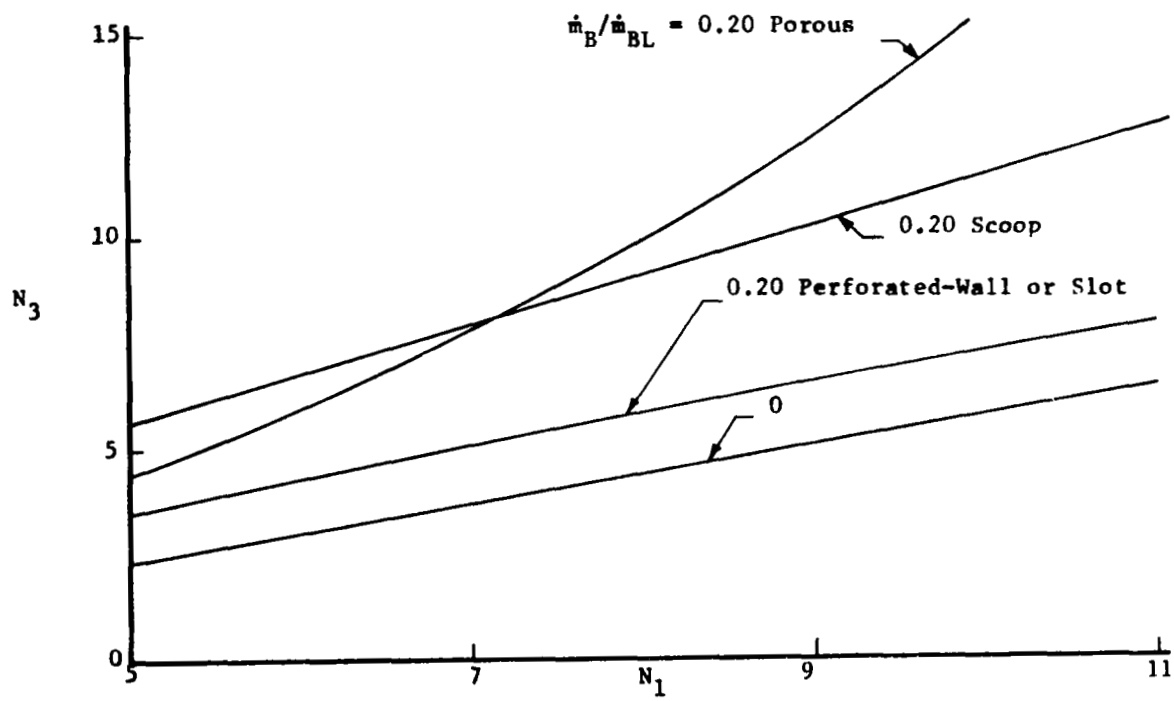

(b) Downstream Power-Law Parameters.

Figure 7. Effect of Upstream Power-Law Parameter on Boundary-Layer Properties, Two-Dimensional Flow.

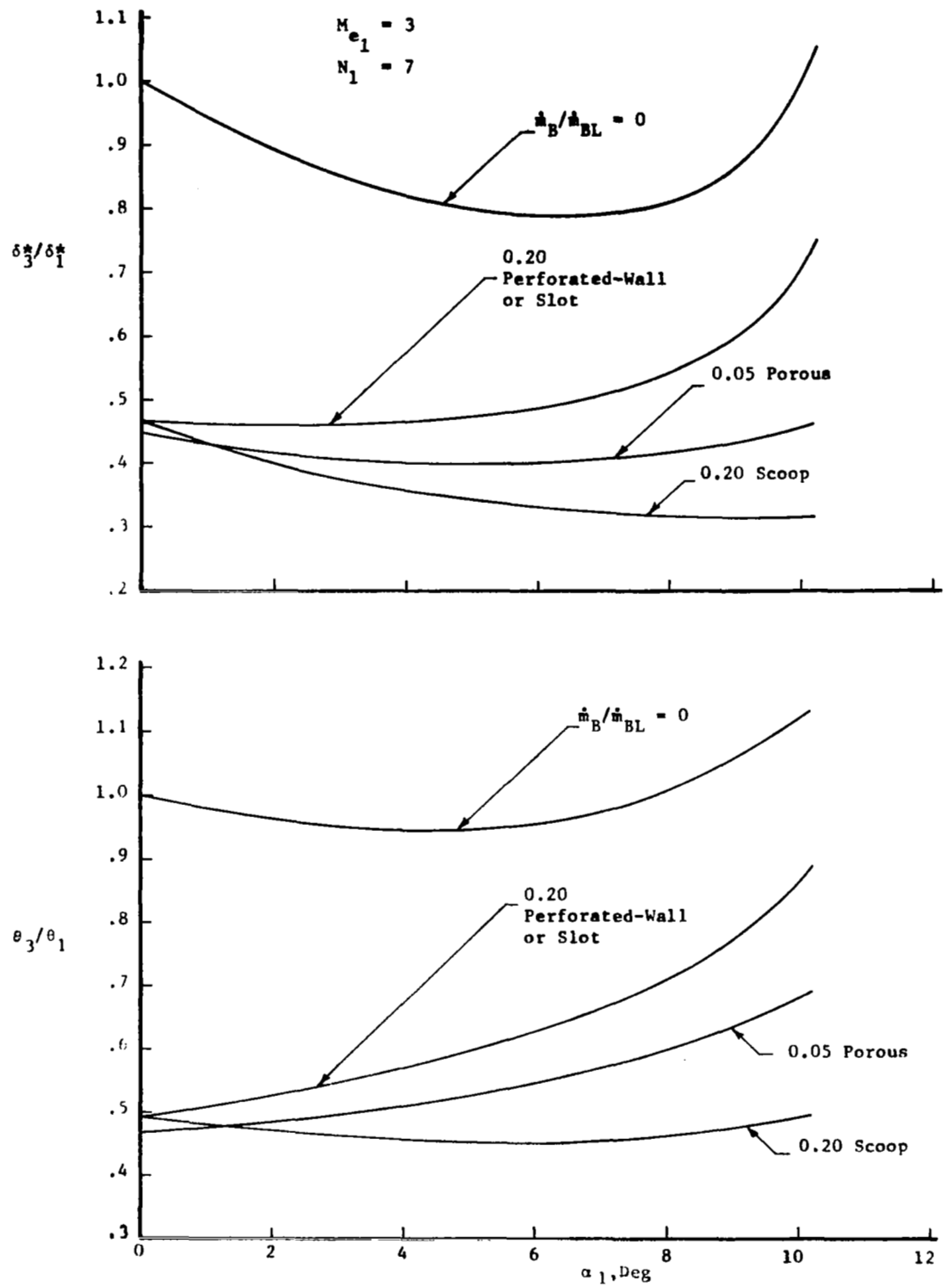

Figure 8. Displacement and Momentum Thickness Ratios for All Suction Configurations, Two-Dimensional Flow.

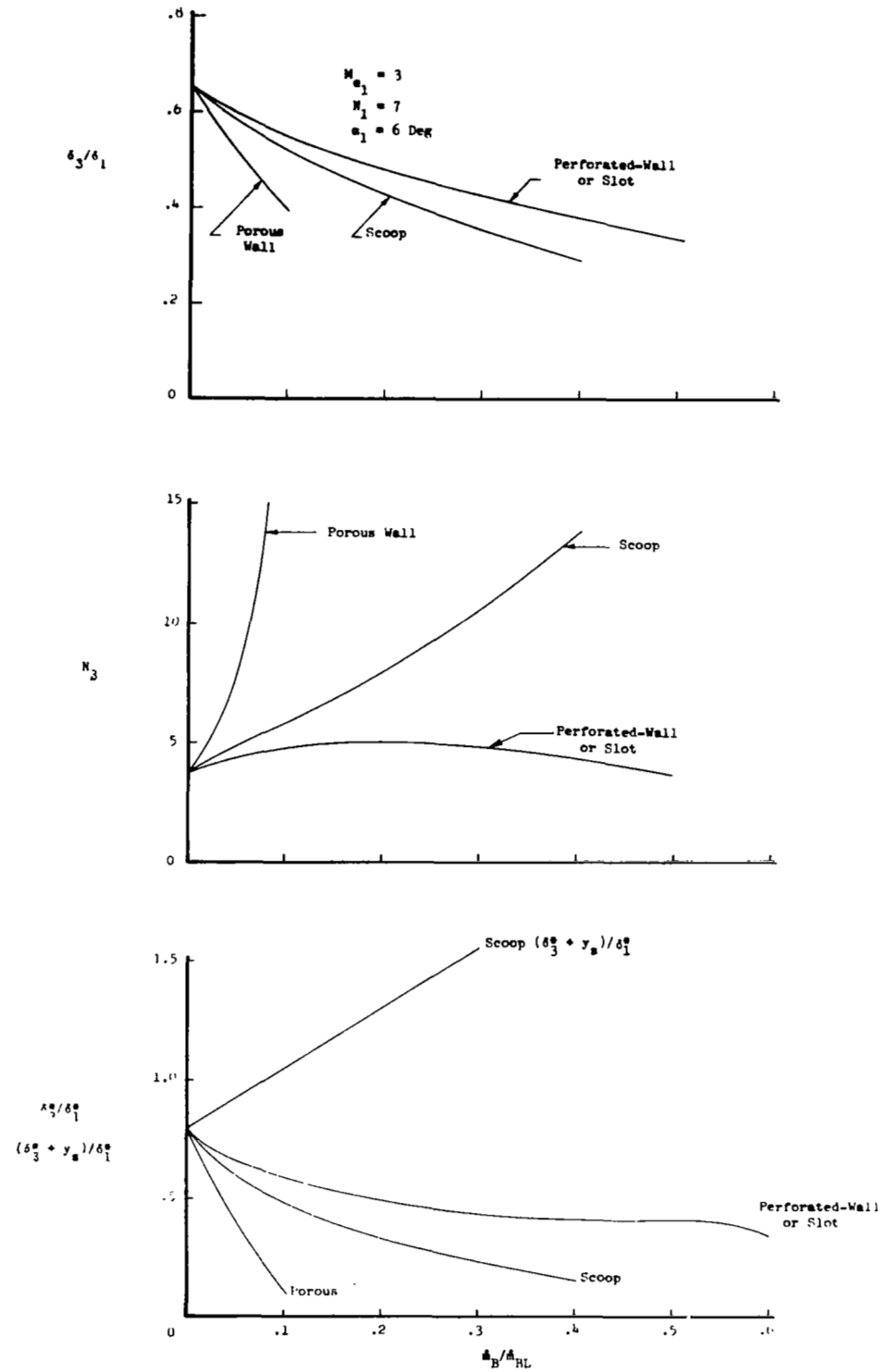

Figure 9. Effect of Suction Rate on Boundary-Layer Properties for All Suction Configurations, Two-Dimensional Flow.

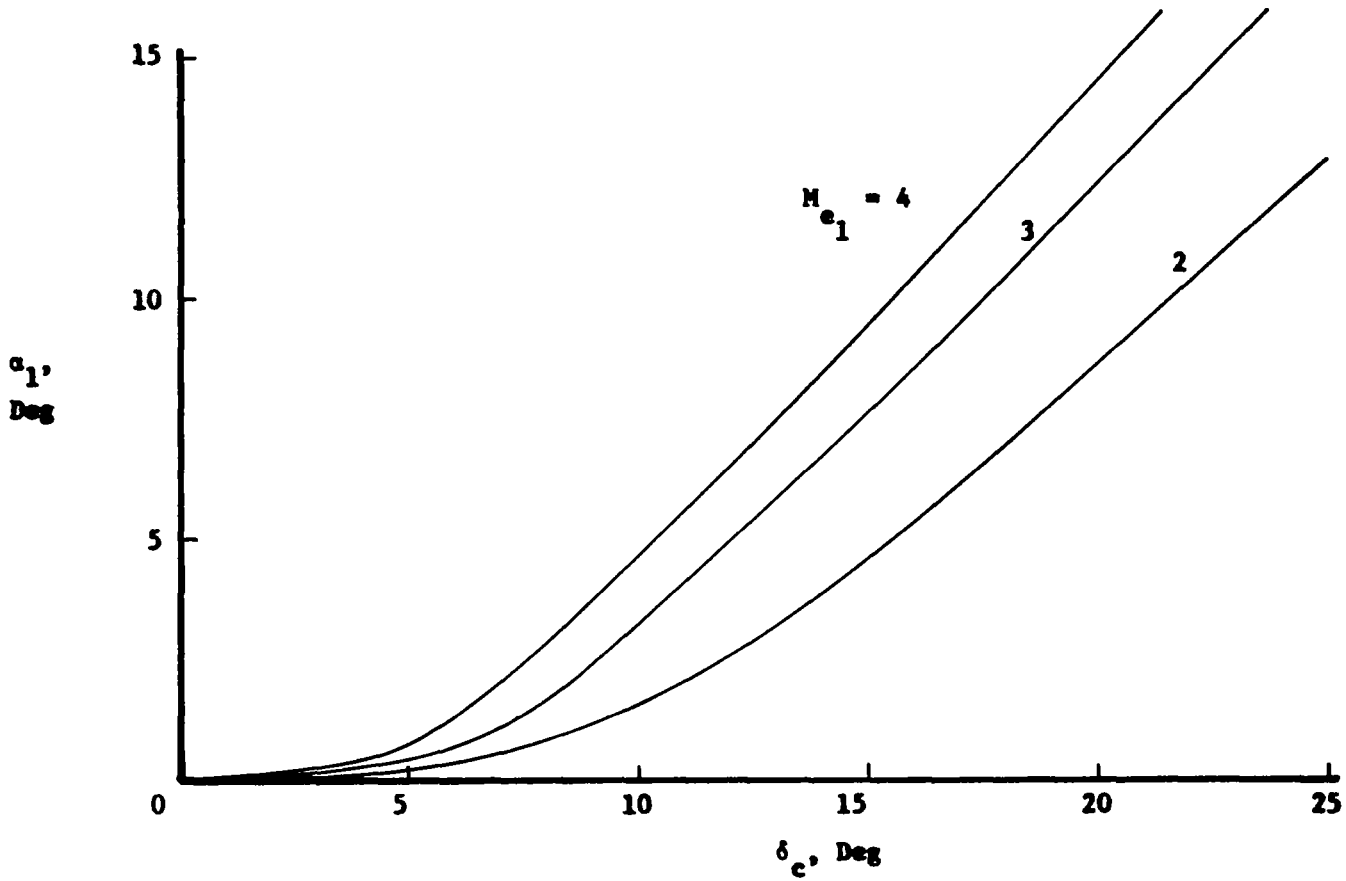

Figure 10. Incident Shock-Wave Flow-Deflection Angles for Conical Shock Waves.

$M_{e_1} = 3 \quad \delta_1/R = 0.1$

$N_1 = 7 \quad \alpha_1 = 3.16$ Deg

Method	δ_3/δ_1	N_3	p_3/p_1
(1) 2-D	0.783	5.09	1.60
(2) Axi.P_2 = c	0.775	5.04	1.60
(3) Axi. Conical	0.707	4.46	1.91

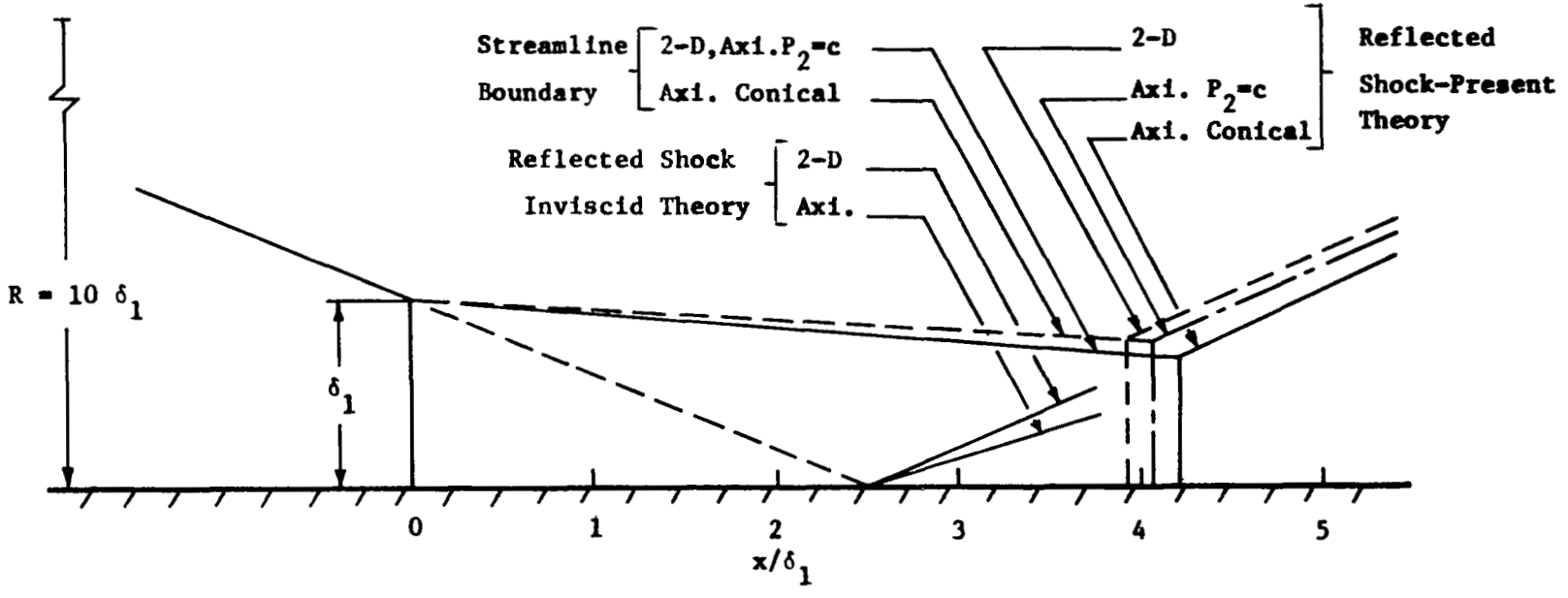

Figure 11. Comparison of Results for Two-Dimensional and Axially Symmetric Flows.

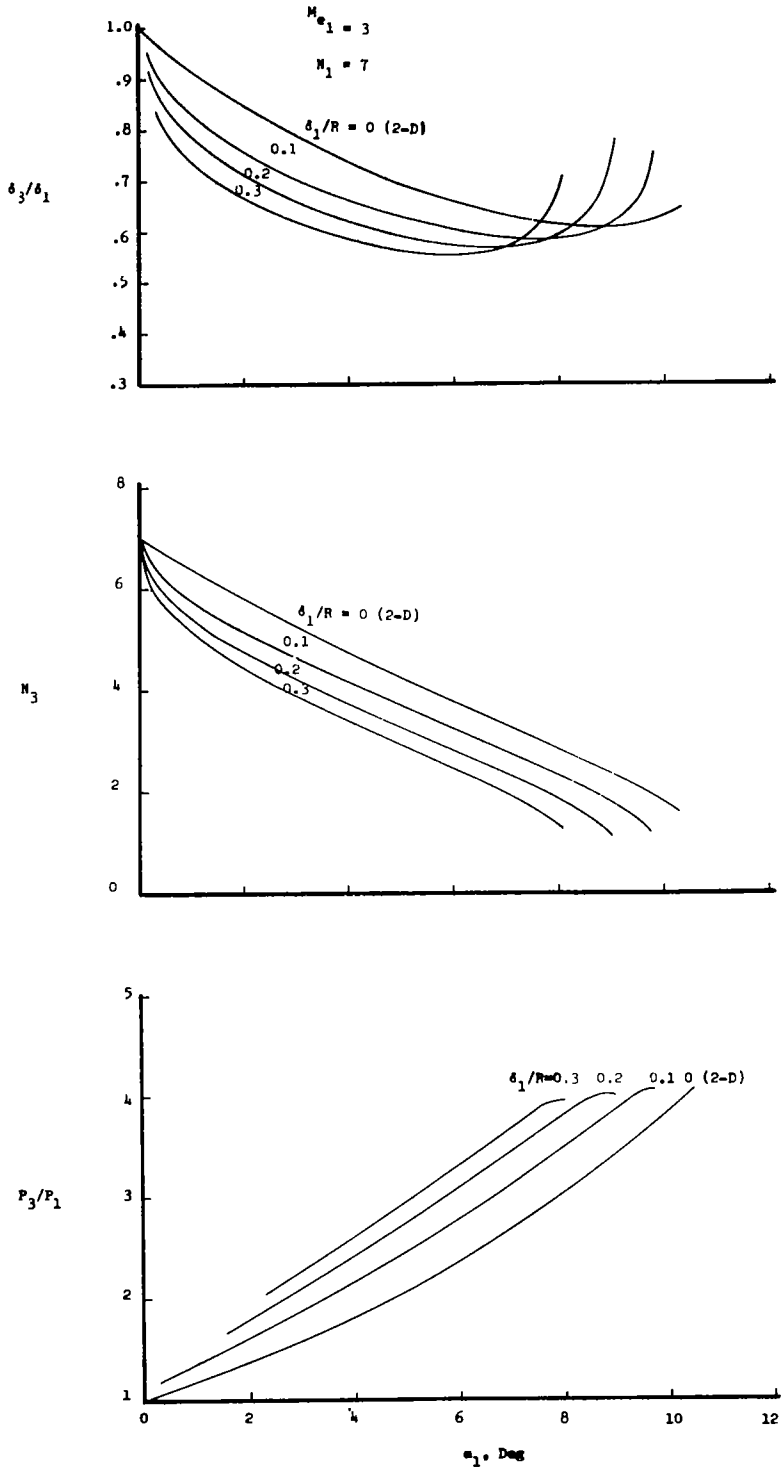

Figure 12. Boundary-Layer Properties for Solid Wall, Two-Dimensional and Axially Symmetric Flows.

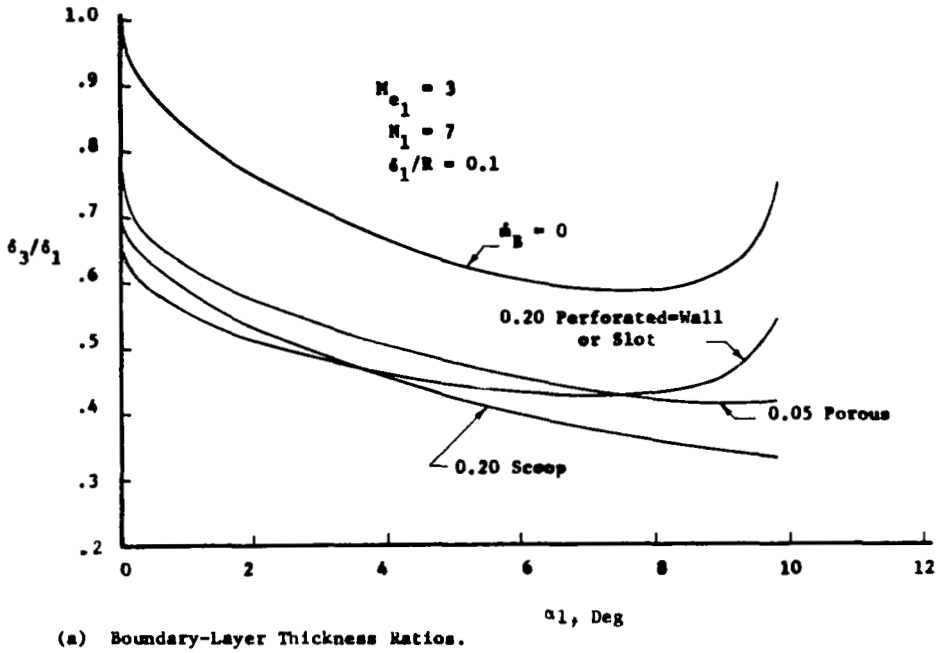

(a) Boundary-Layer Thickness Ratios.

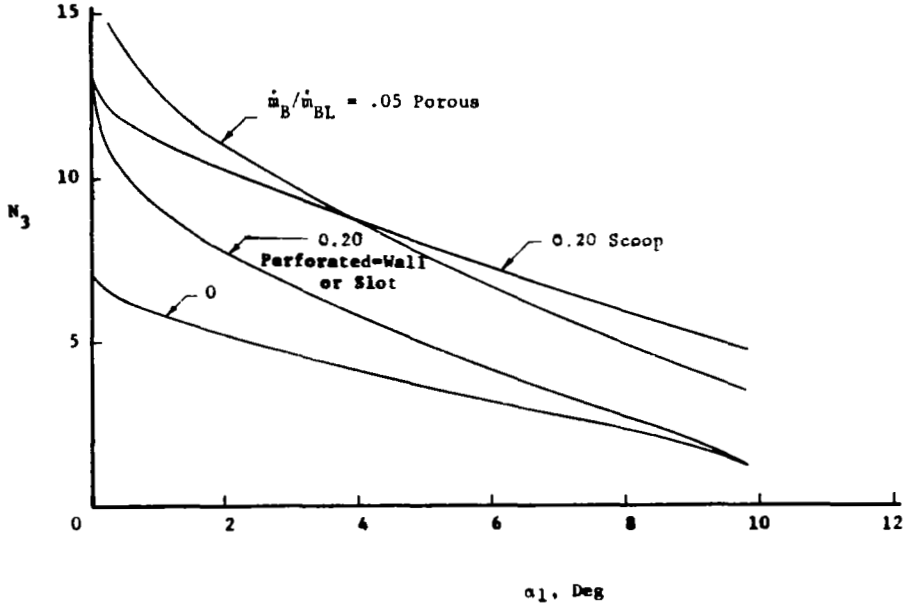

(b) Downstream Power-Law Parameters.

Figure 13. Boundary-Layer Properties for All Suction Configurations, Axially Symmetric Flow.

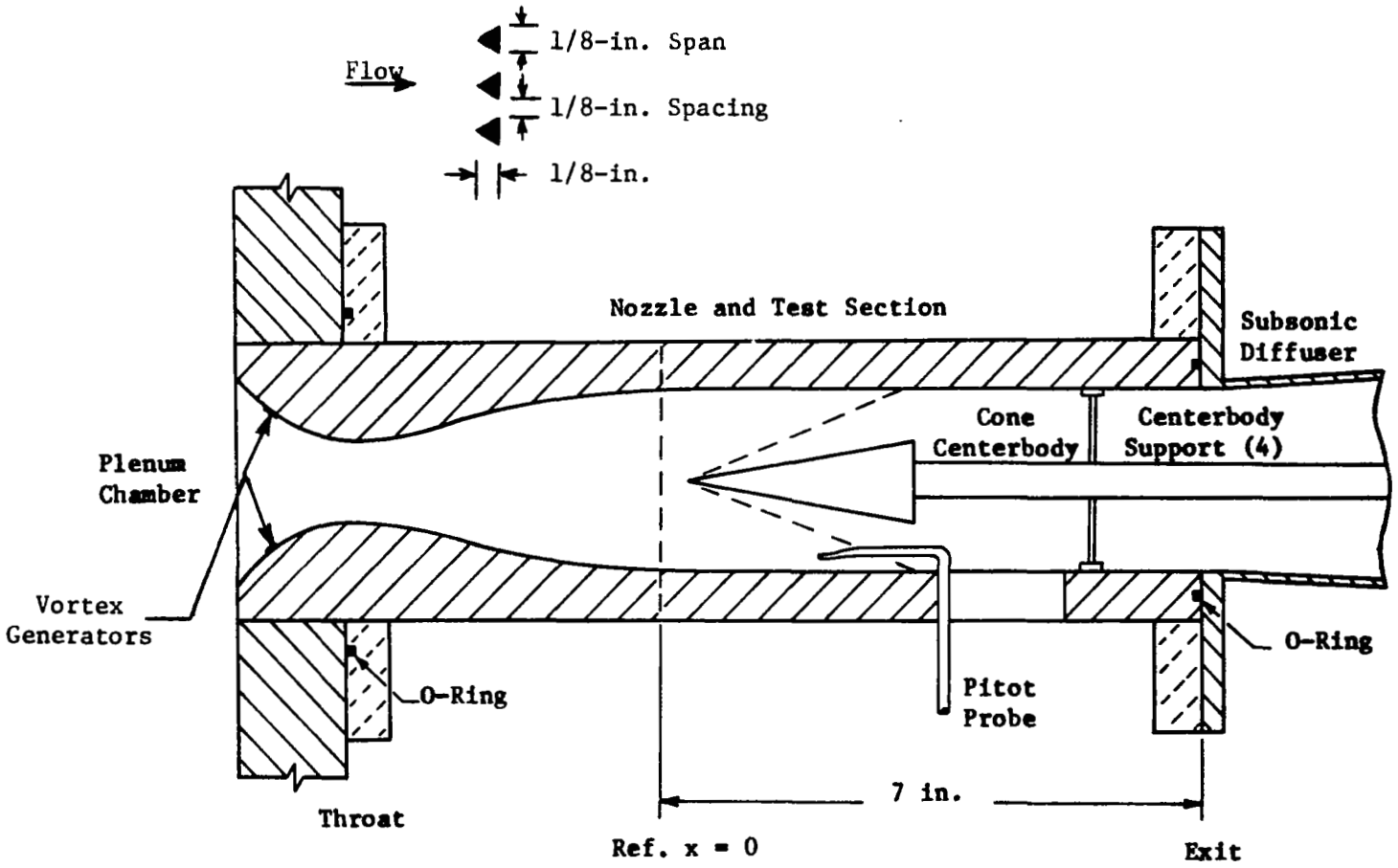

Figure 14. Wind Tunnel Nozzle.

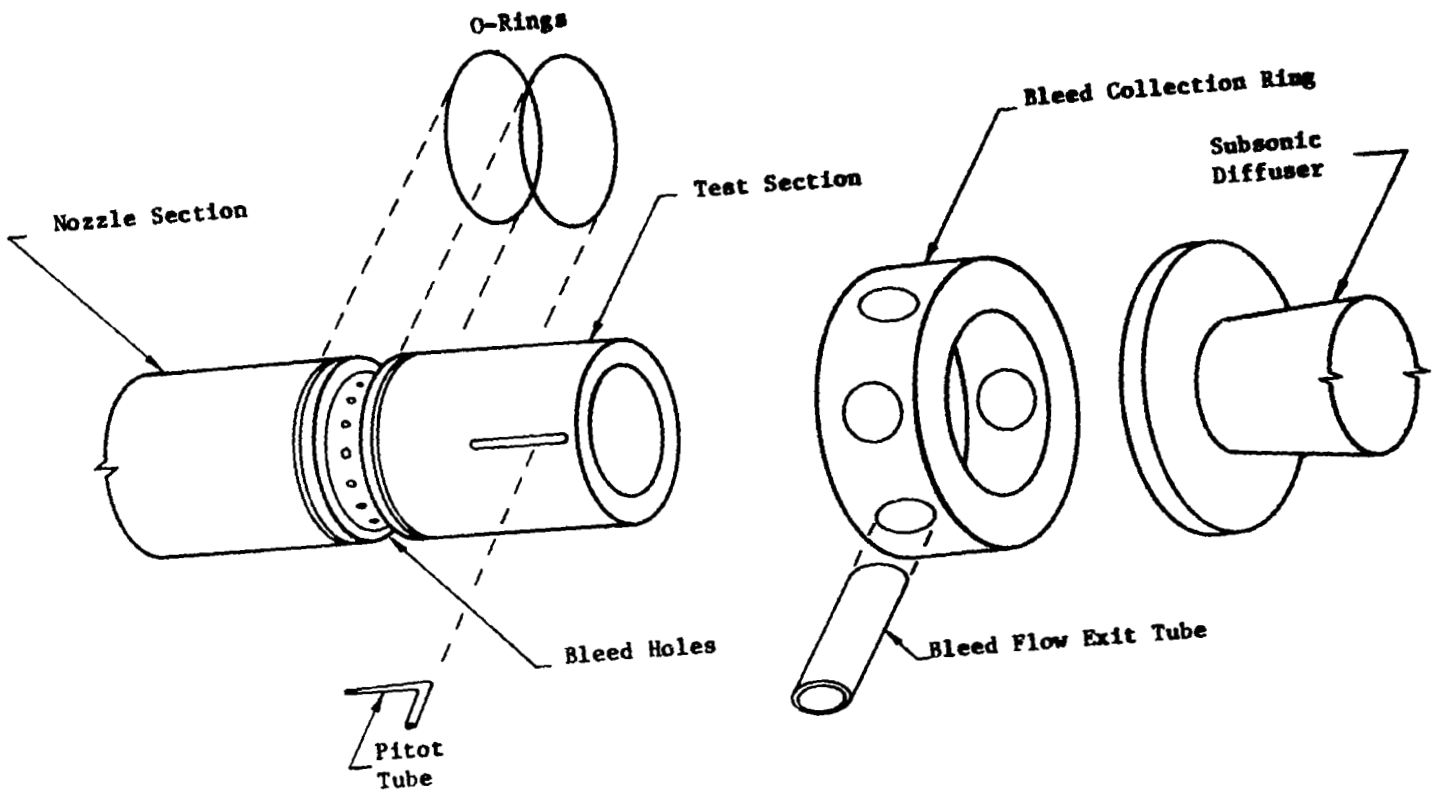

Figure 15. Wind Tunnel Test Section.

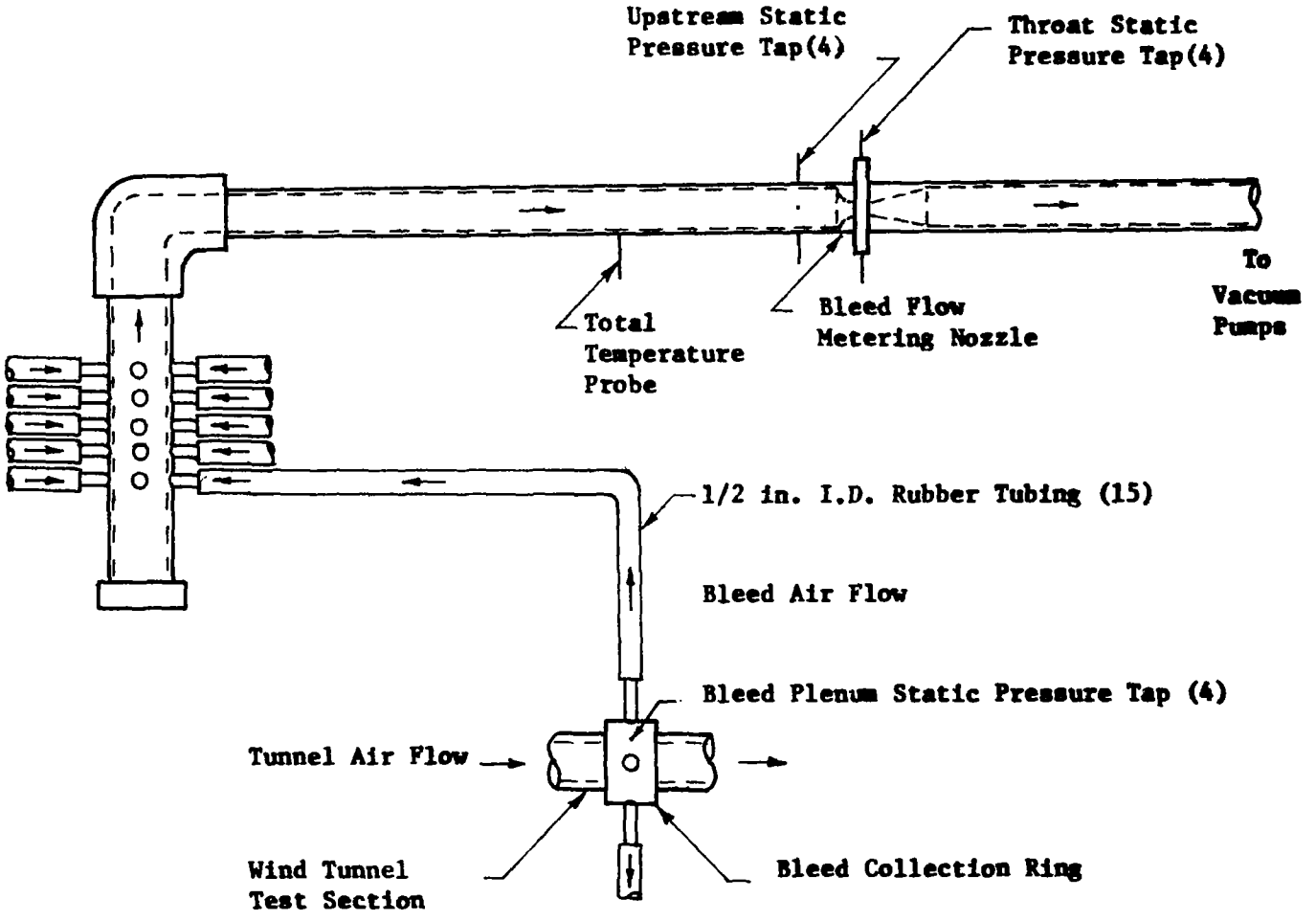

Figure 16. Suction System.

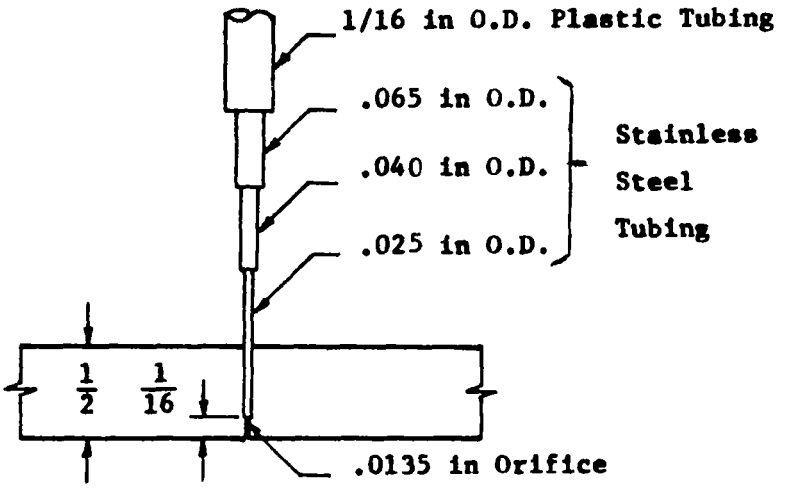

(a) Static Pressure Tap.

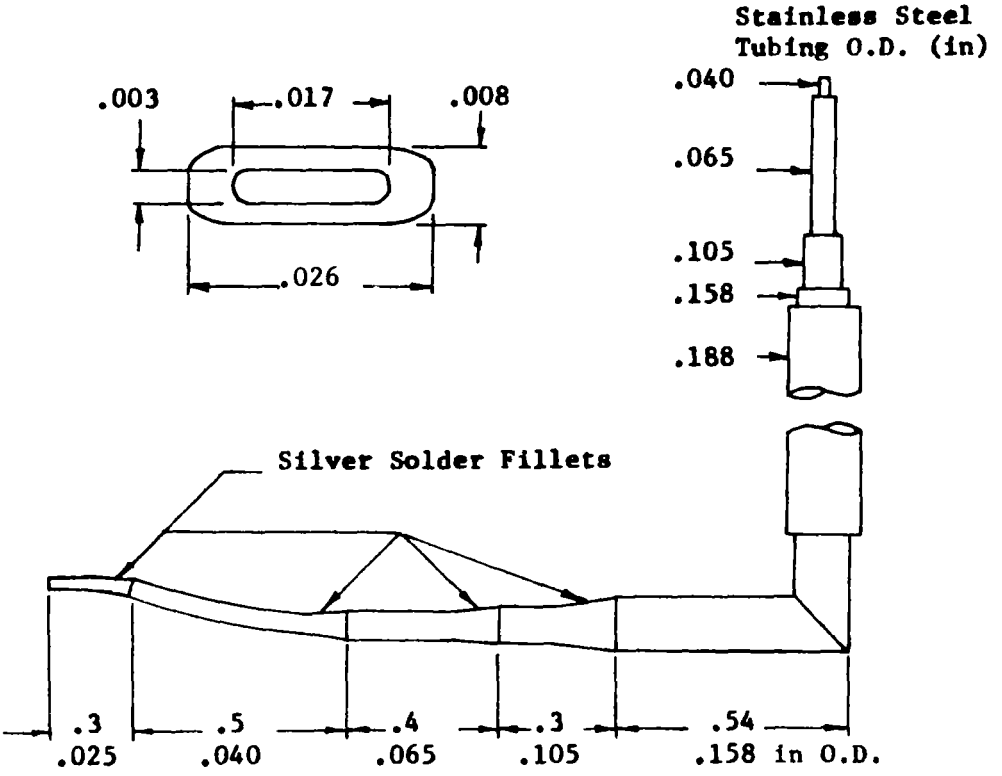

(b) Pitot Probe.

Figure 17. Pressure Instrumentation.

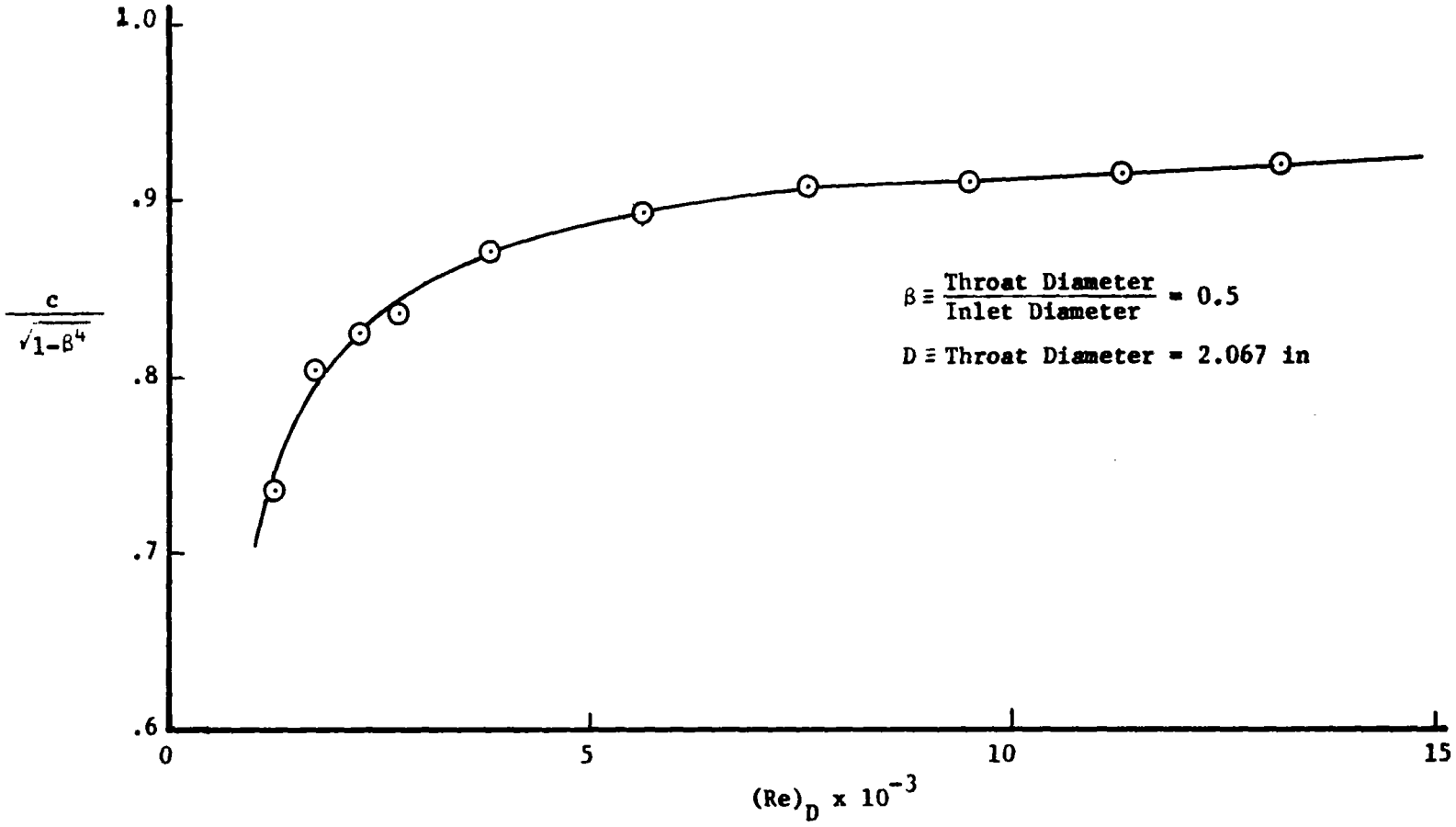

Figure 18. Flow Nozzle Calibration Curve.

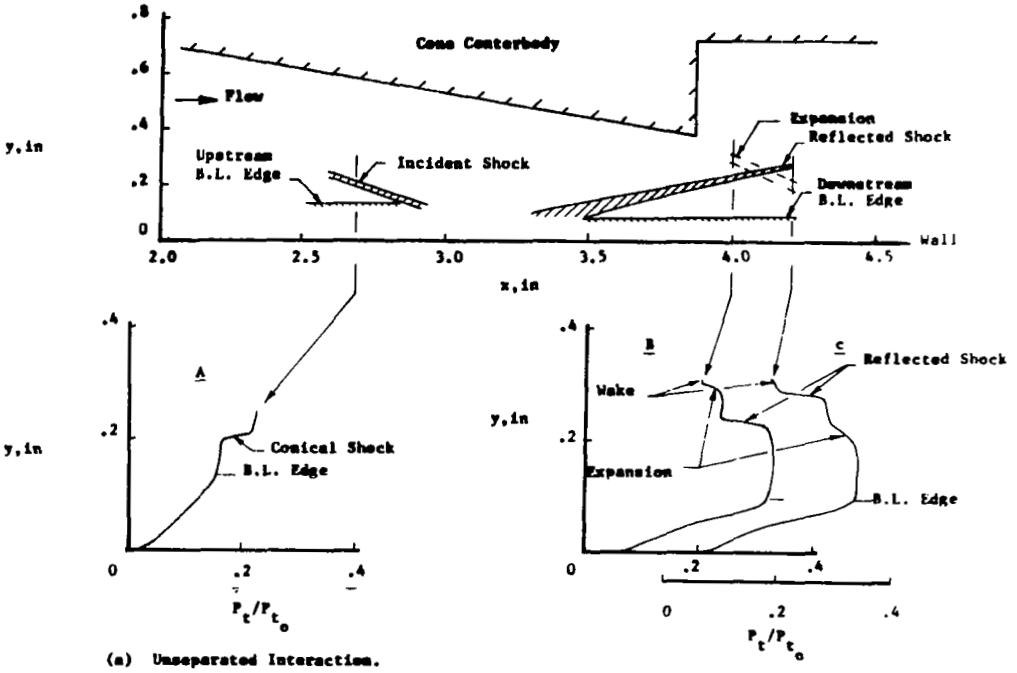

(a) Unseparated Interaction.

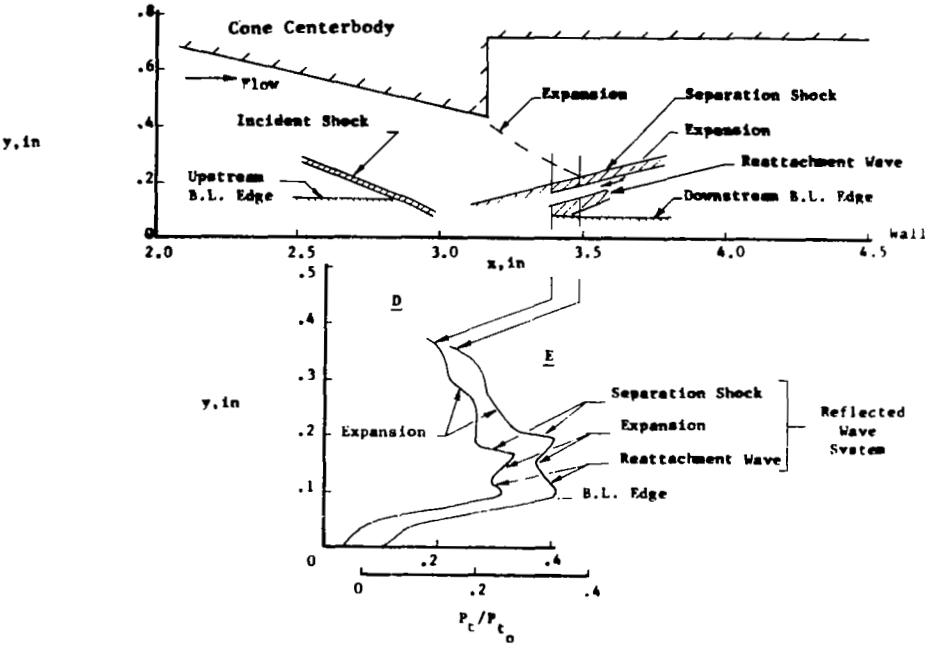

(b) Separated Interaction.

Figure 19. Interpretation of Pitot-Pressure Plots.

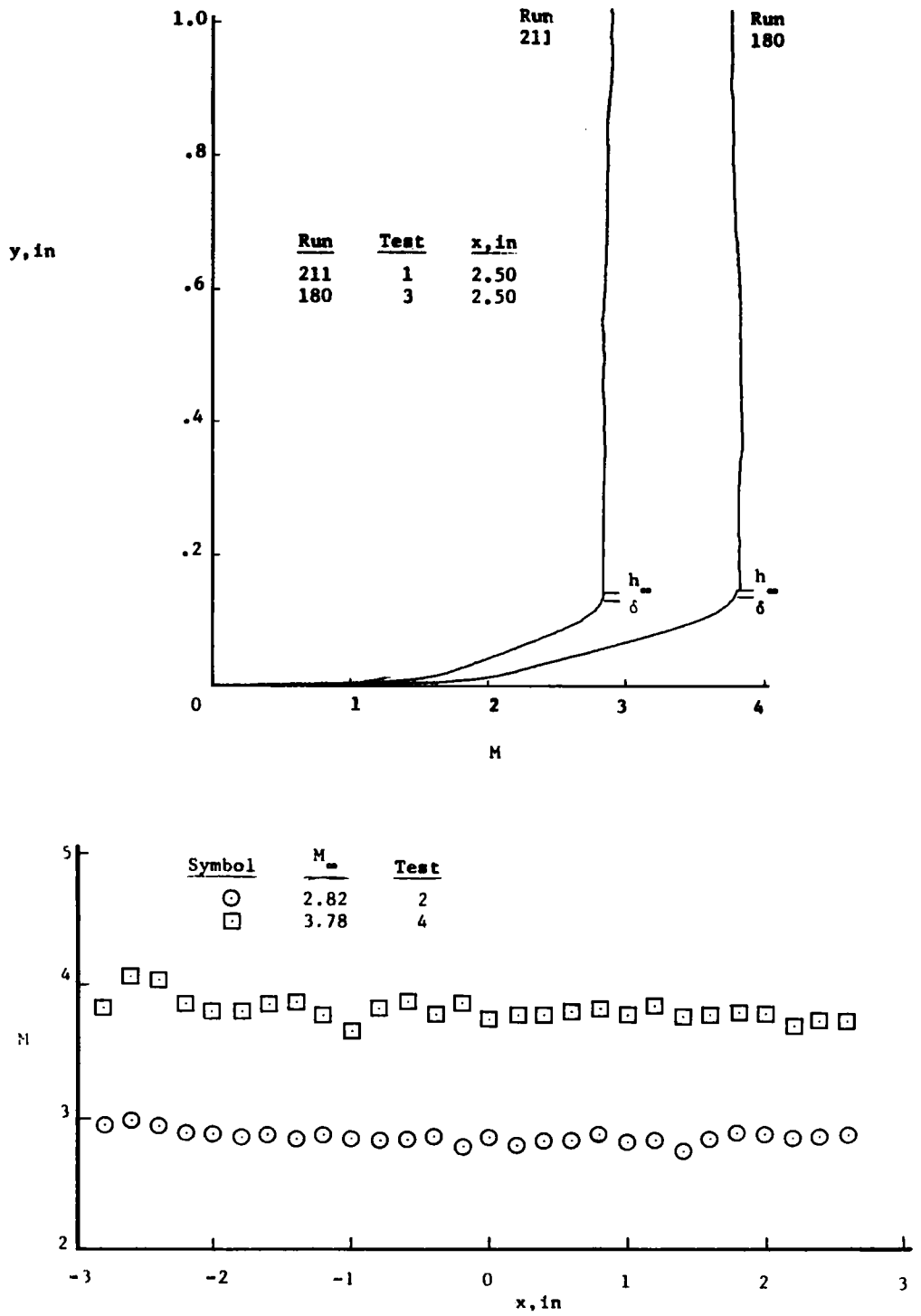

Figure 20. Test-Section Mach Number Profiles.

Symbol	M_∞	Test No.	Run No.
⊙	2.82	1	211
⊡	3.78	3	180

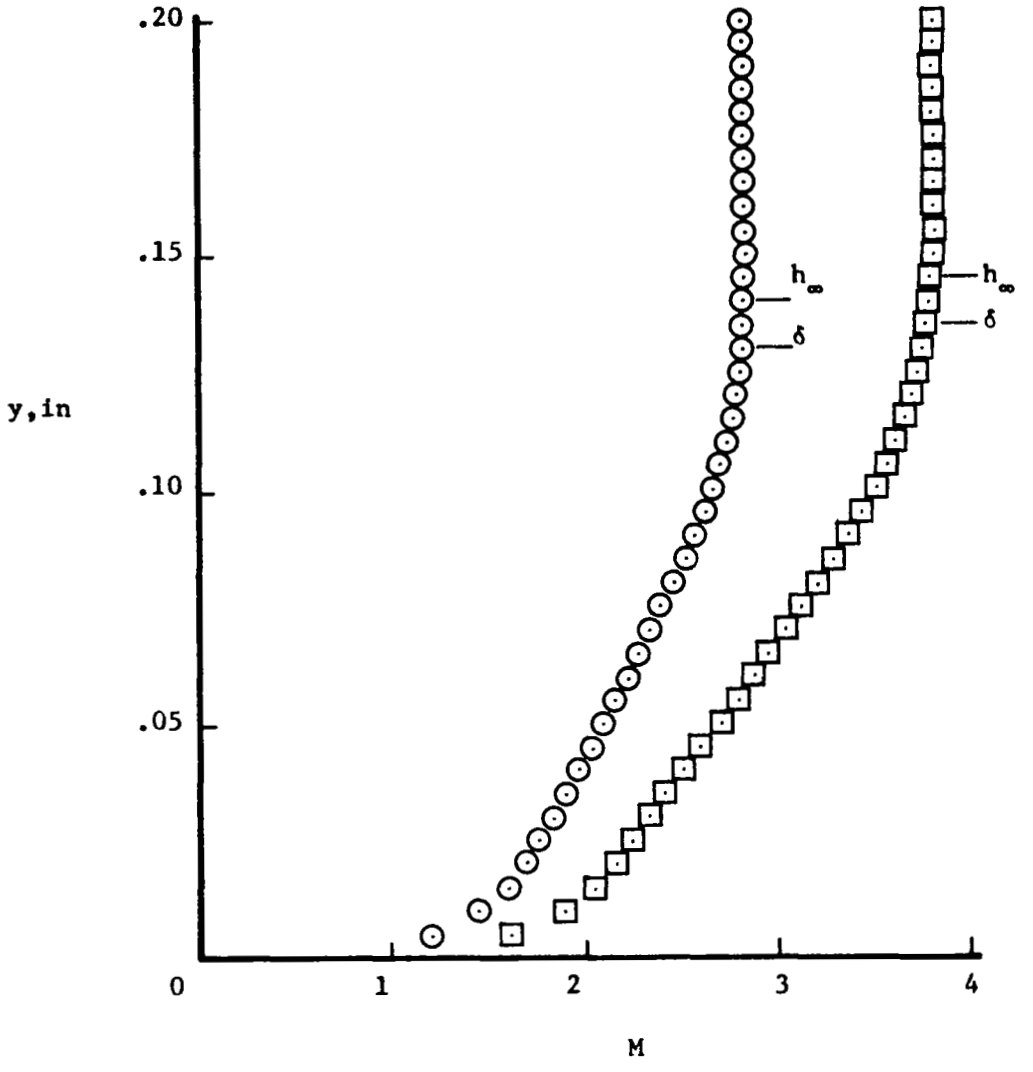

Figure 21. Boundary-Layer Mach Number Profiles.

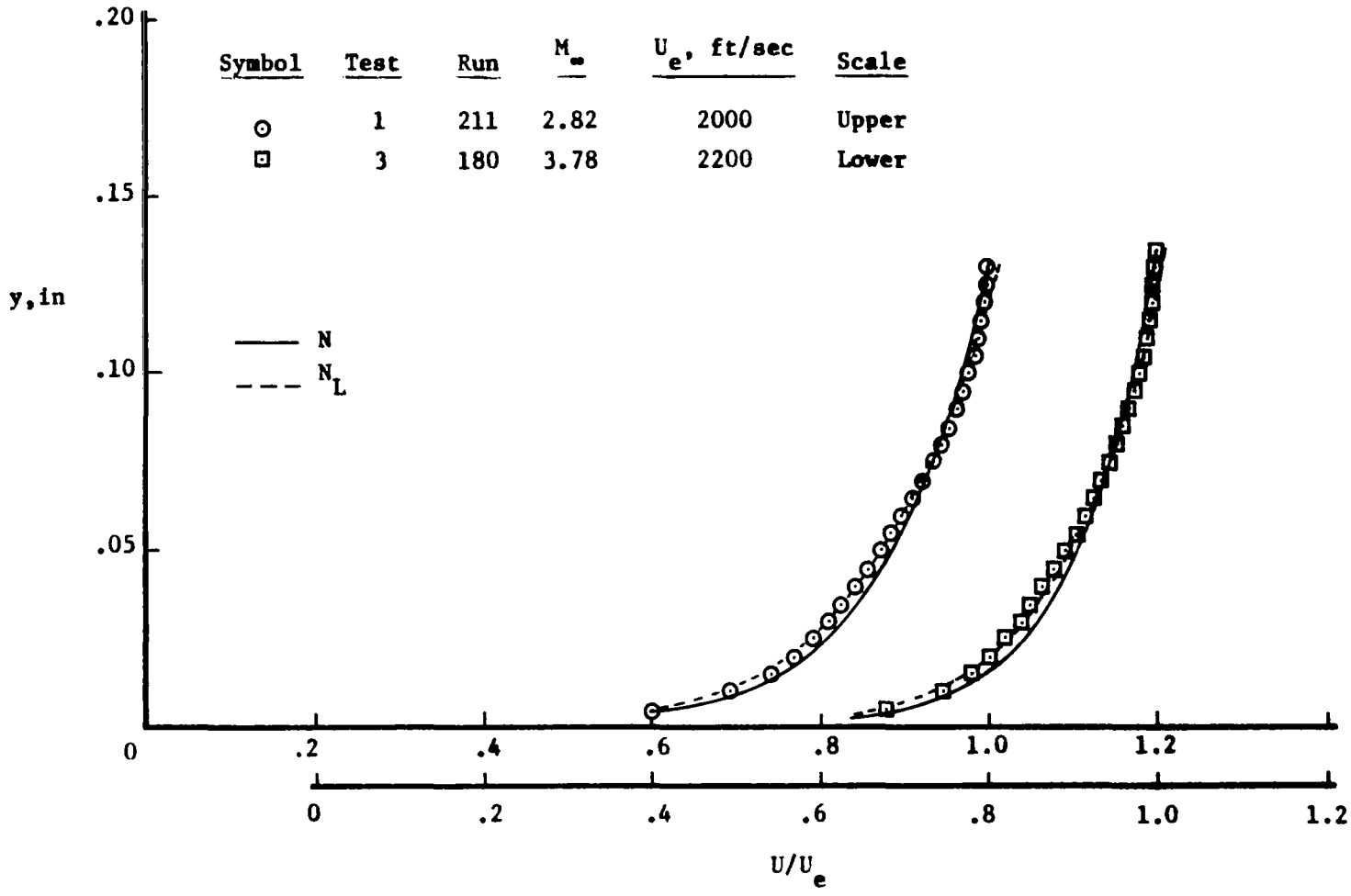

Figure 22. Boundary-Layer Velocity Profiles.

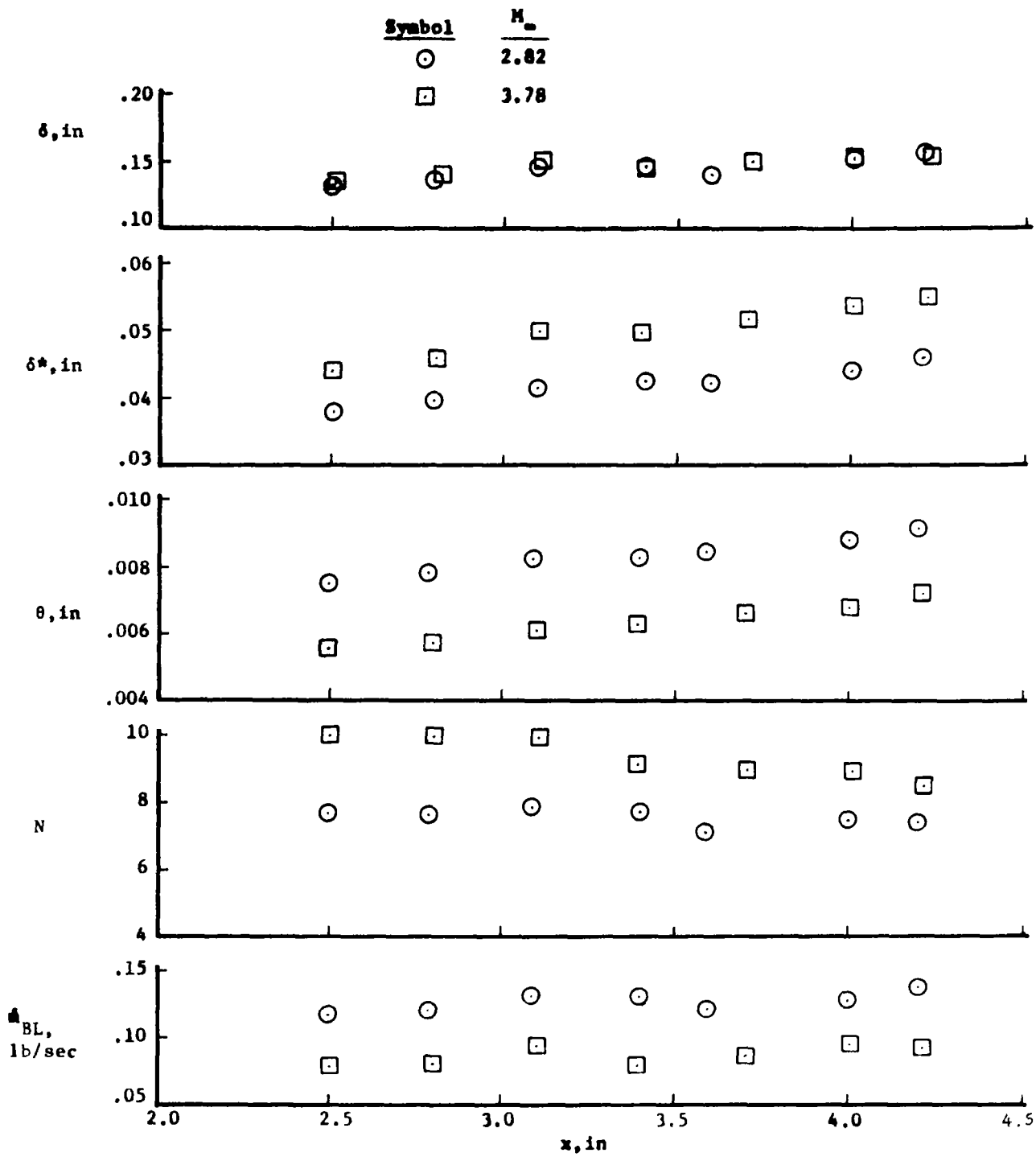

Figure 23. Basic Boundary-Layer Properties.

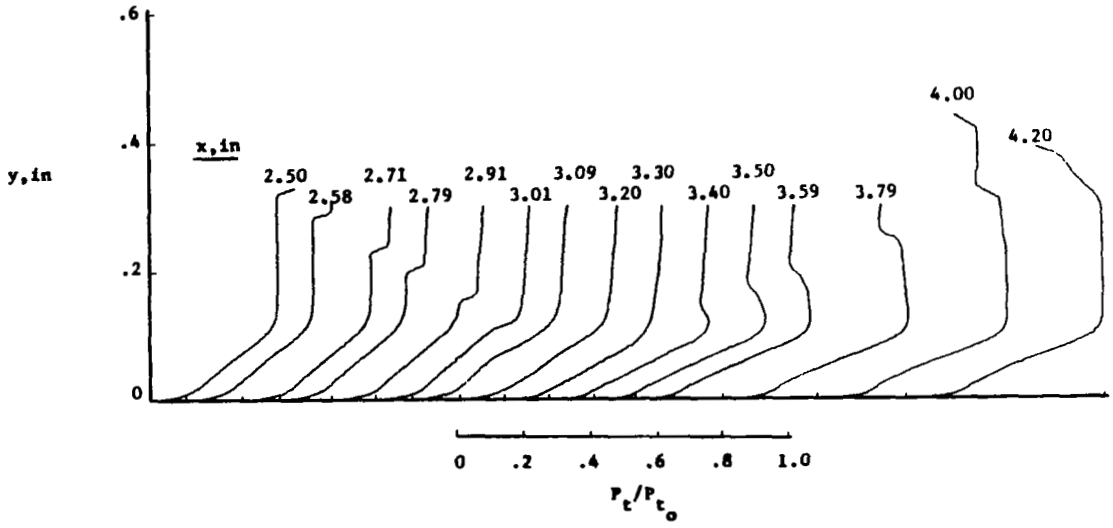

(a) Pitot Pressure Surveys.

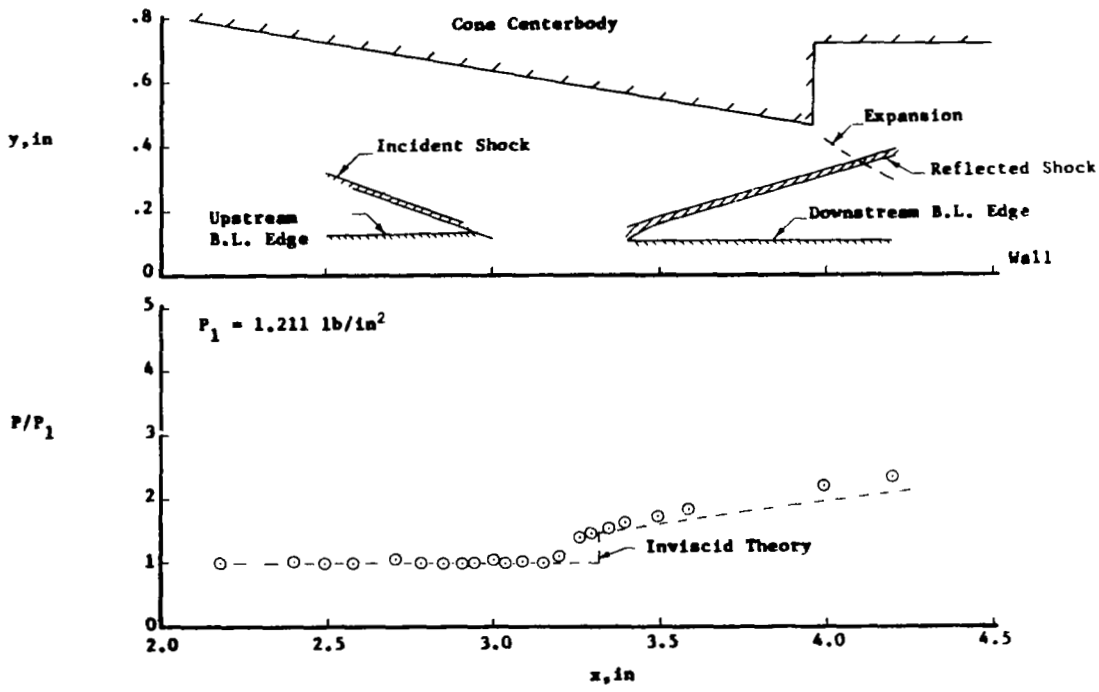

(b) Flow Field and Surface Static-Pressure Distribution.

Figure 24. Solid-Wall Shock-Interaction Region Properties, 10-Degree Cone at M_∞ = 2.82.

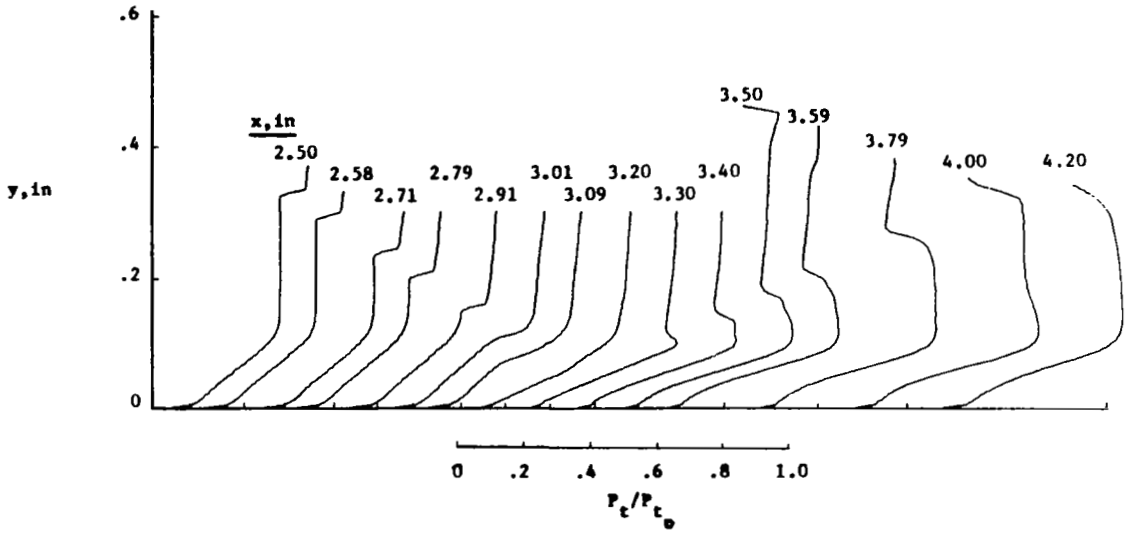

(a) Pitot Pressure Surveys.

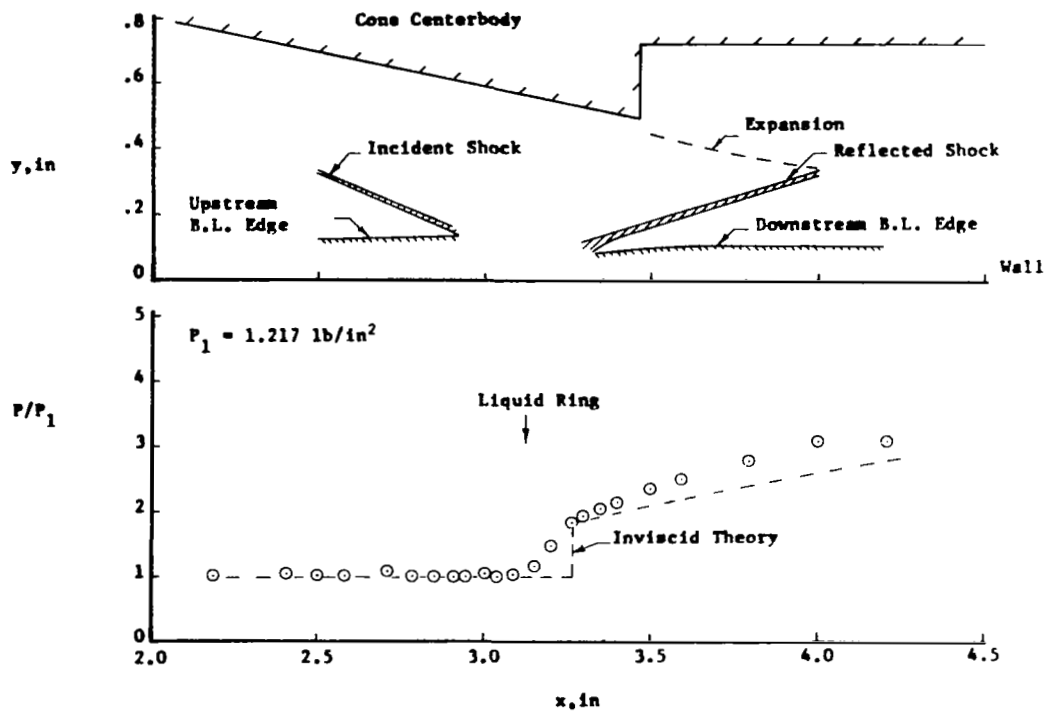

(b) Flow Field and Surface Static-Pressure Distribution.

Figure 25. Solid-Wall Shock-Interaction Region Properties, 12-Degree Cone at M_∞ = 2.82.

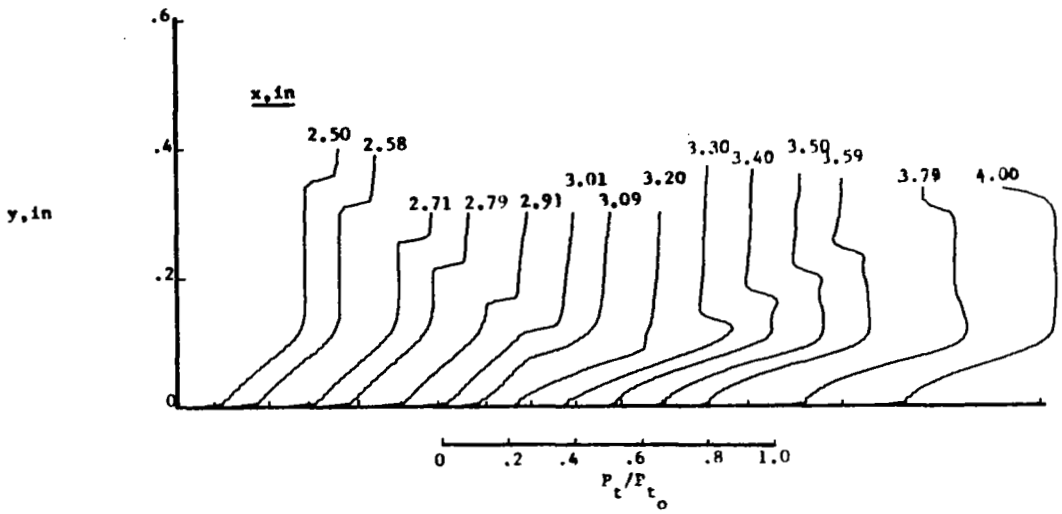

(a) Pitot Pressure Surveys.

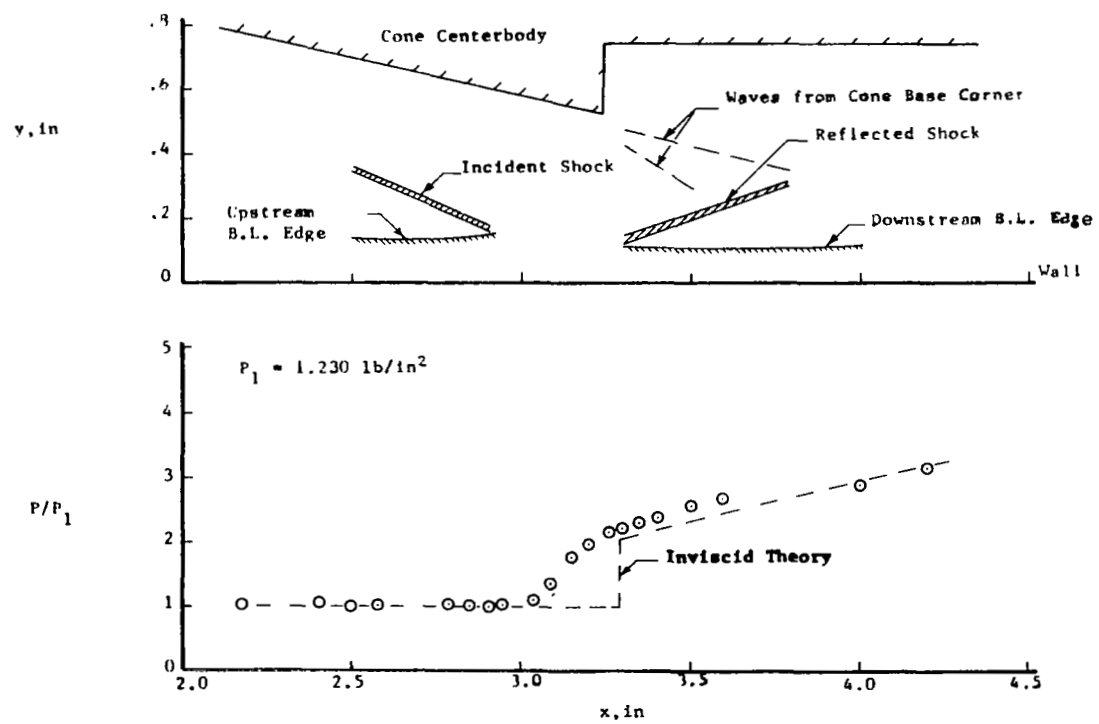

(b) Flow Field and Surface Static-Pressure Distribution.

Figure 26. Solid-Wall Shock-Interaction Region Properties, 13-Degree Cone at M_∞ = 2.82.

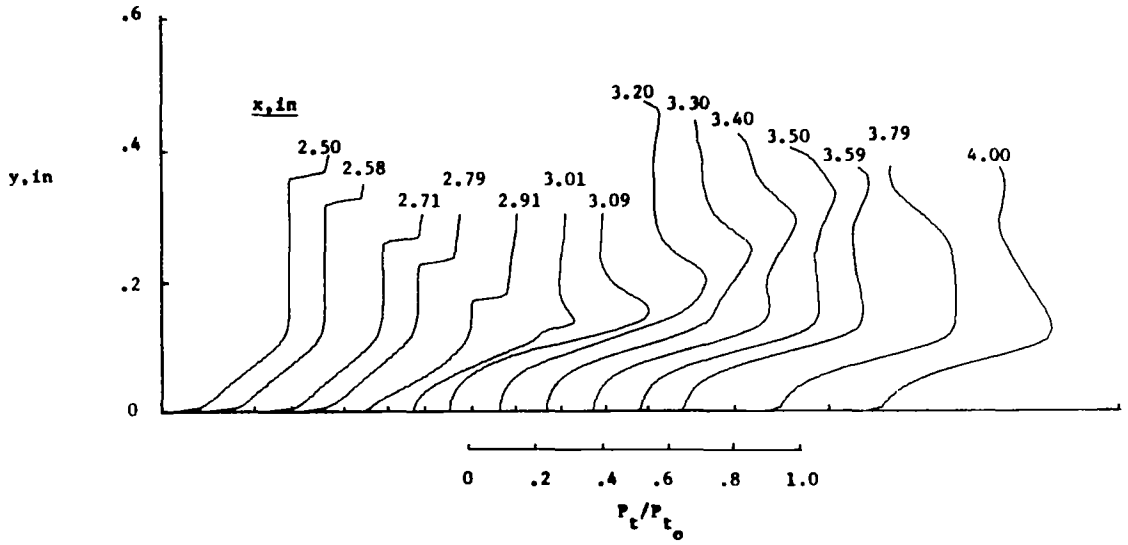

(a) Pitot Pressure Surveys.

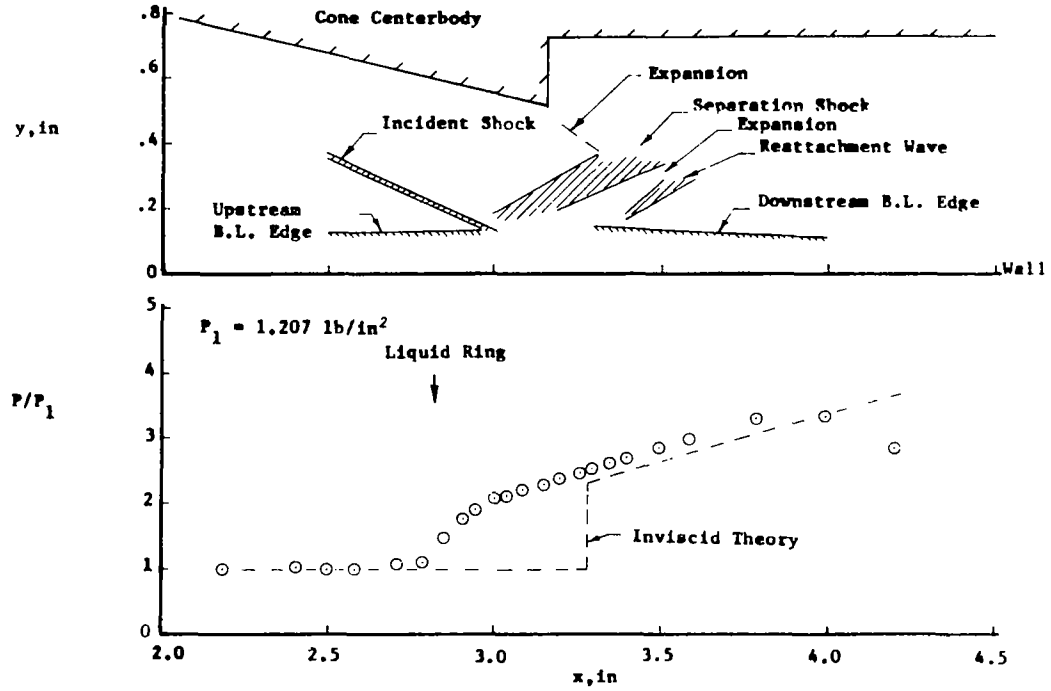

(b) Flow Field and Surface Static-Pressure Distribution.

Figure 27. Solid-Wall Shock-Interaction Region Properties, 14-Degree Cone at M_∞ = 2.82.

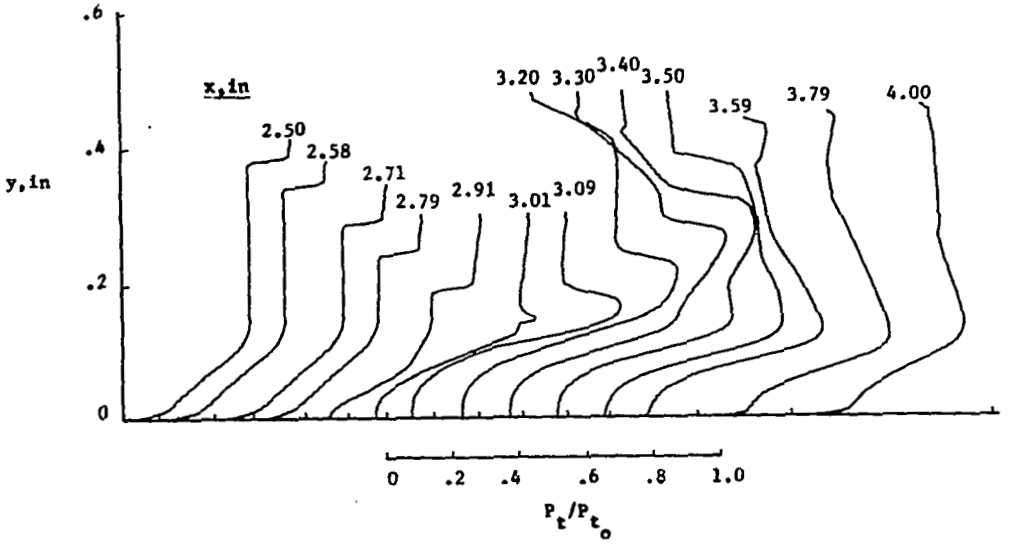

(a) Pitot Pressure Surveys.

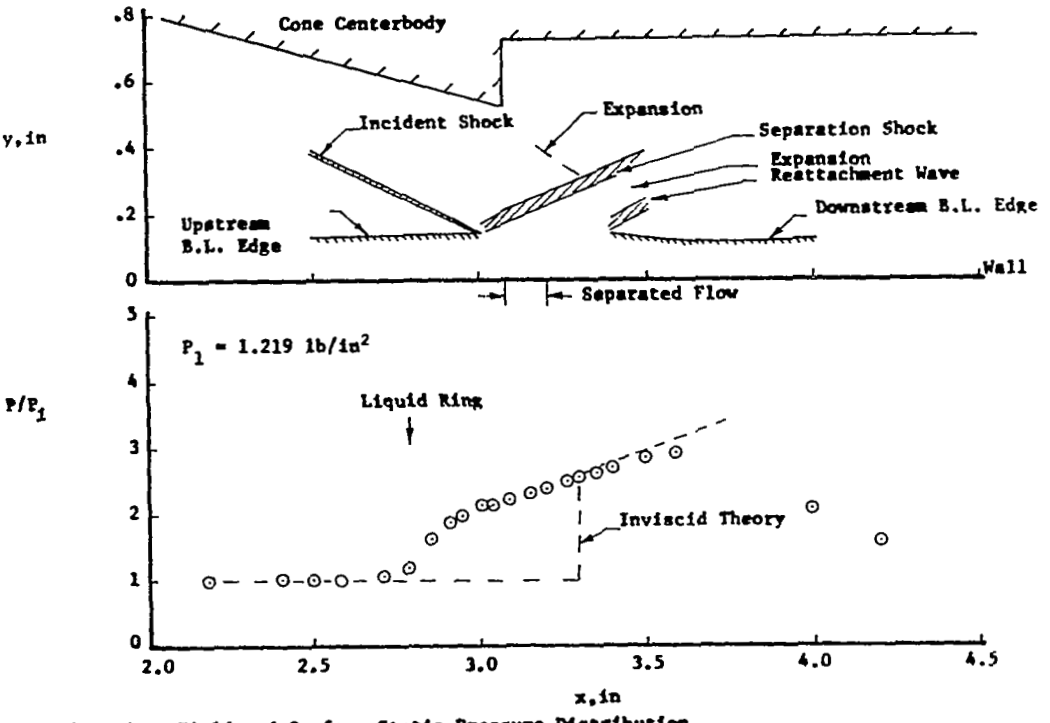

(b) Flow Field and Surface Static-Pressure Distribution.

Figure 28. Solid-Wall Shock-Interaction Region Properties, 15-Degree Cone at M_∞ = 2.82.

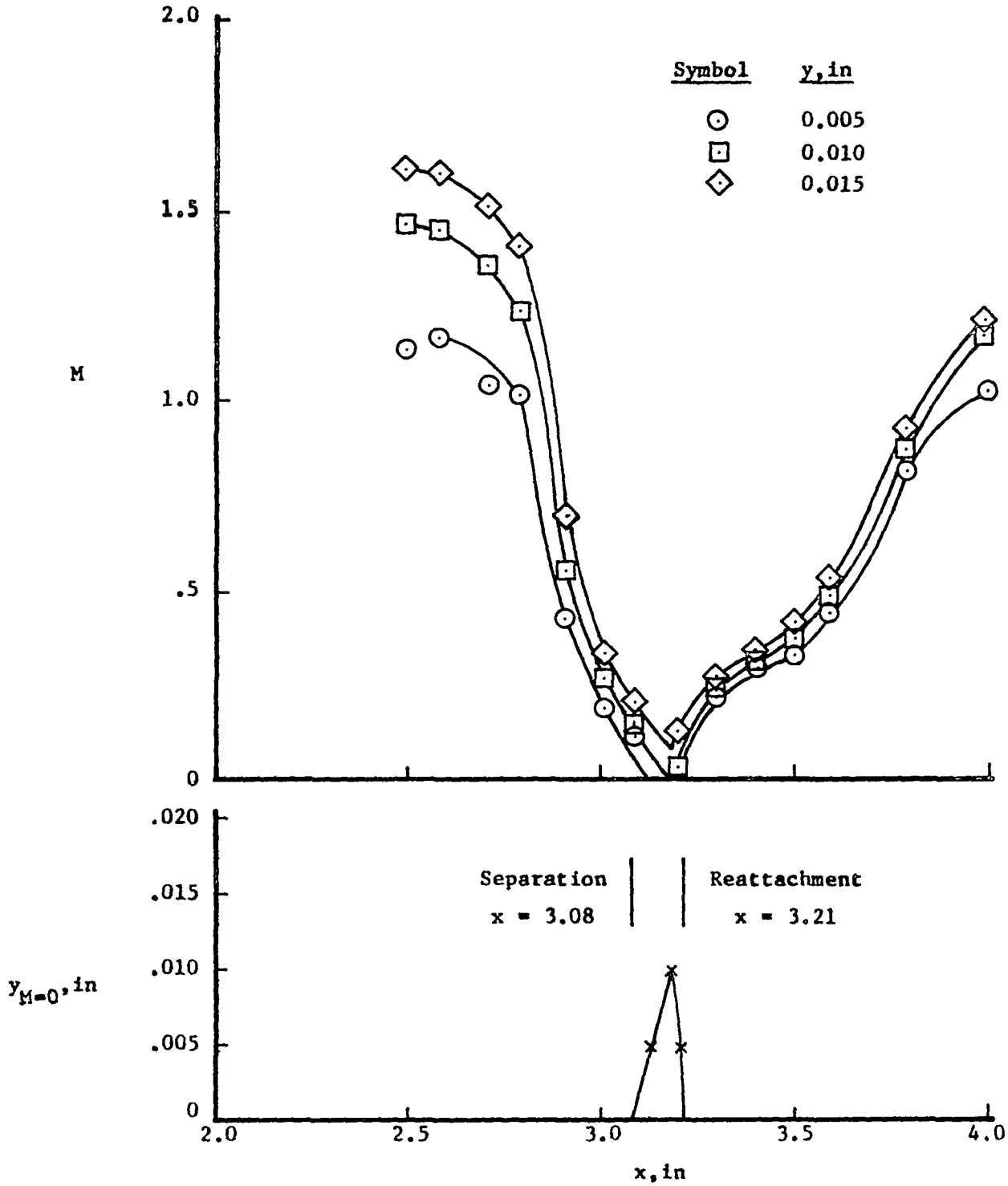

Figure 29. Separation and Reattachment Points, 15-Degree Cone at $M_\infty = 2.82$.

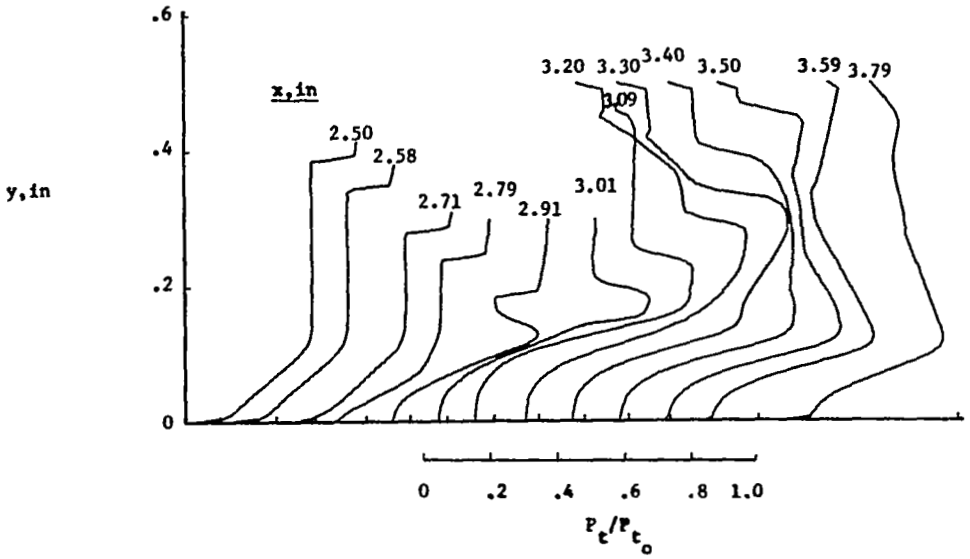

(a) Pitot Pressure Surveys.

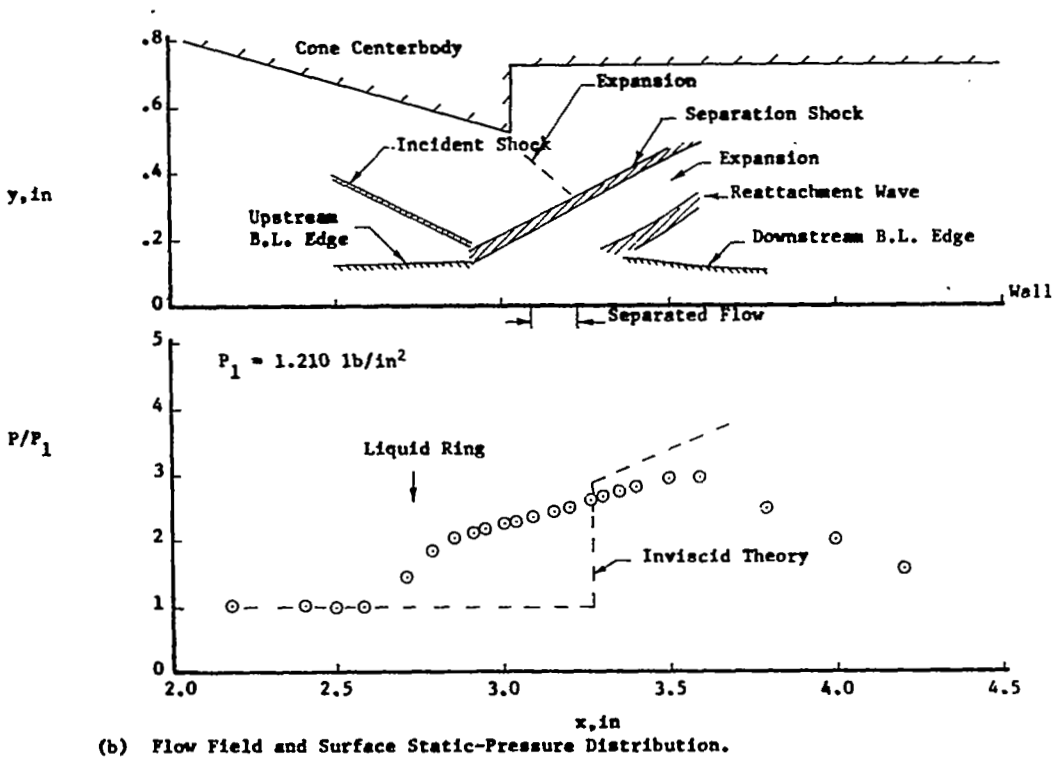

(b) Flow Field and Surface Static-Pressure Distribution.

Figure 30. Solid-Wall Shock-Interaction Region Properties, 16-Degree Cone at M_∞ = 2.82.

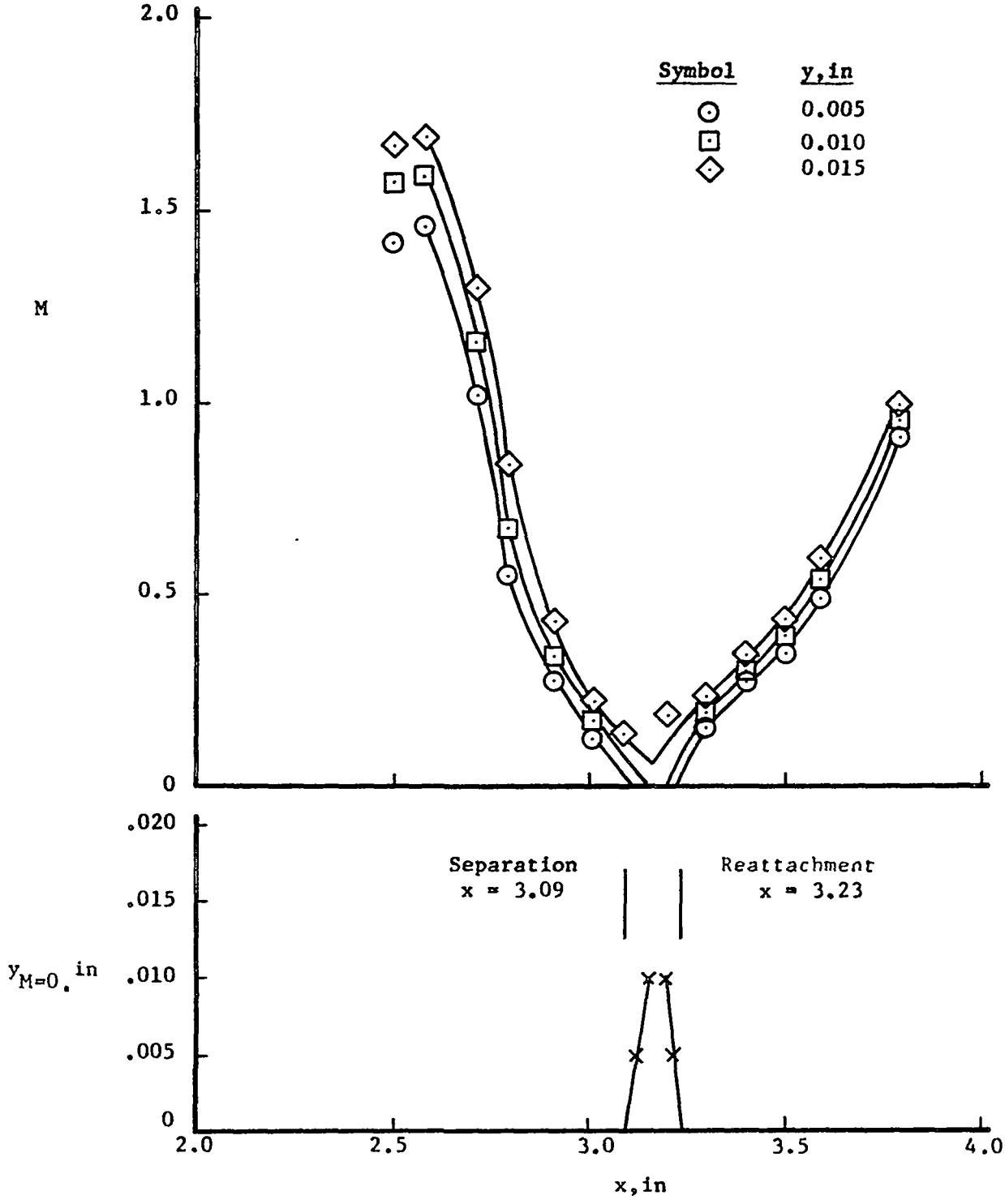

Figure 31. Separation and Reattachment Points, 16-Degree Cone at M_∞ = 2.82.

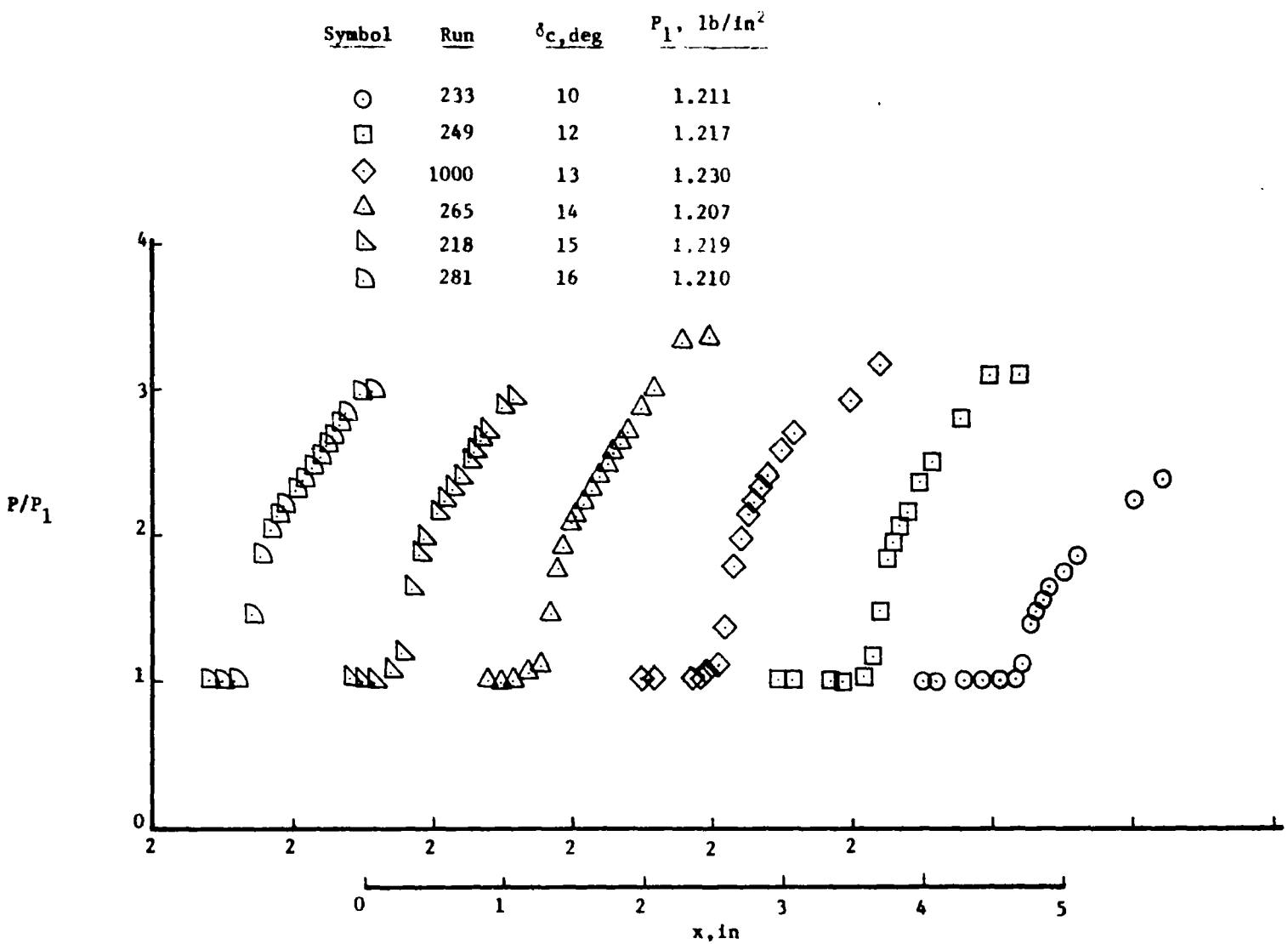

Figure 32. Summary of Surface Static-Pressure Distributions, Solid Wall, $M_\infty = 2.82$.

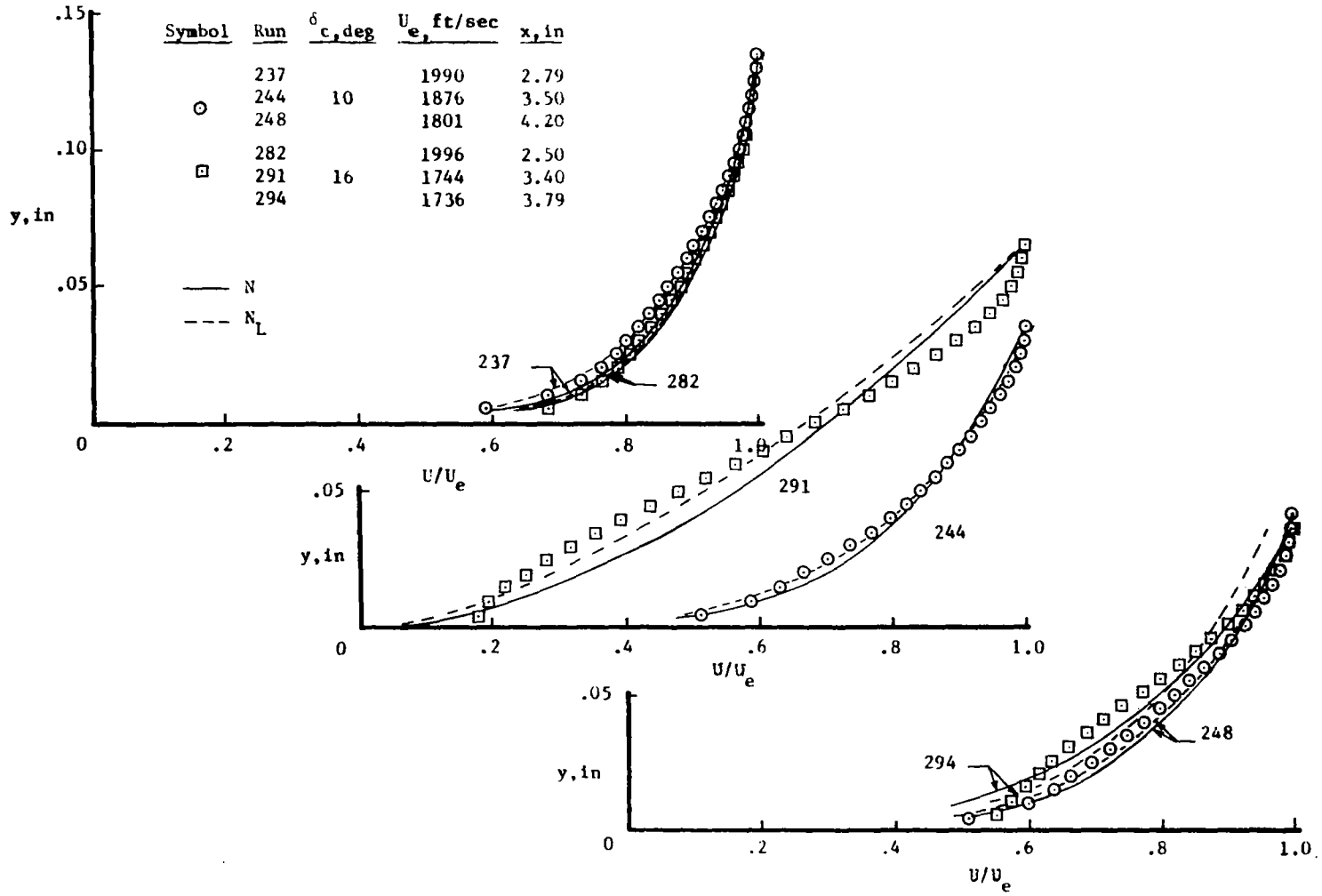

Figure 33. Typical Boundary-Layer Velocity Profiles, Solid Wall, $M_\infty = 2.82$.

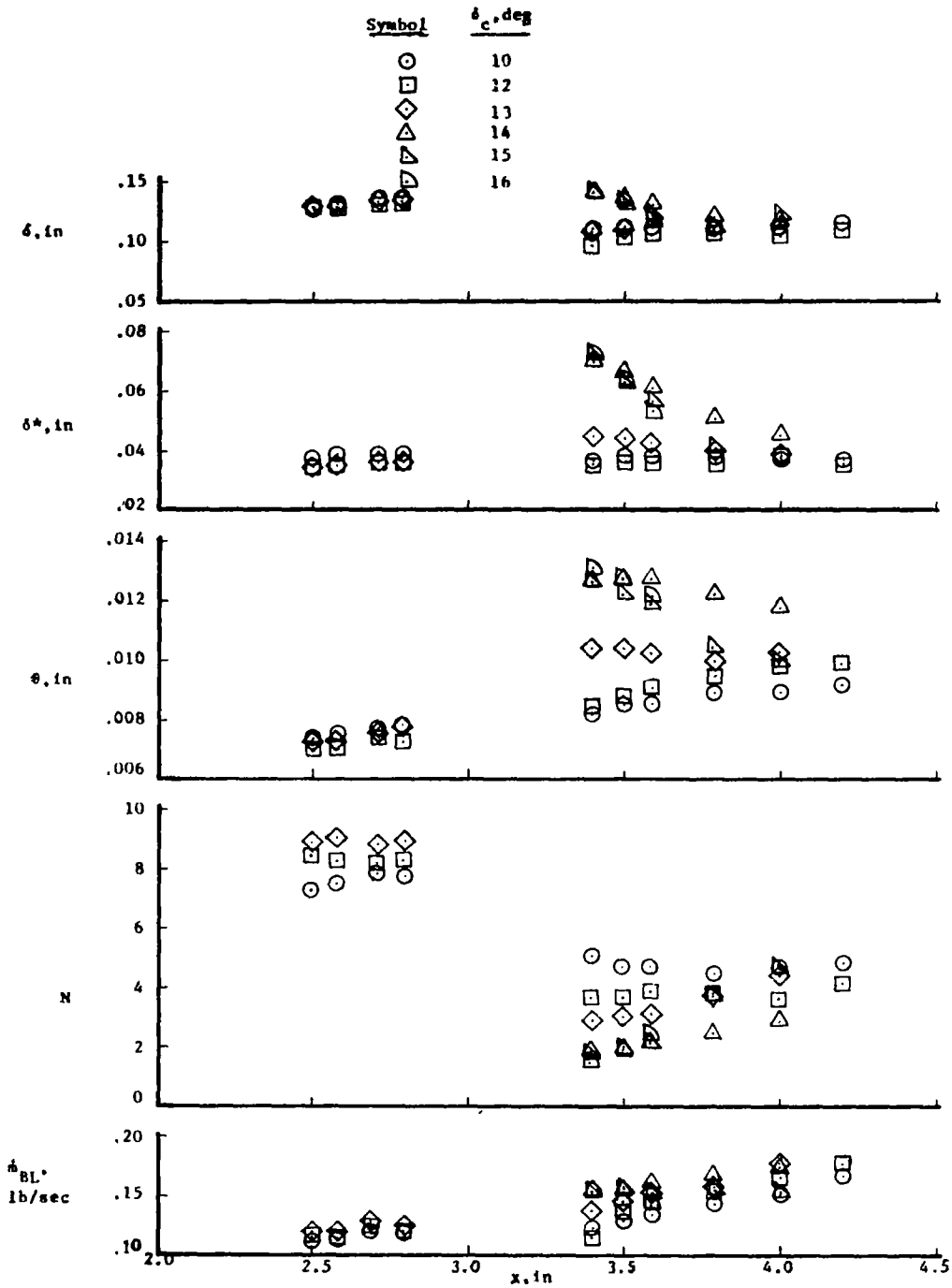

Figure 34. Summary of Boundary-Layer Properties, Solid Wall, M_∞ = 2.82.

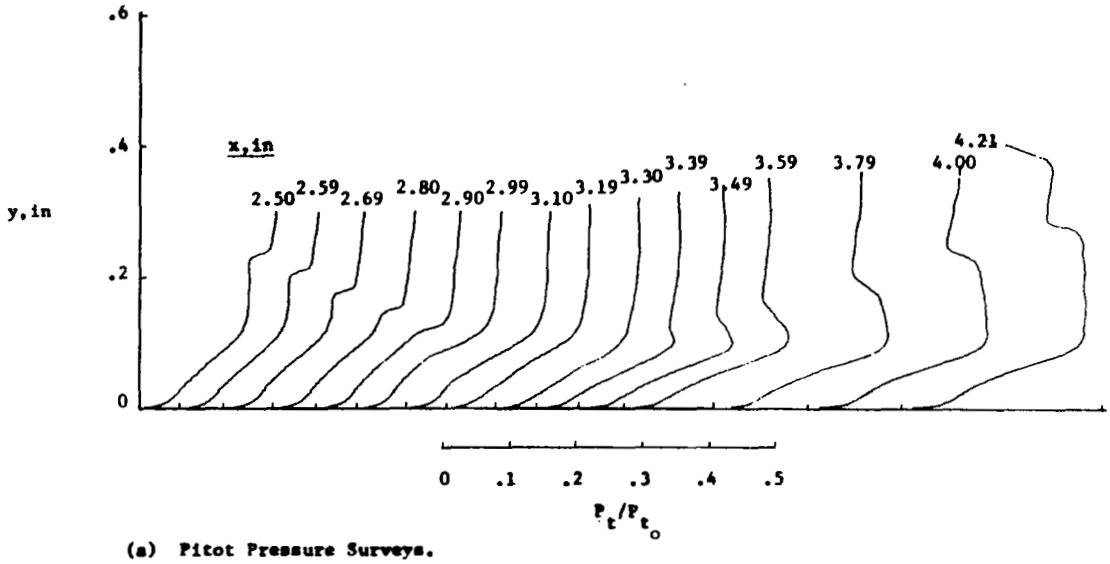

(a) Pitot Pressure Surveys.

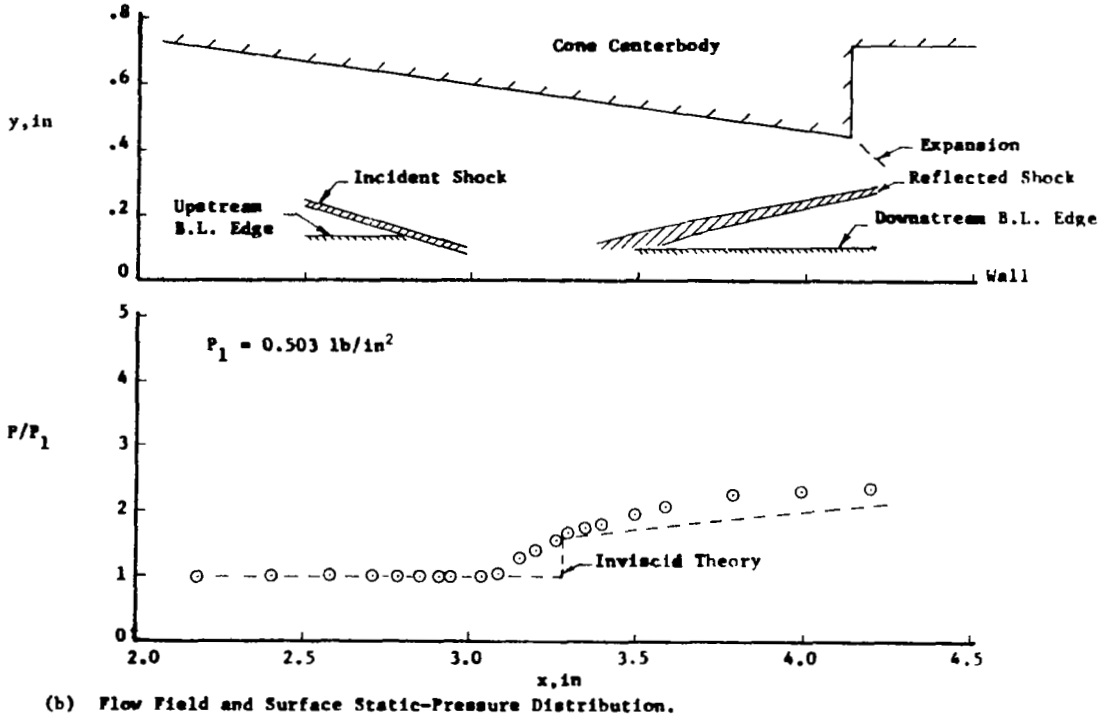

(b) Flow Field and Surface Static-Pressure Distribution.

Figure 35. Solid-Wall Shock-Interaction Region Properties, 8-Degree Cone at M_∞ = 3.78.

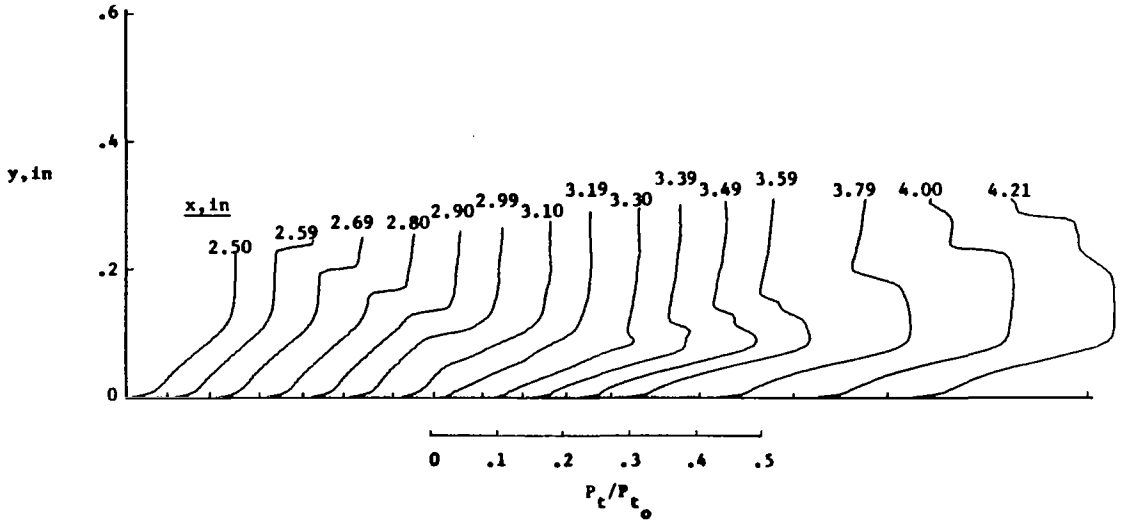

(a) Pitot Pressure Surveys.

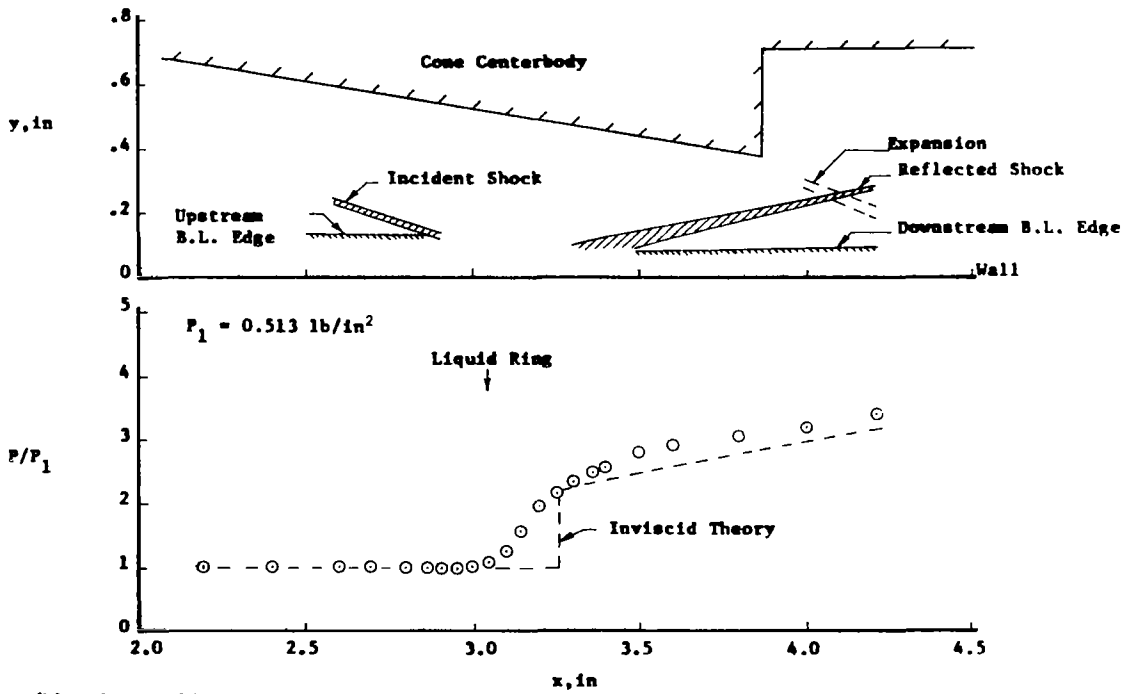

(b) Flow Field and Surface Static-Pressure Distribution.

Figure 36. Solid-Wall Shock-Interaction Region Properties, 10-Degree Cone at M_∞ = 3.78.

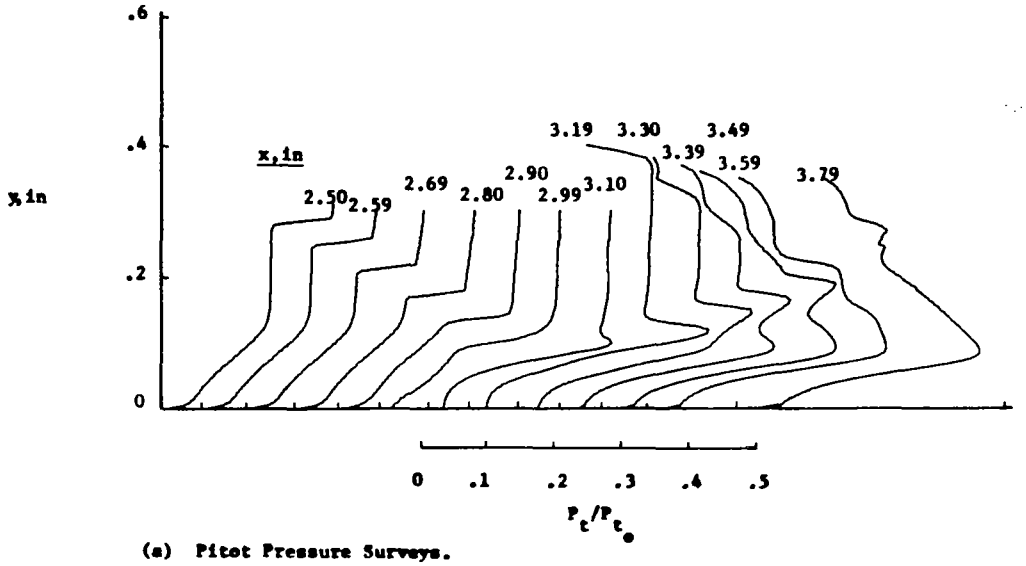

(a) Pitot Pressure Surveys.

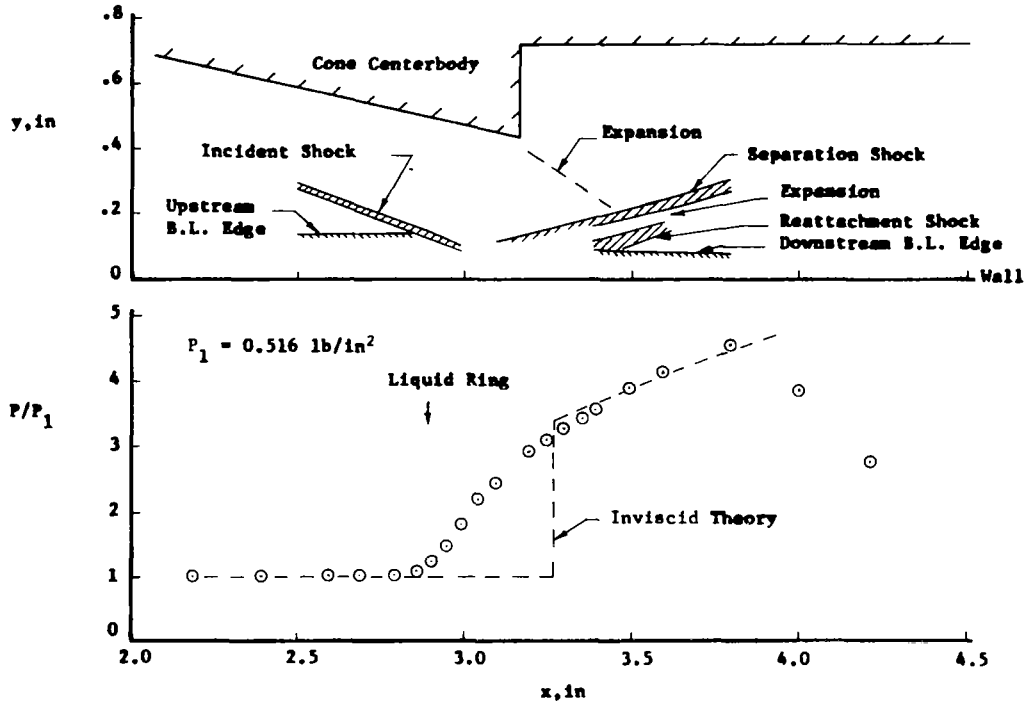

(b) Flow Field and Surface Static-Pressure Distribution.

Figure 37. Solid-Wall Shock-Interaction Region Properties, 13-Degree Cone at M_∞ = 3.78.

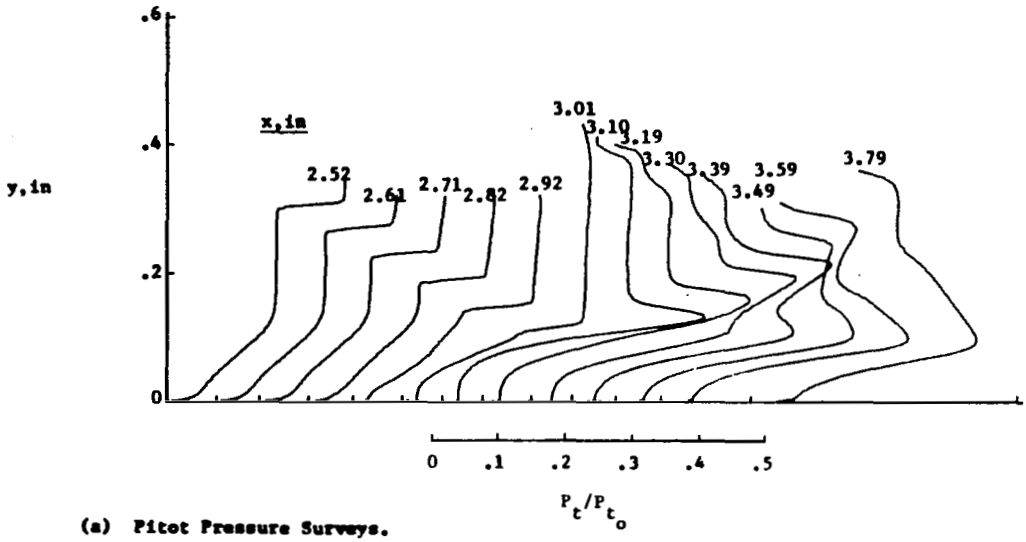

(a) Pitot Pressure Surveys.

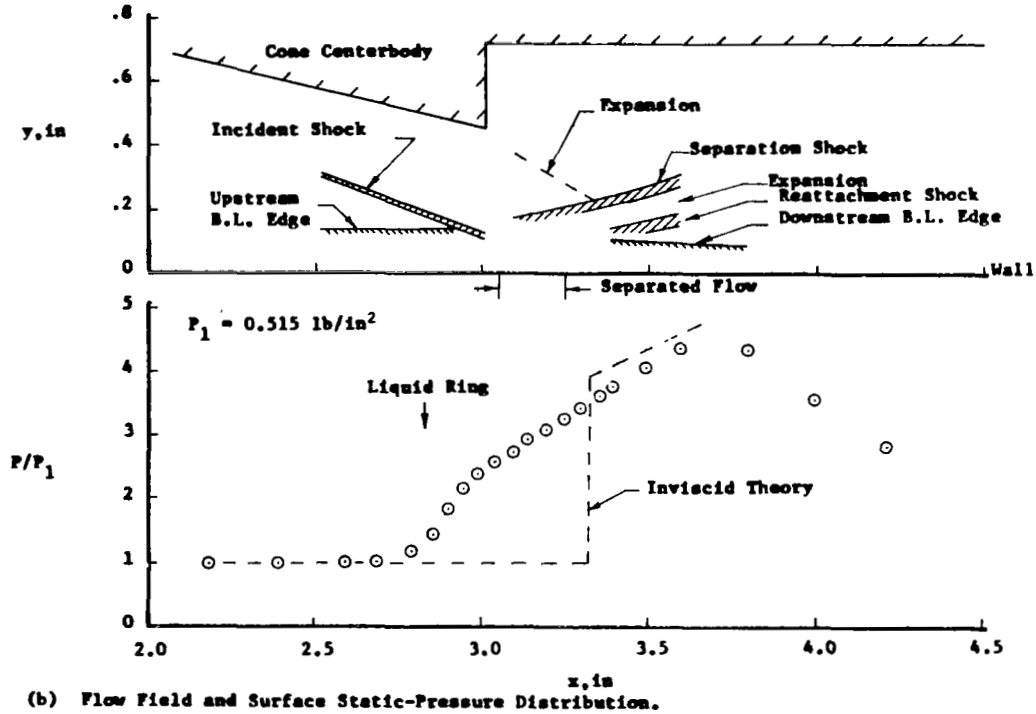

(b) Flow Field and Surface Static-Pressure Distribution.

Figure 38. Solid-Wall Shock-Interaction Region Properties, 14-Degree Cone at M_∞ = 3.78.

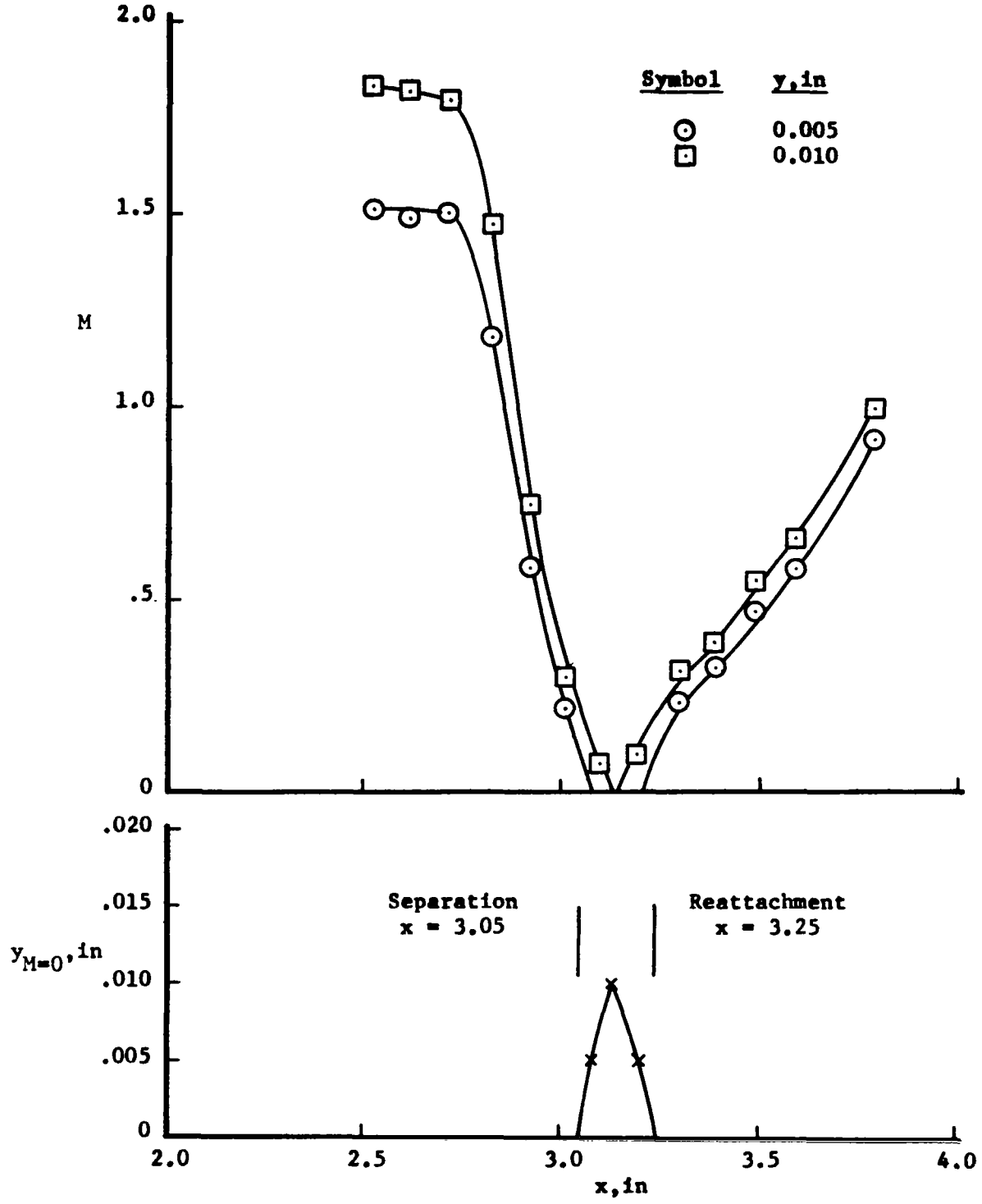

Figure 39. Separation and Reattachment Points, 14-Dgree Cone at M_∞ = 3.78.

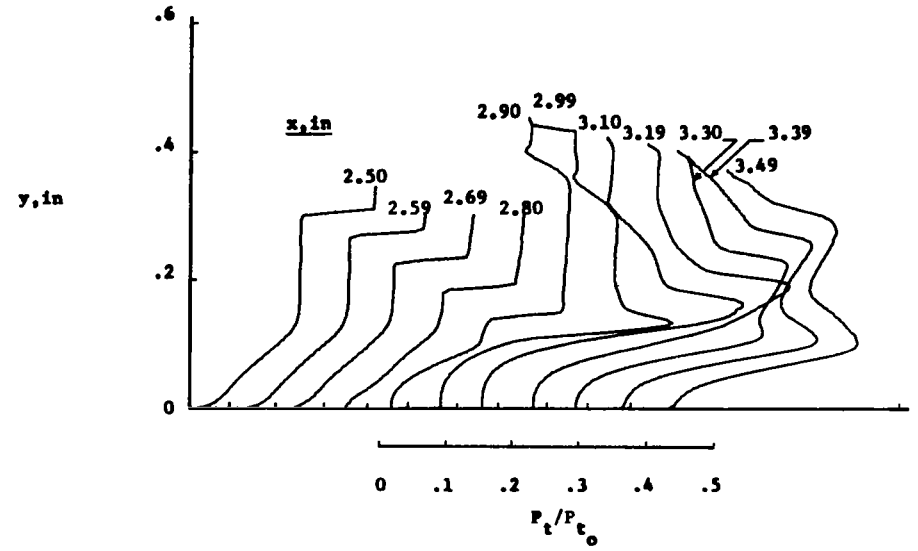

(a) Pitot Pressure Surveys.

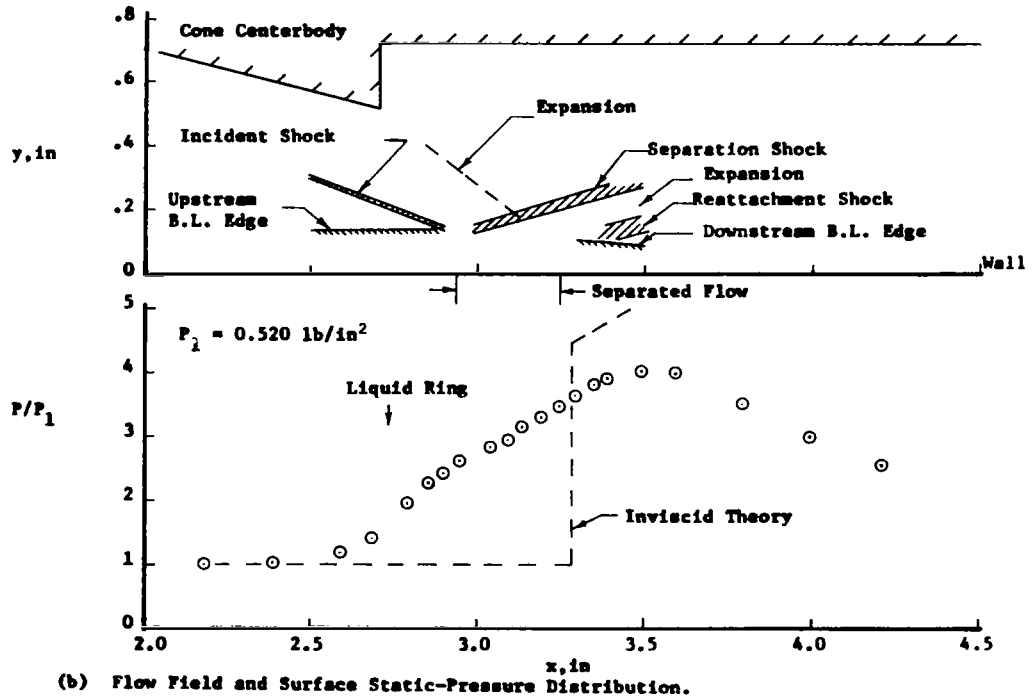

(b) Flow Field and Surface Static-Pressure Distribution.

Figure 40. Solid-Wall Shock-Interaction Region Properties, 15-Degree Cone at M_∞ = 3.78.

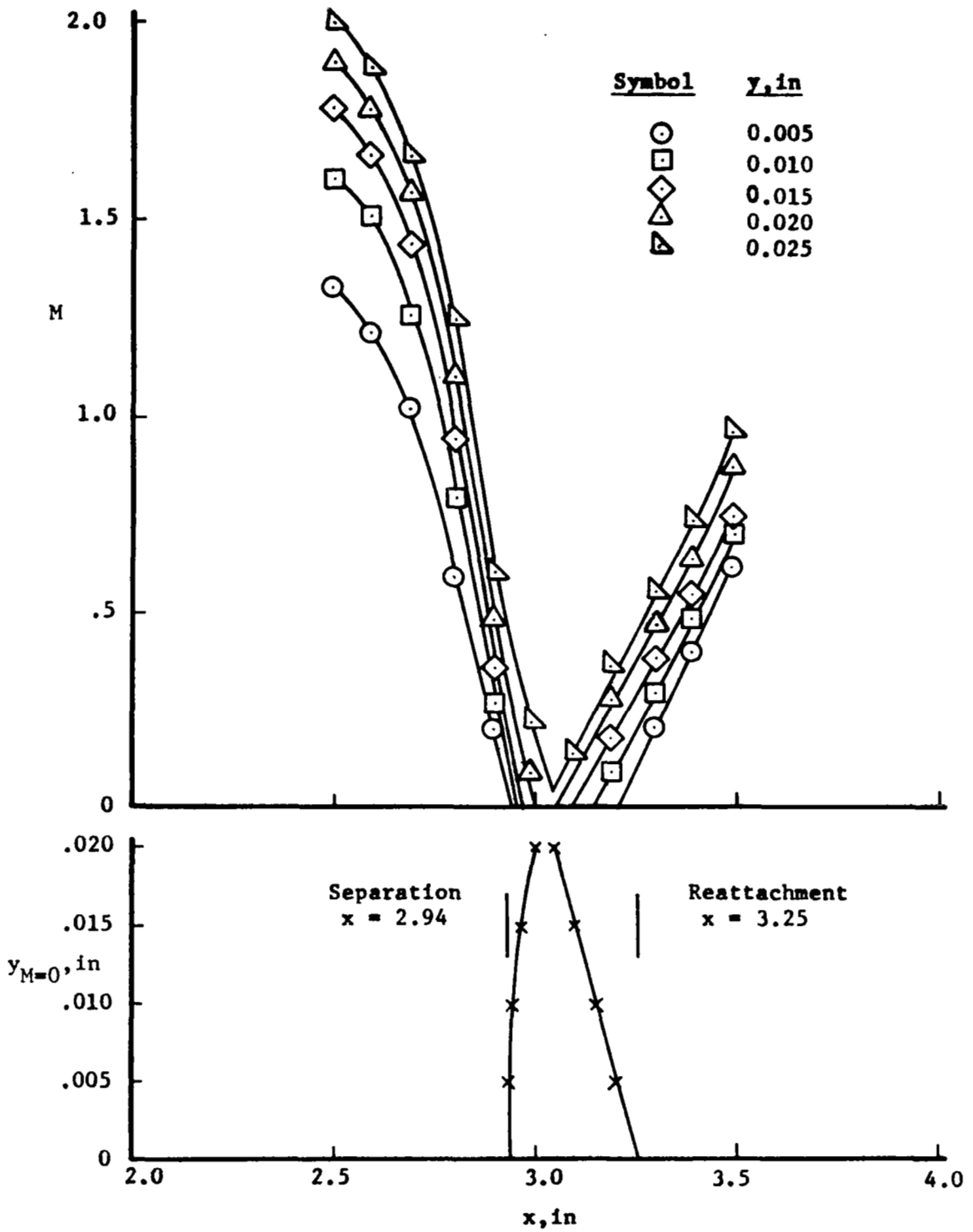

Figure 41. Separation and Reattachment Points, 15-Degree Cone at M_∞ = 3.78.

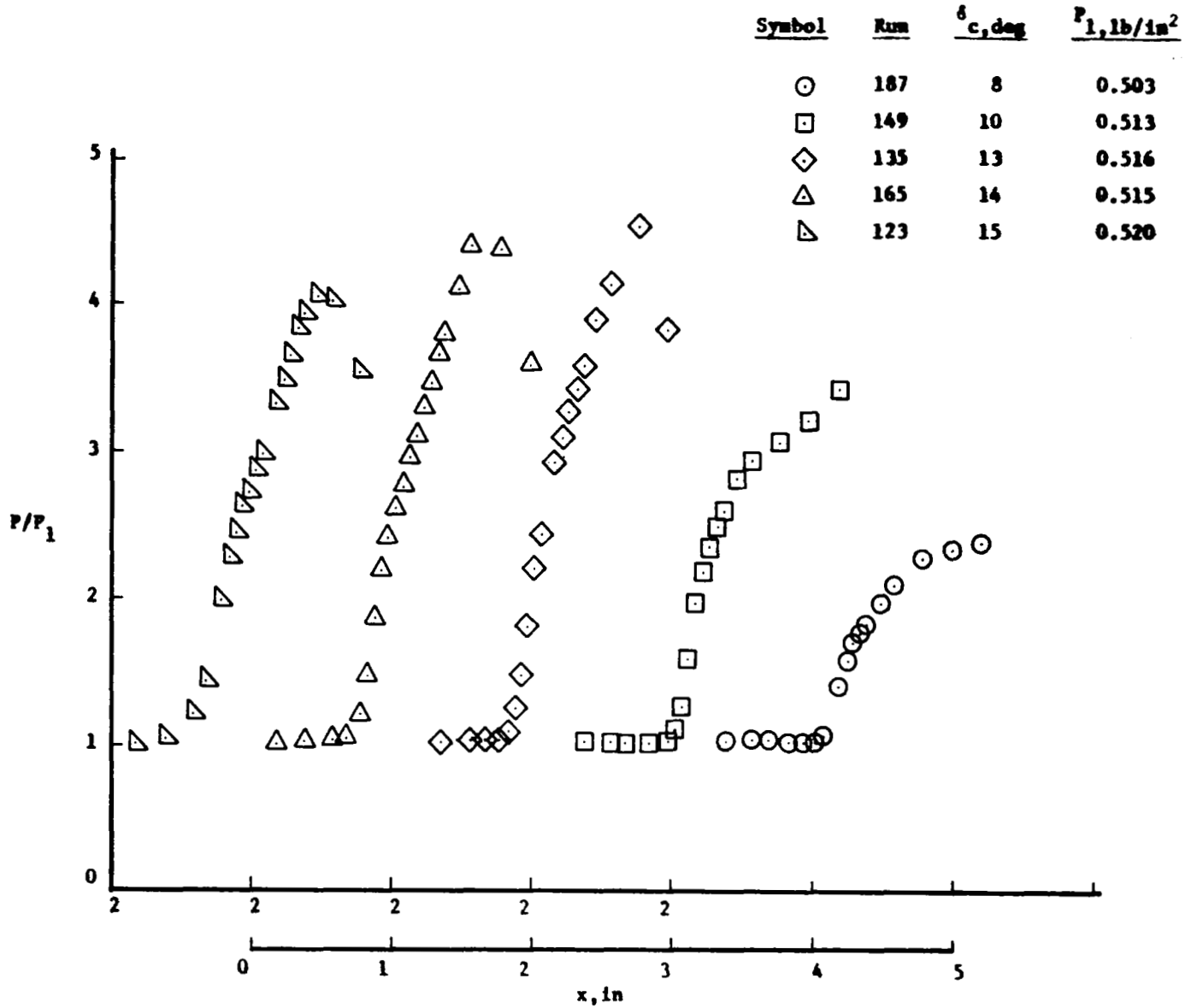

Figure 42. Summary of Surface Static-Pressure Distributions, Solid Wall, M_∞ = 3.78.

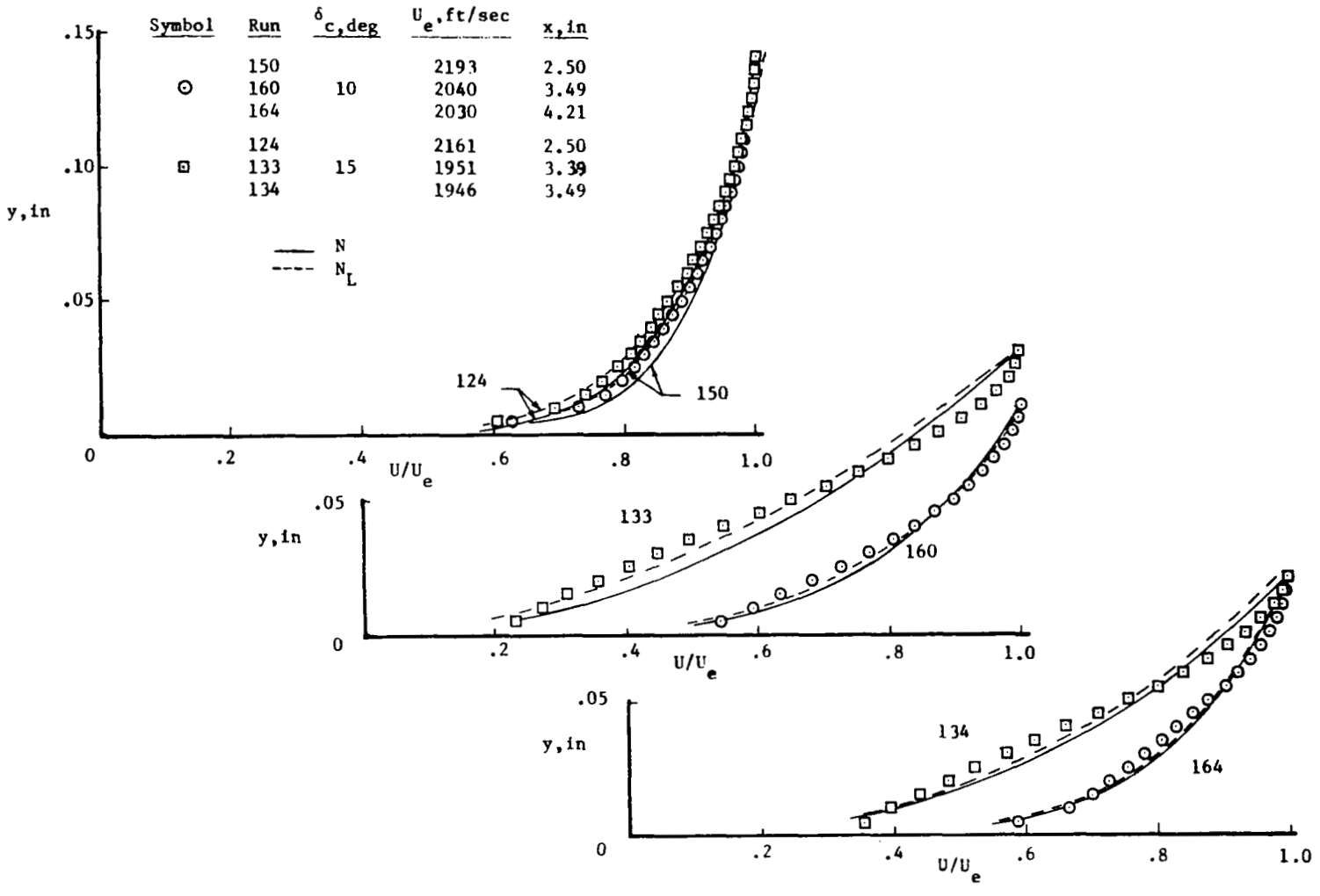

Figure 43. Typical Boundary-Layer Velocity Profiles, Solid Wall, $M_\infty = 3.78$.

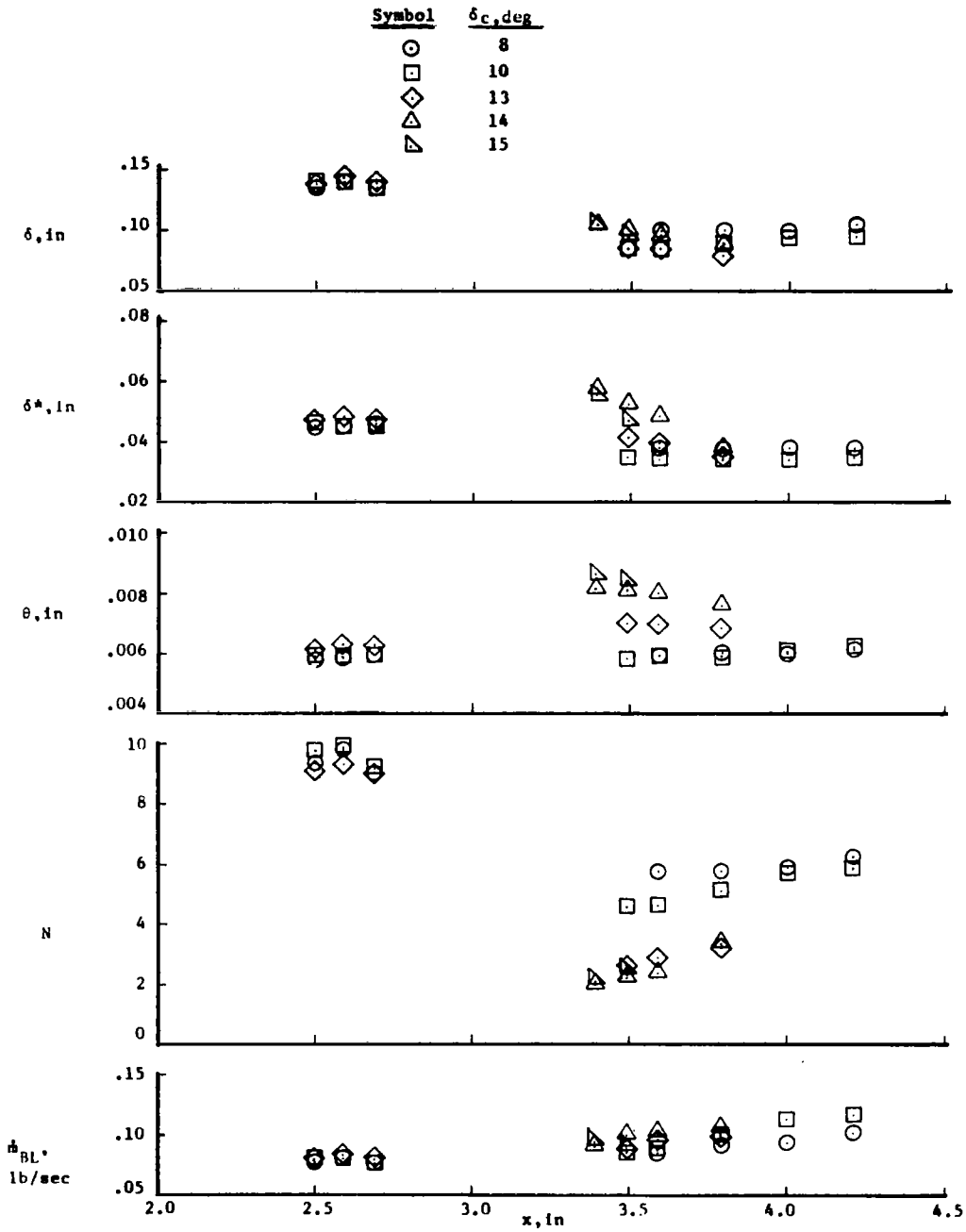

Figure 44. Summary of Boundary-Layer Properties, Solid Wall, M_∞ = 3.78.

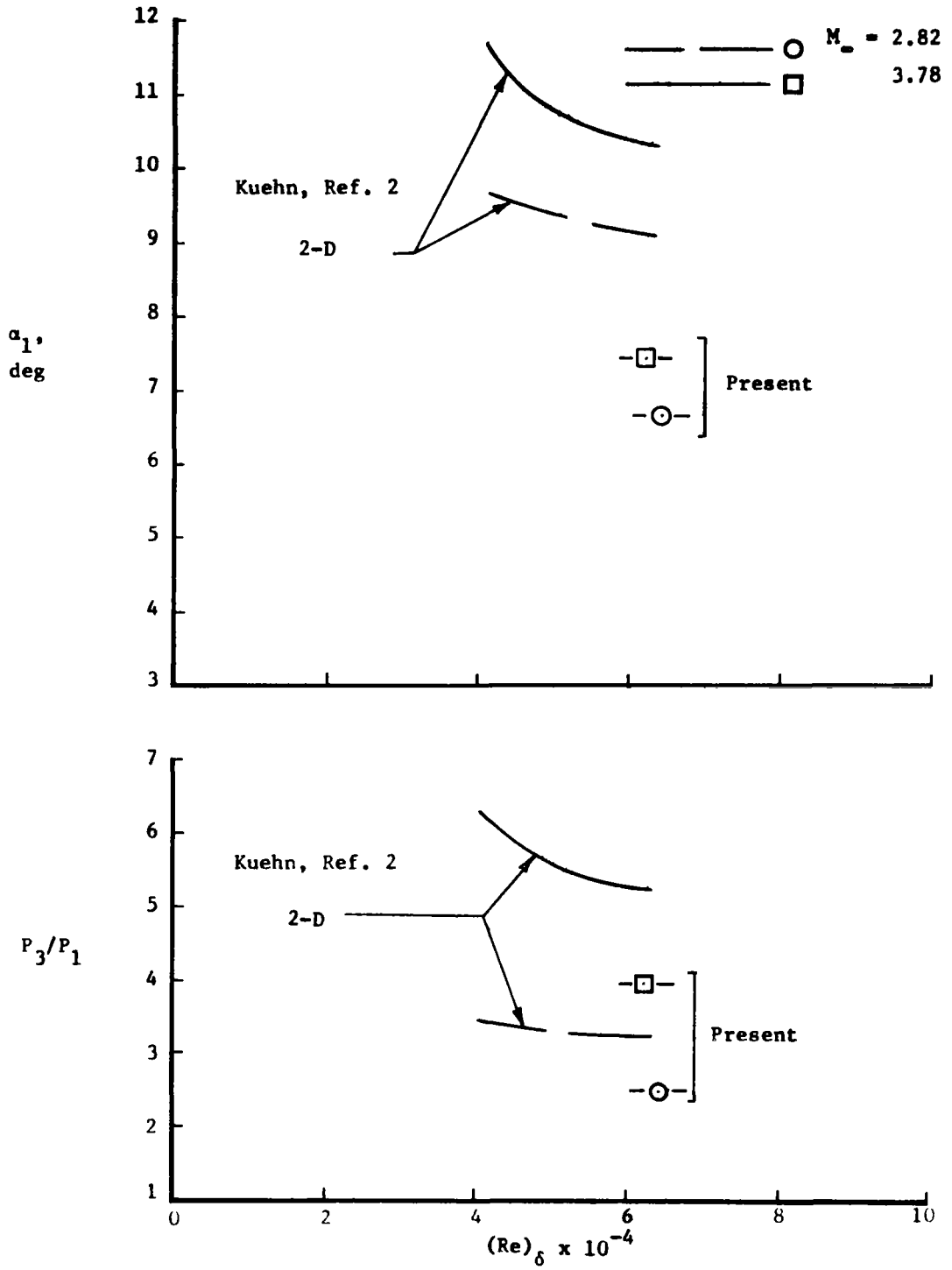

Figure 45. Conditions for Incipient Separation, Solid Wall, Two-Dimensional and Axially Symmetric Flow.

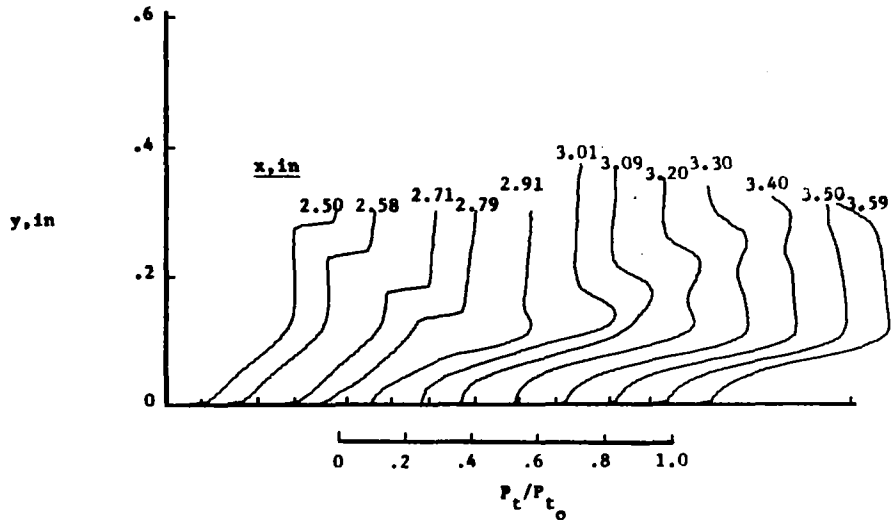

(a) Pitot Pressure Surveys.

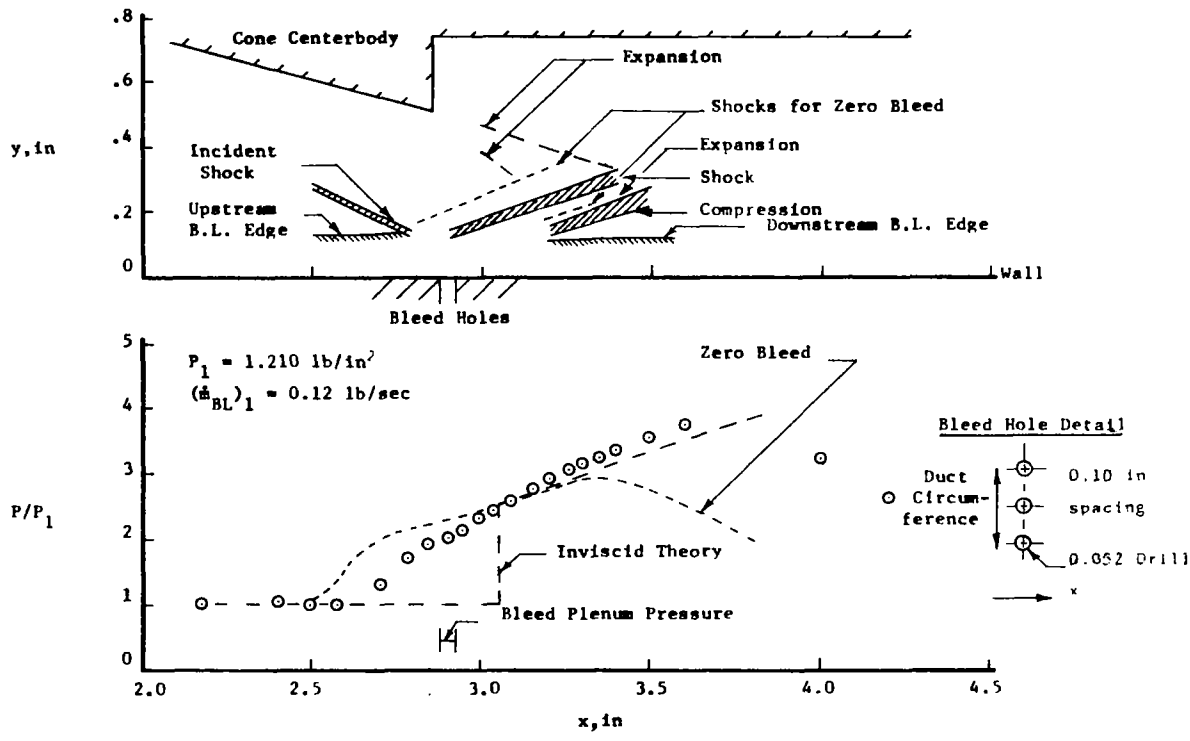

(b) Flow and Surface Static-Pressure Distribution.

Figure 46. Perforated-Wall Shock-Interaction Region Properties, 15-Degree Cone at M_∞ = 2.82, 2.8% Suction.

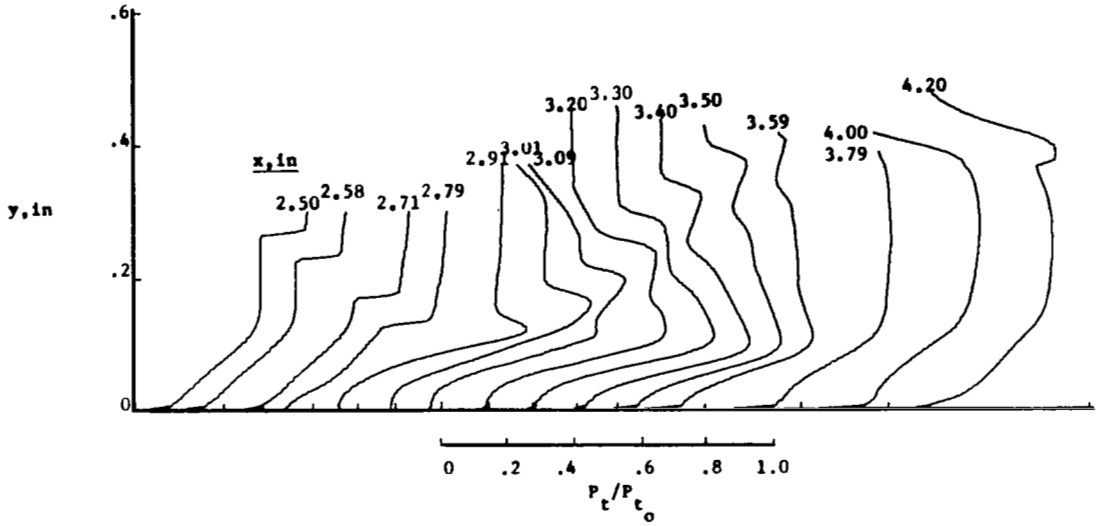

(a) Pitot Pressure Surveys.

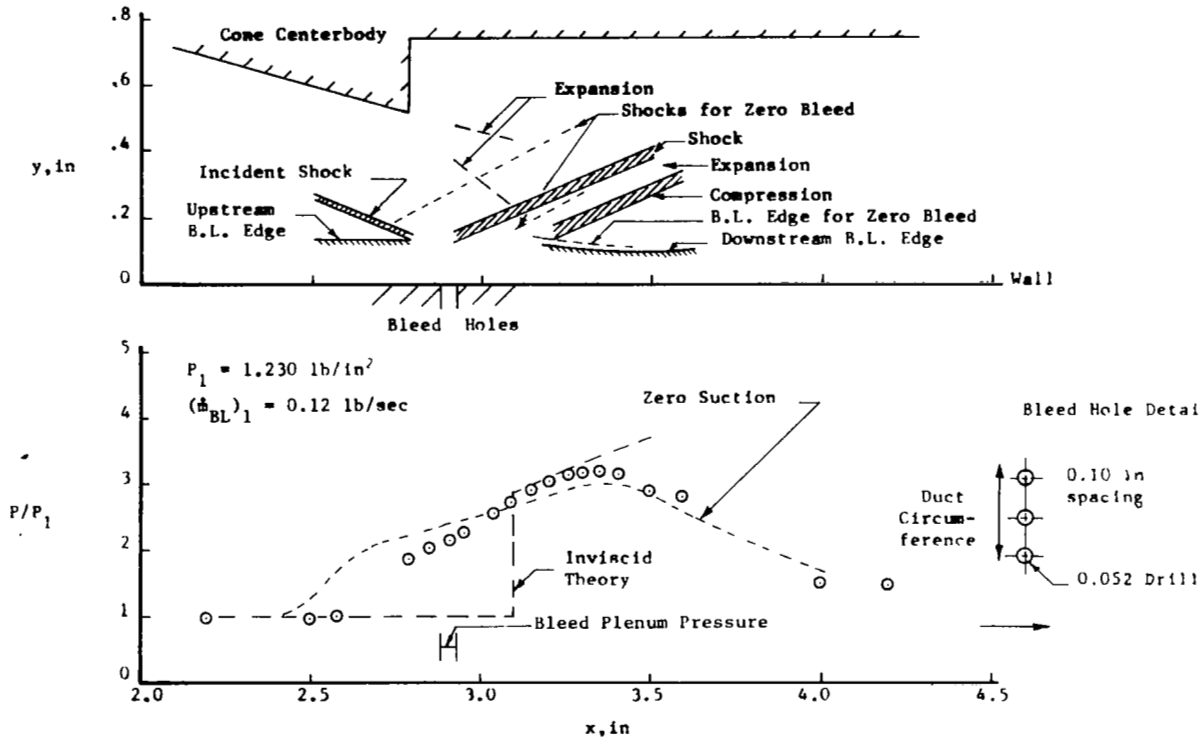

(b) Flow Field and Surface Static-Pressure Distribution.

Figure 47. Perforated Wall Shock-Interaction Region Properties, 16-Degree Cone at M_∞ = 2.82, 3.6% Suction.

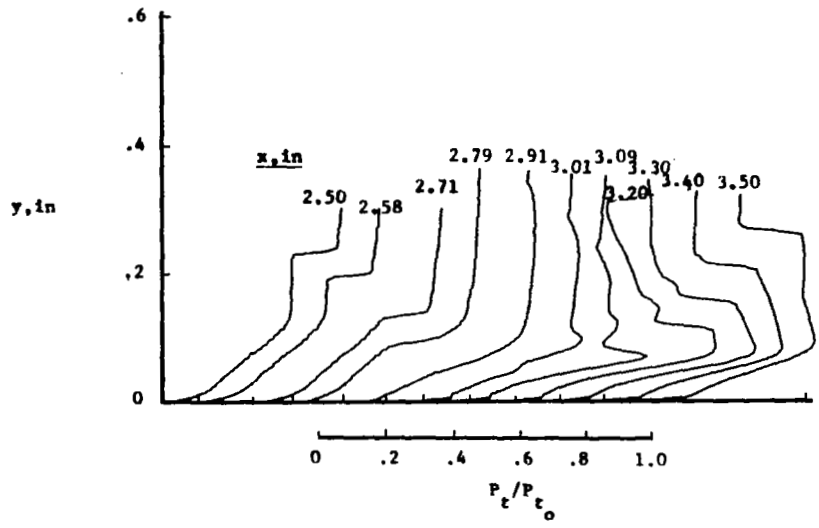

(a) Pitot Pressure Surveys.

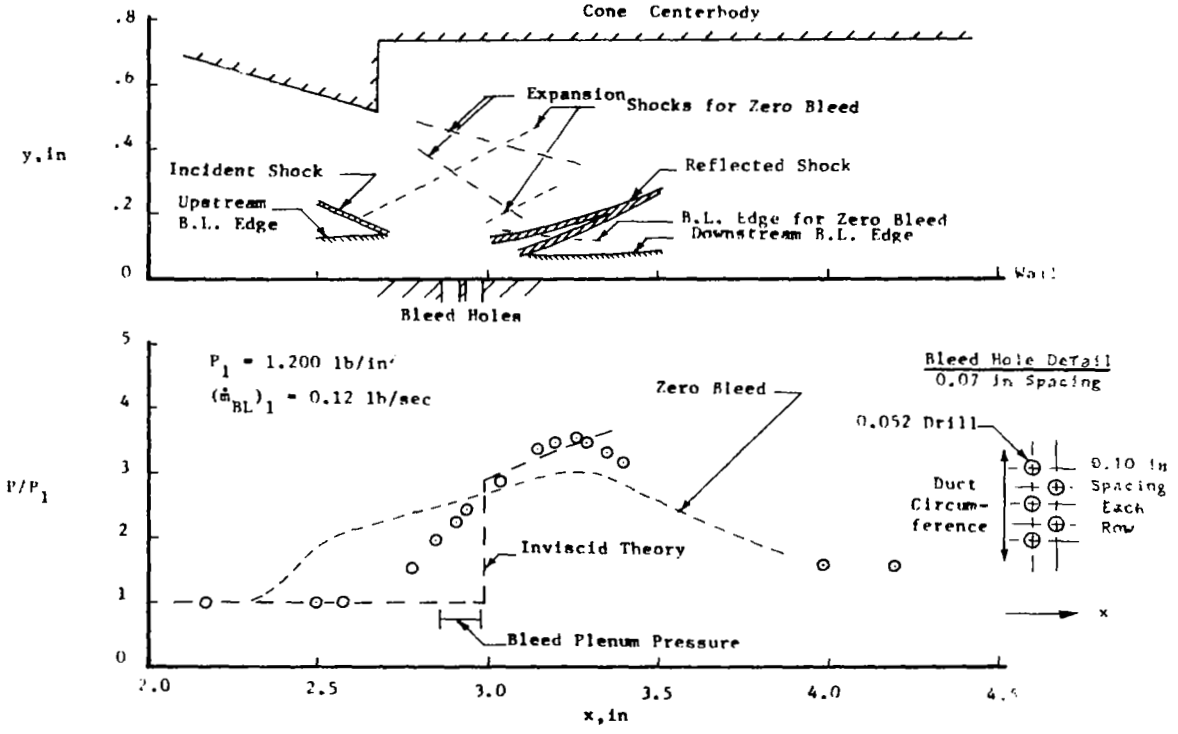

(b) Flow Field and Surface Static-Pressure Distribution.

Figure 48. Perforated-Wall Shock-Interaction Region Properties, 16-Degree Cone at M_∞ = 2.82, 6.4% Suction.

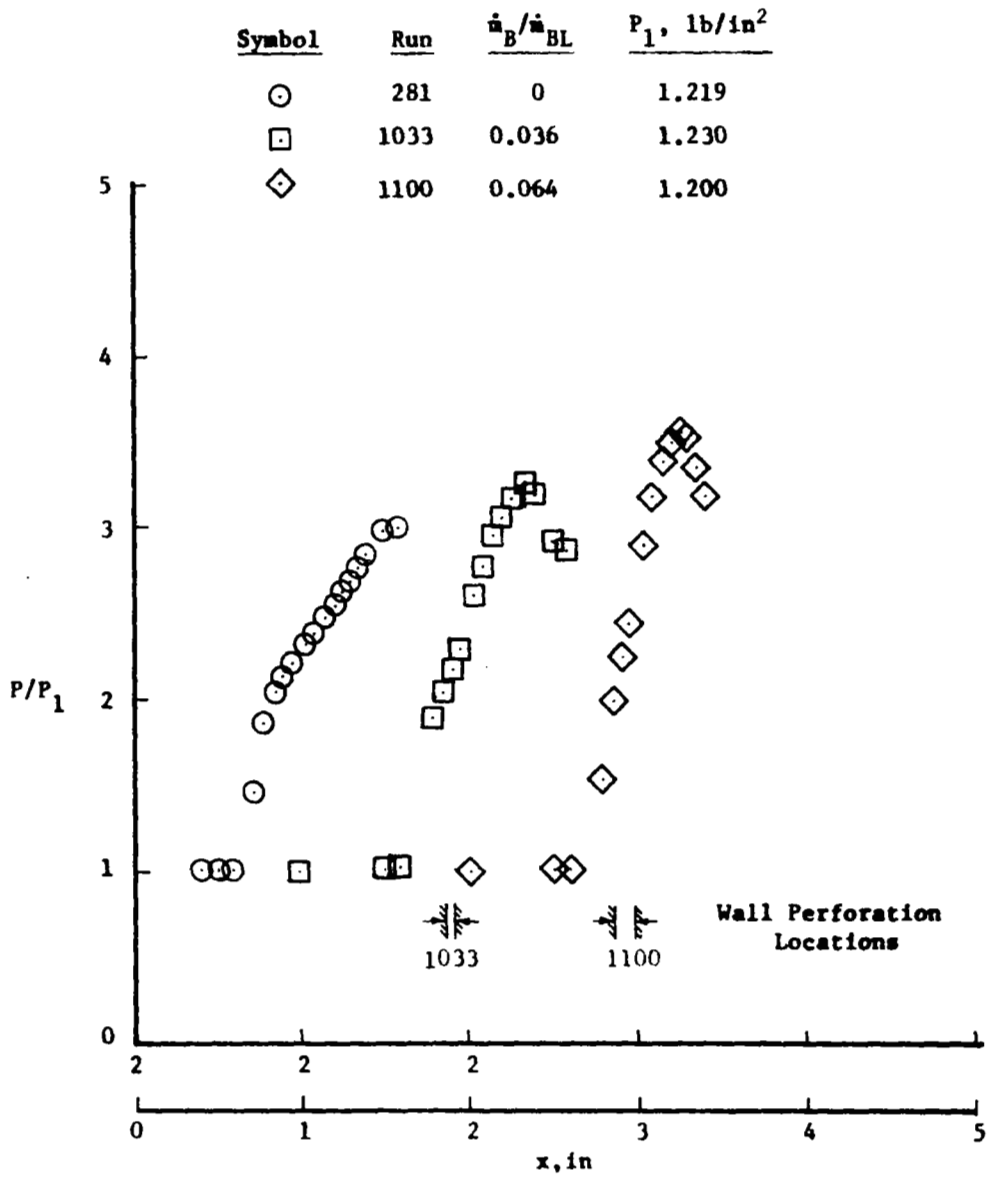

Figure 49. Effect of Suction Rate on Surface Static-Pressure Distribution, 16-Degree Cone at M_∞ = 2.82 with Suction within Interaction Region.

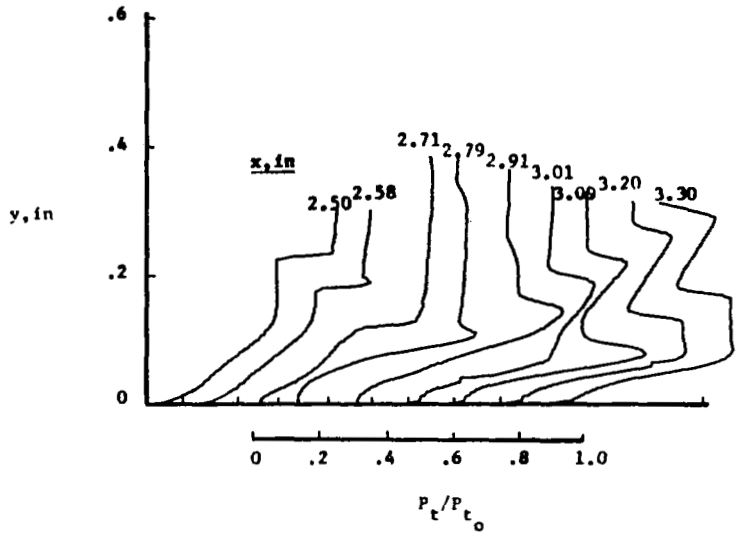

(a) Pitot Pressure Surveys.

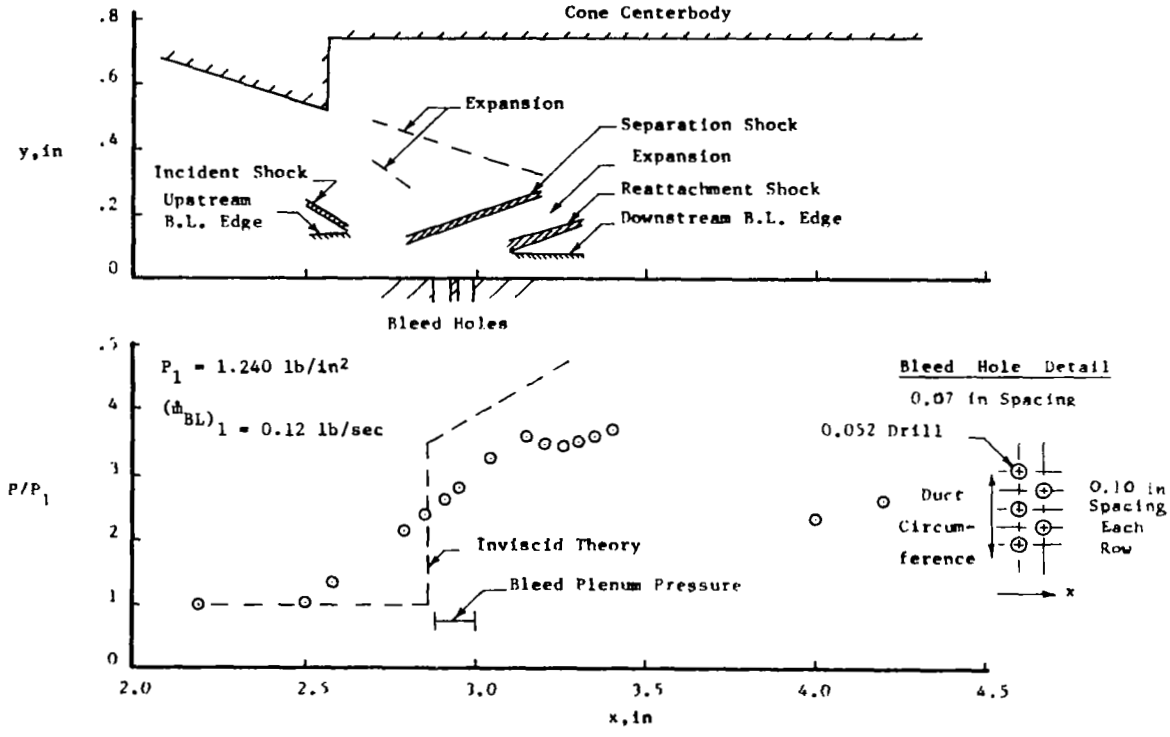

(b) Flow Field and Surface Static-Pressure Distribution.

Figure 50. Perforated-Wall Shock-Interaction Region Properties, 18-Degree Cone at M_∞ = 2.82, 9.7% Suction.

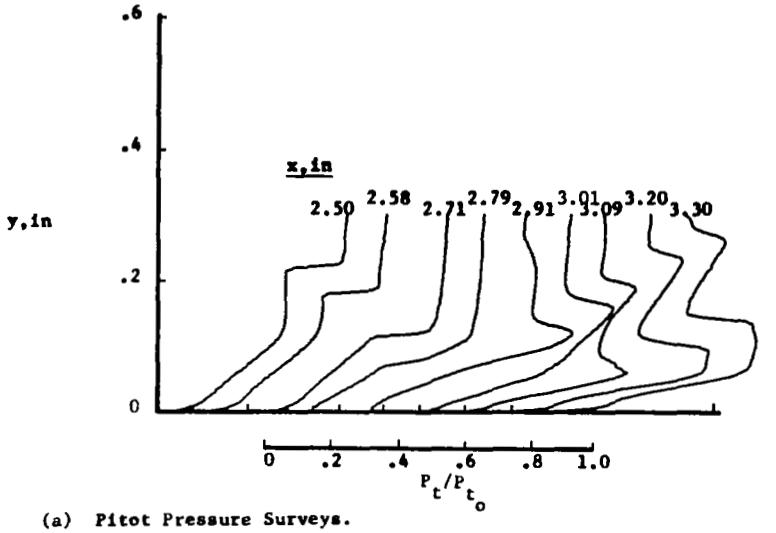

(a) Pitot Pressure Surveys.

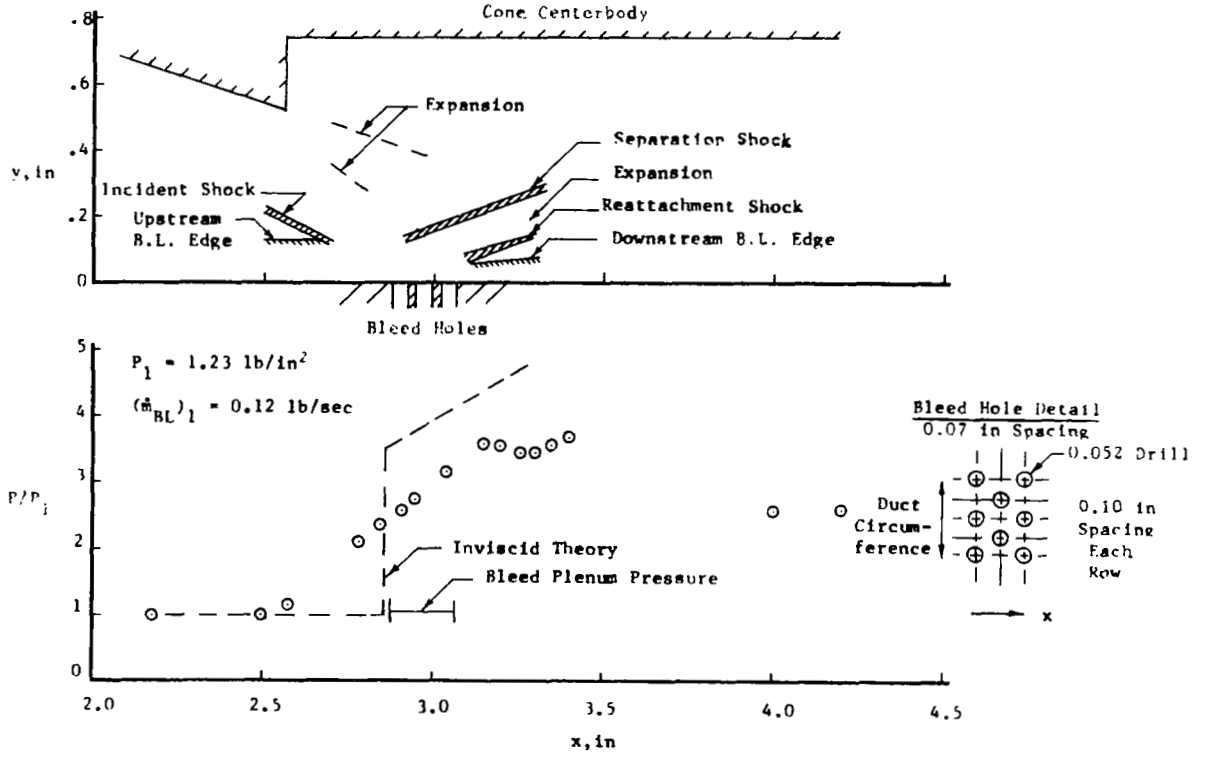

(b) Flow Field and Surface Static-Pressure Distribution.

Figure 51. Perforated-Wall Shock-Interaction Region Properties, 18-Degree Cone at M_∞ = 2.82, 13.5% Suction.

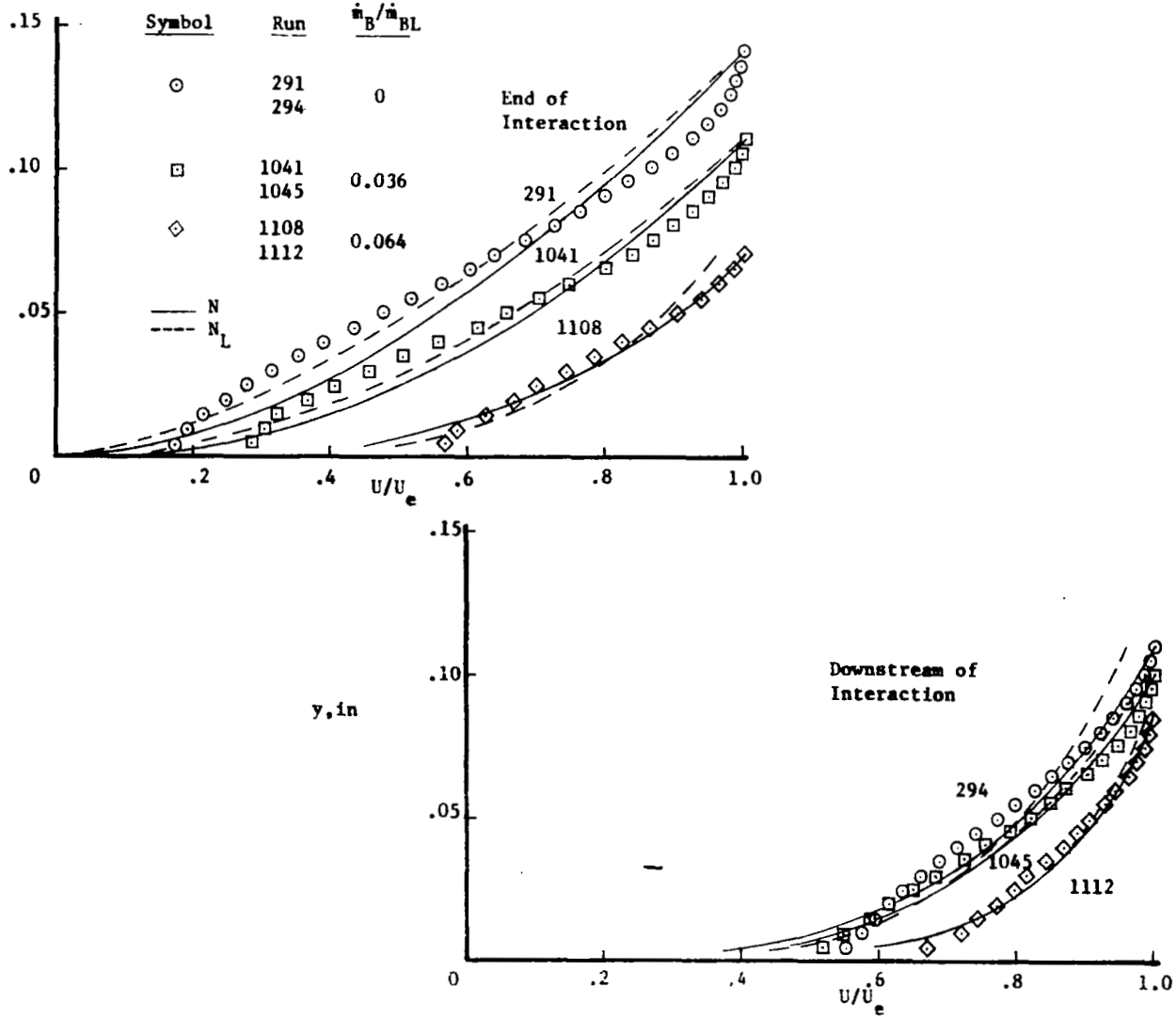

Figure 52. Typical Boundary-Layer Velocity Profiles, 16-Degree Cone with Perforated Wall, $M_\infty = 2.82$.

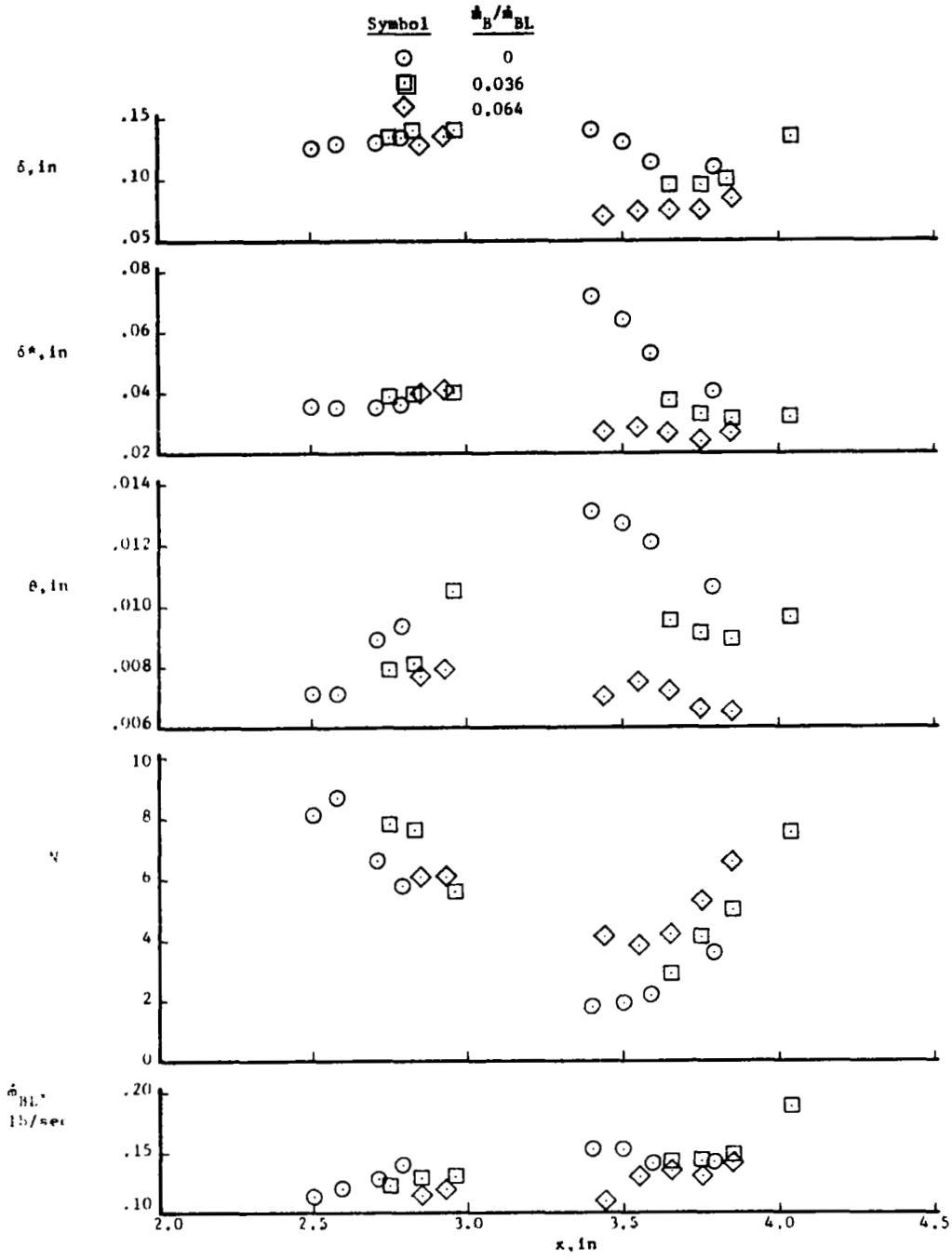

Figure 53. Summary of Boundary-Layer Properties, 16-Degree Cone with Perforated Wall, M_∞ = 2.82.

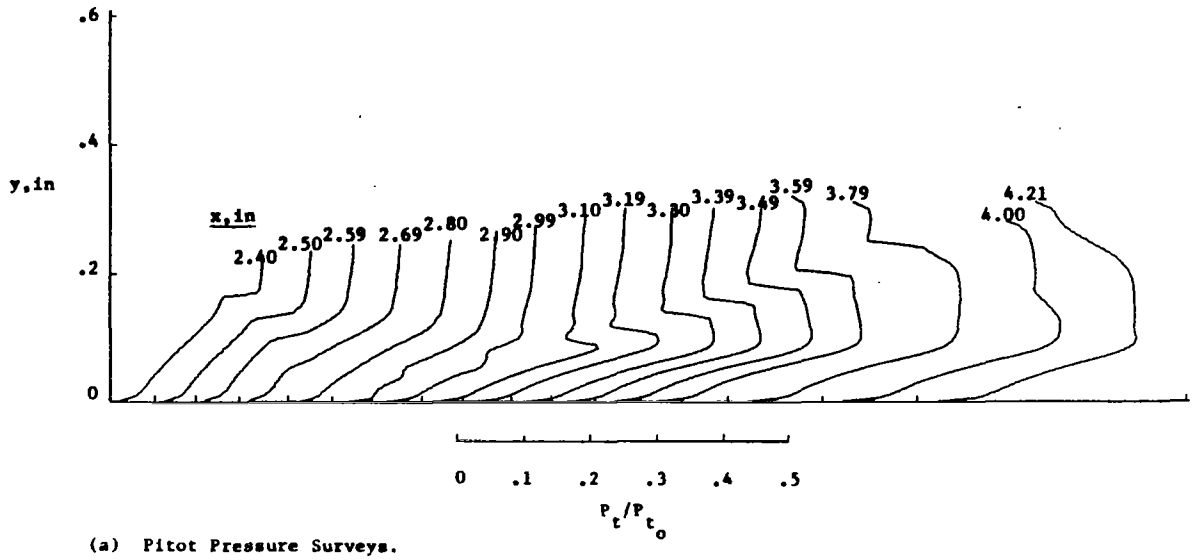

(a) Pitot Pressure Surveys.

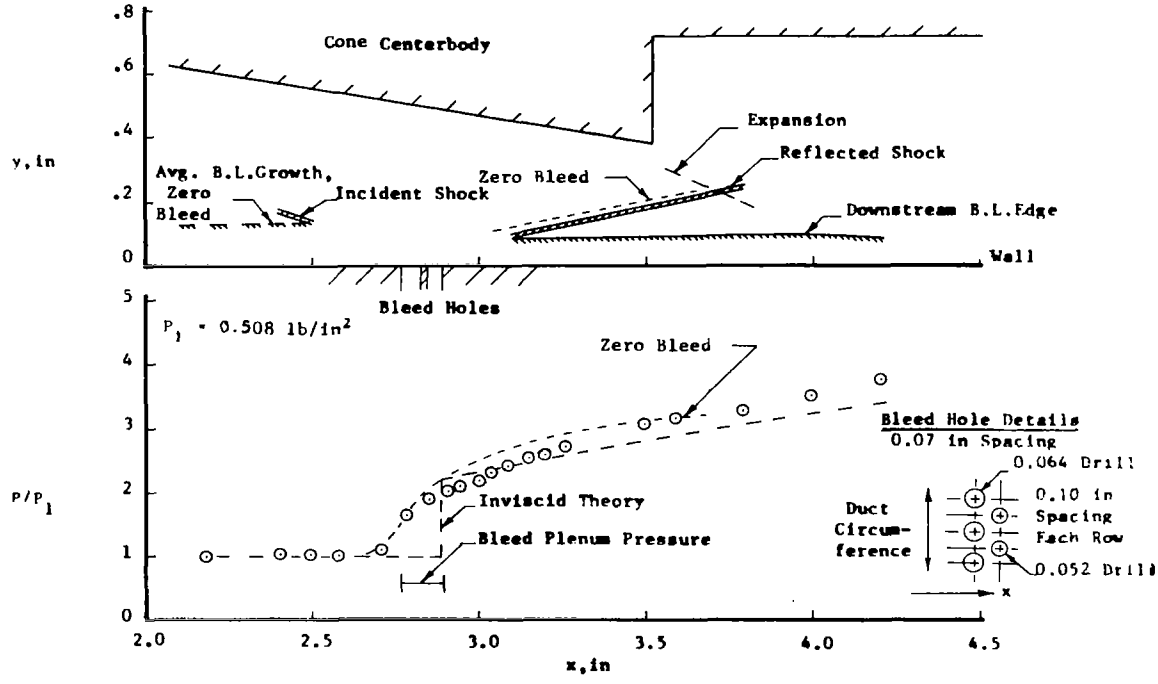

(b) Flow Field and Surface Static-Pressure Distribution.

Figure 54. Perforated-Wall Shock-Interaction Region Properties, 10-Degree Cone at M_∞ = 3.78, 3.6% Suction.

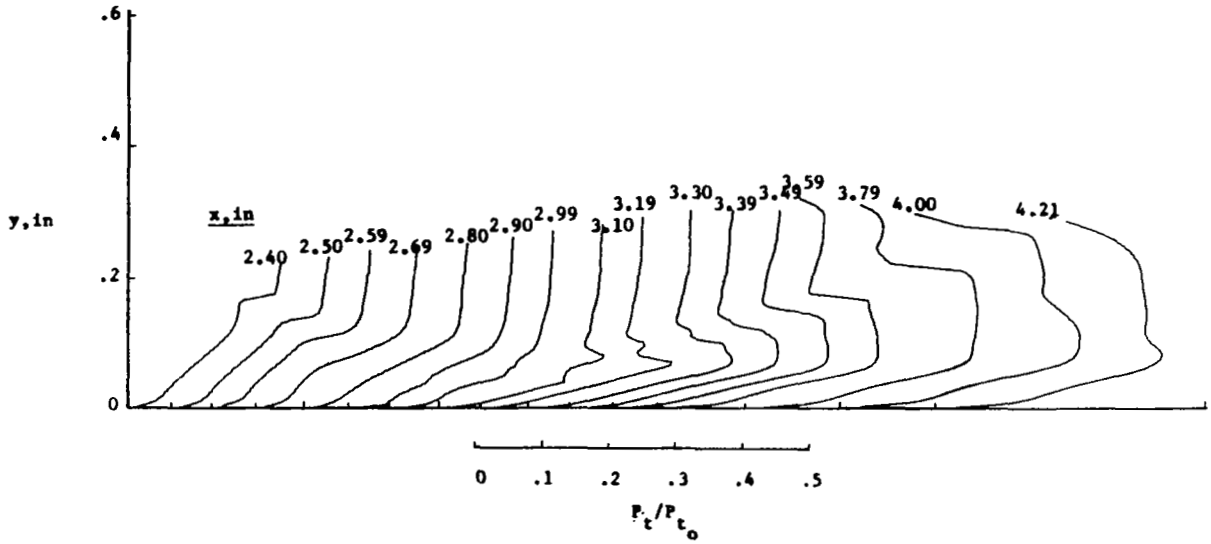

(a) Pitot Pressure Surveys.

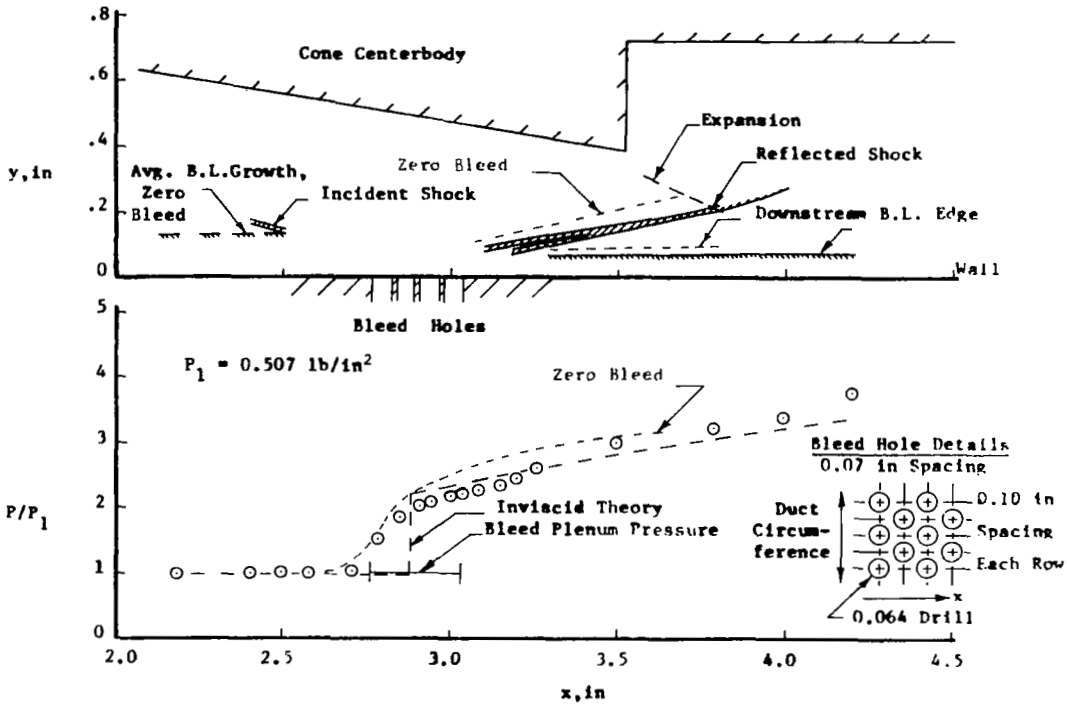

(b) Flow Field and Surface Static-Pressure Distribution.

Figure 55. Perforated-Wall Shock-Interaction Region Properties, 10-Degree Cone at M_∞ = 3.78, 8.5% Suction.

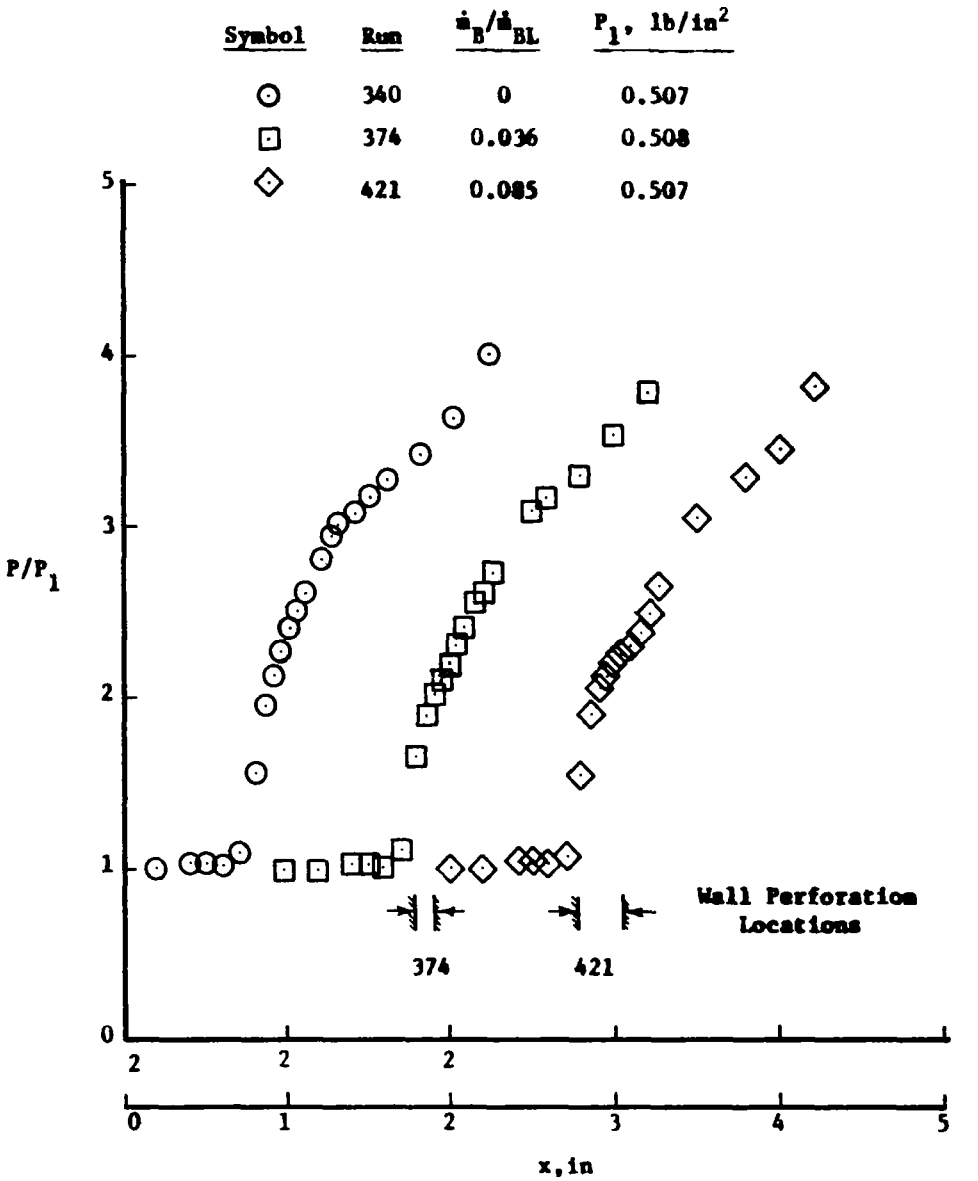

Figure 56. Effect of Suction Rate on Surface Static-Pressure Distribution, 10-Degree Cone at M_∞ = 3.78 with Suction within Interaction Region.

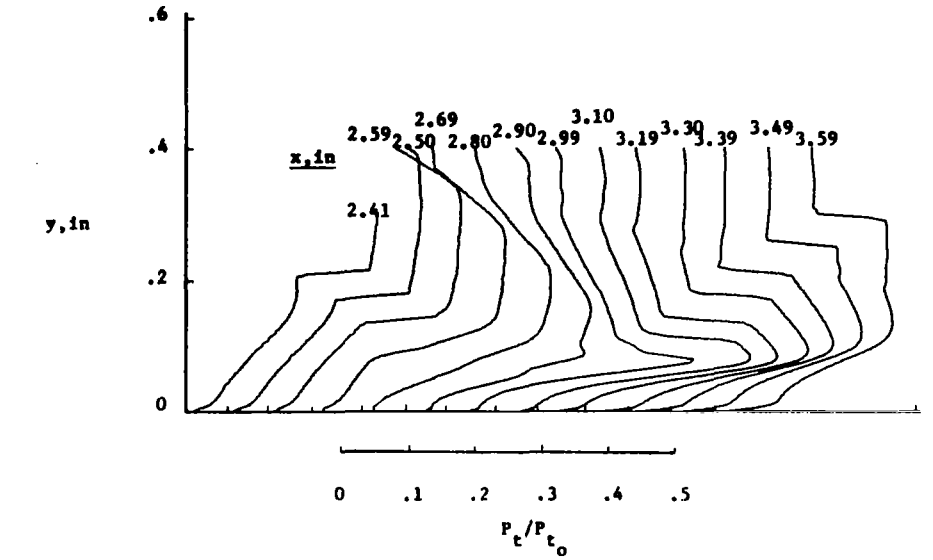

(a) Pitot Pressure Surveys.

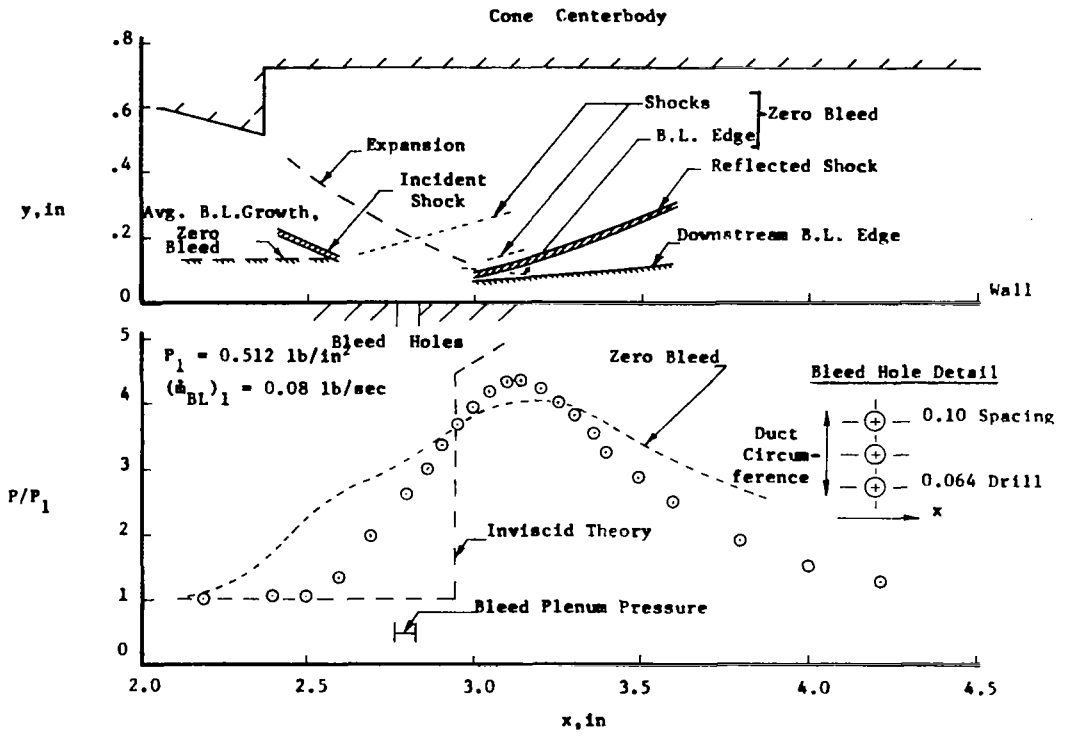

(b) Flow Field and Surface Static-Pressure Distribution.

Figure 57. Perforated-Wall Shock-Interaction Region Properties, 15-Degree Cone at M_∞ = 3.78, 3.1% Suction.

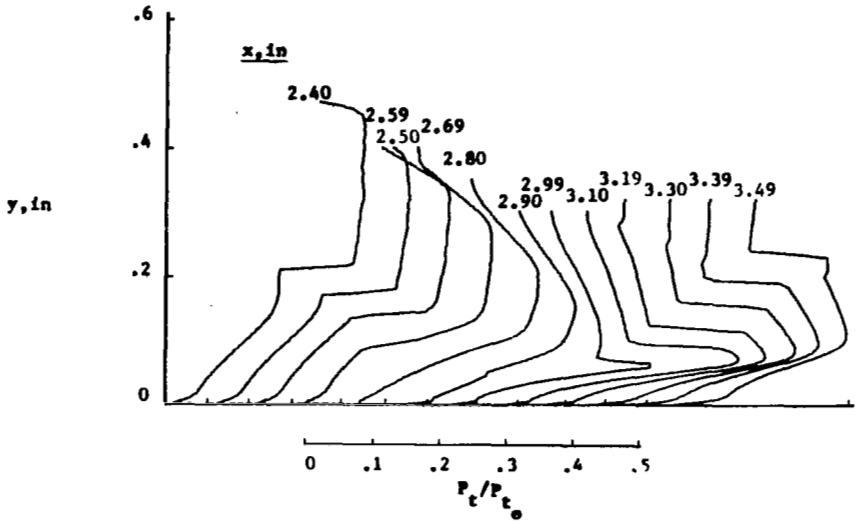

(a) Pitot Pressure Surveys.

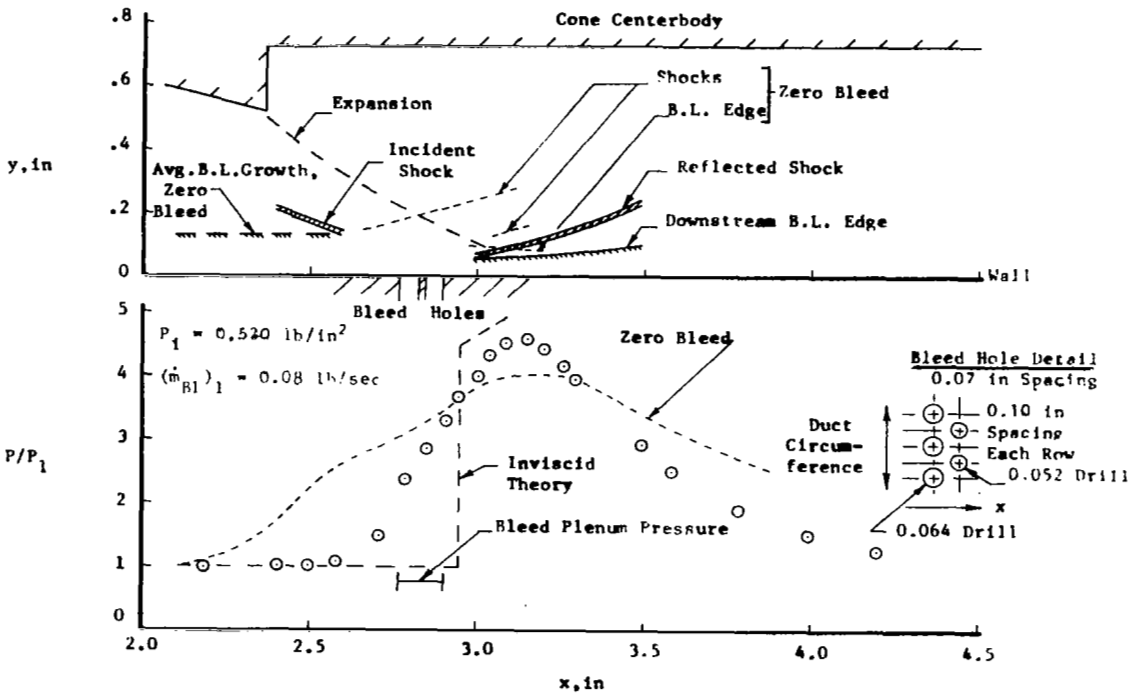

(b) Flow Field and Surface Static-Pressure Distribution.

Figure 58. Perforated-Wall Shock-Interaction Region Properties, 15-Degree Cone at M_∞ = 3.78, 5.2% Suction.

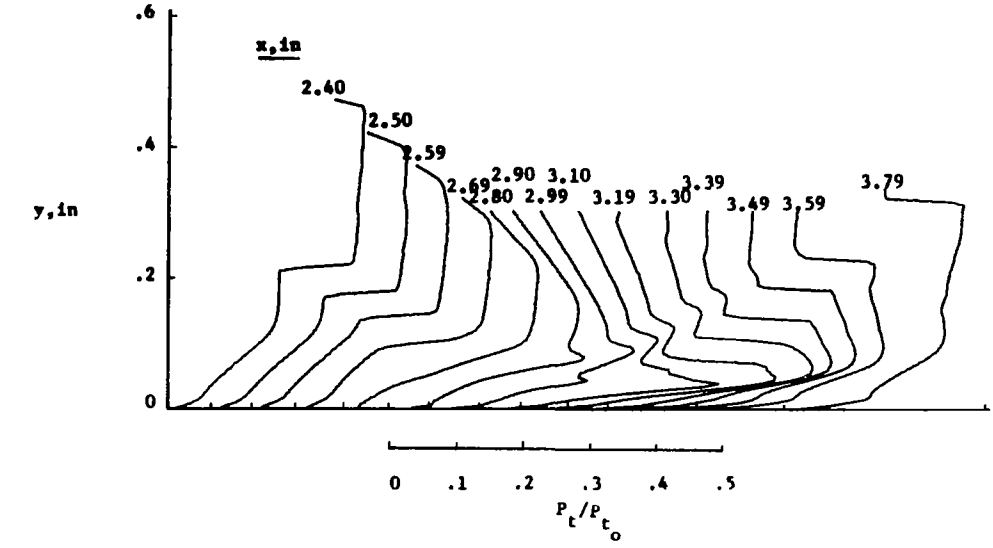

(a) Pitot Pressure Surveys.

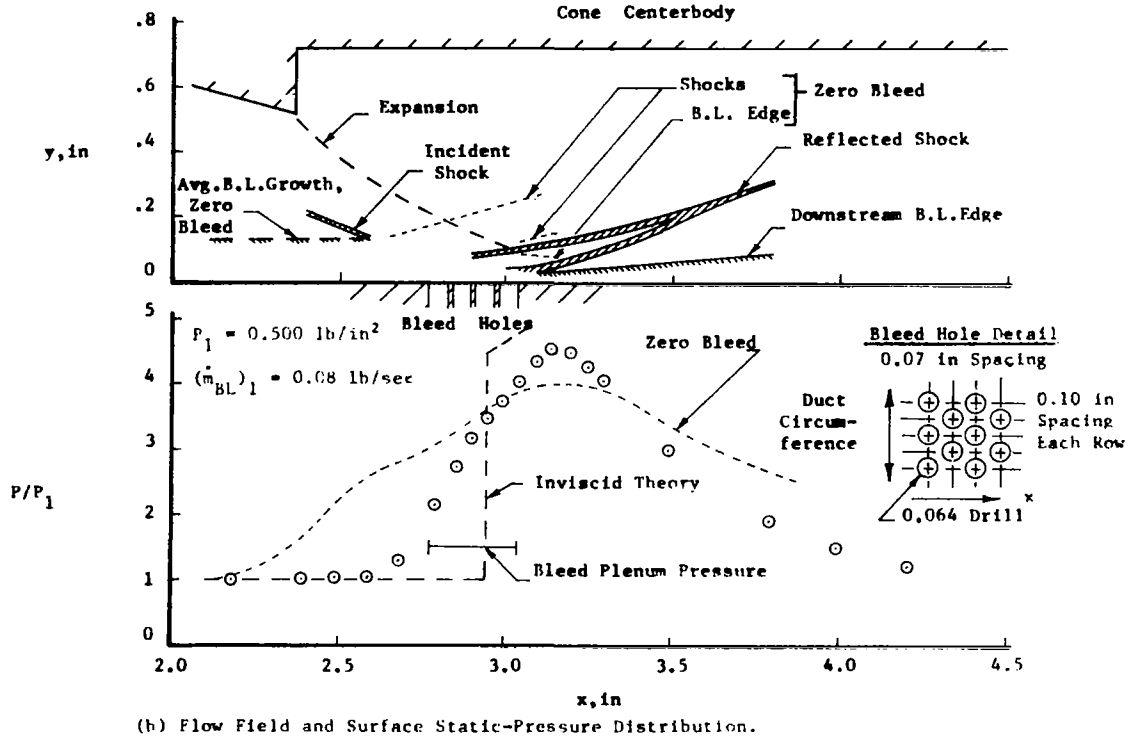

(b) Flow Field and Surface Static-Pressure Distribution.

Figure 59. Perforated-Wall Shock-Interaction Region Properties, 15-Degree Cone at M_∞ = 3.78, 13.1% Suction.

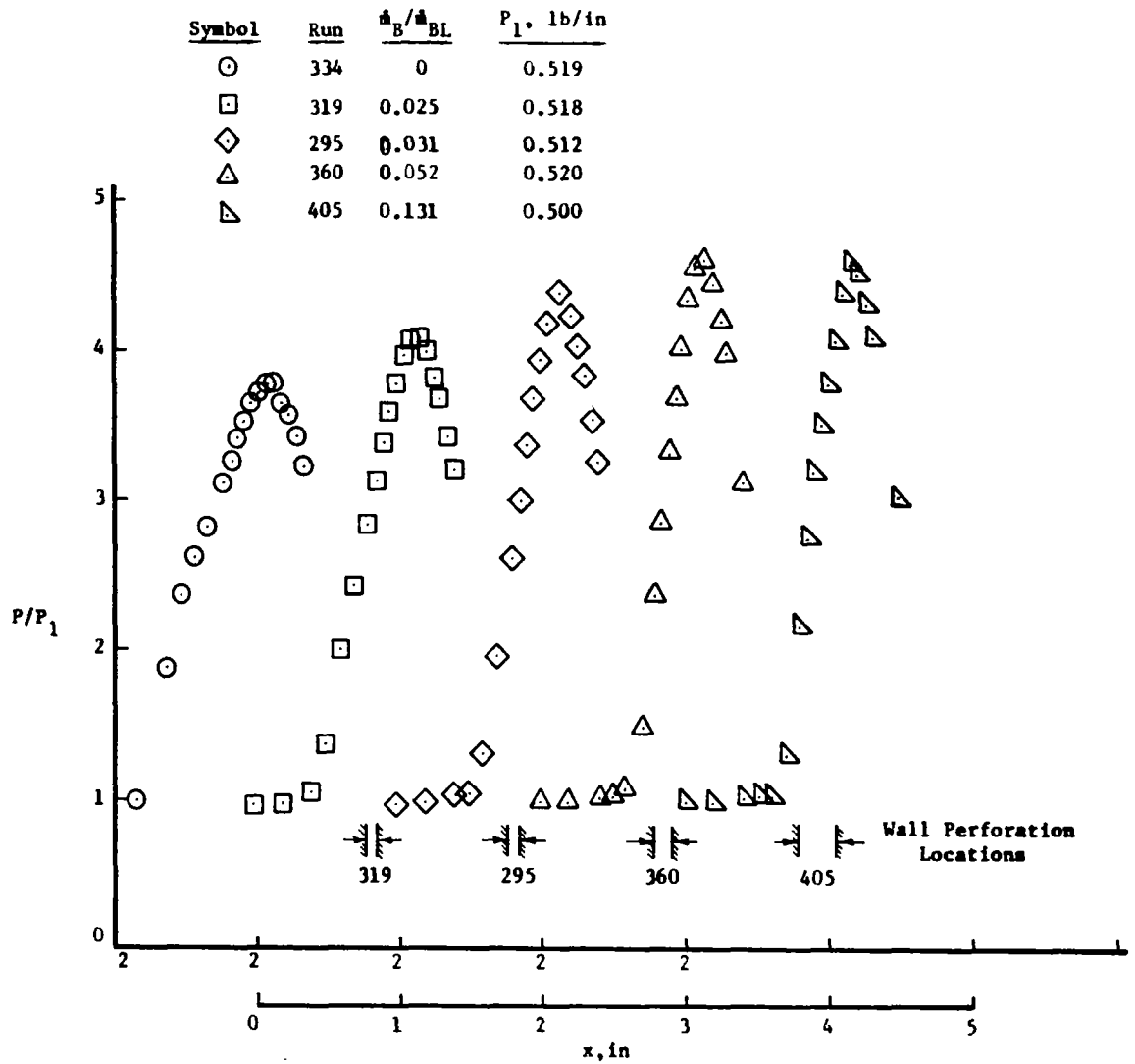

Figure 60. Effect of Suction Rate on Surface Static-Pressure Distribution, 15-Degree Cone at M_∞ = 3.78 with Suction within Interaction Region.

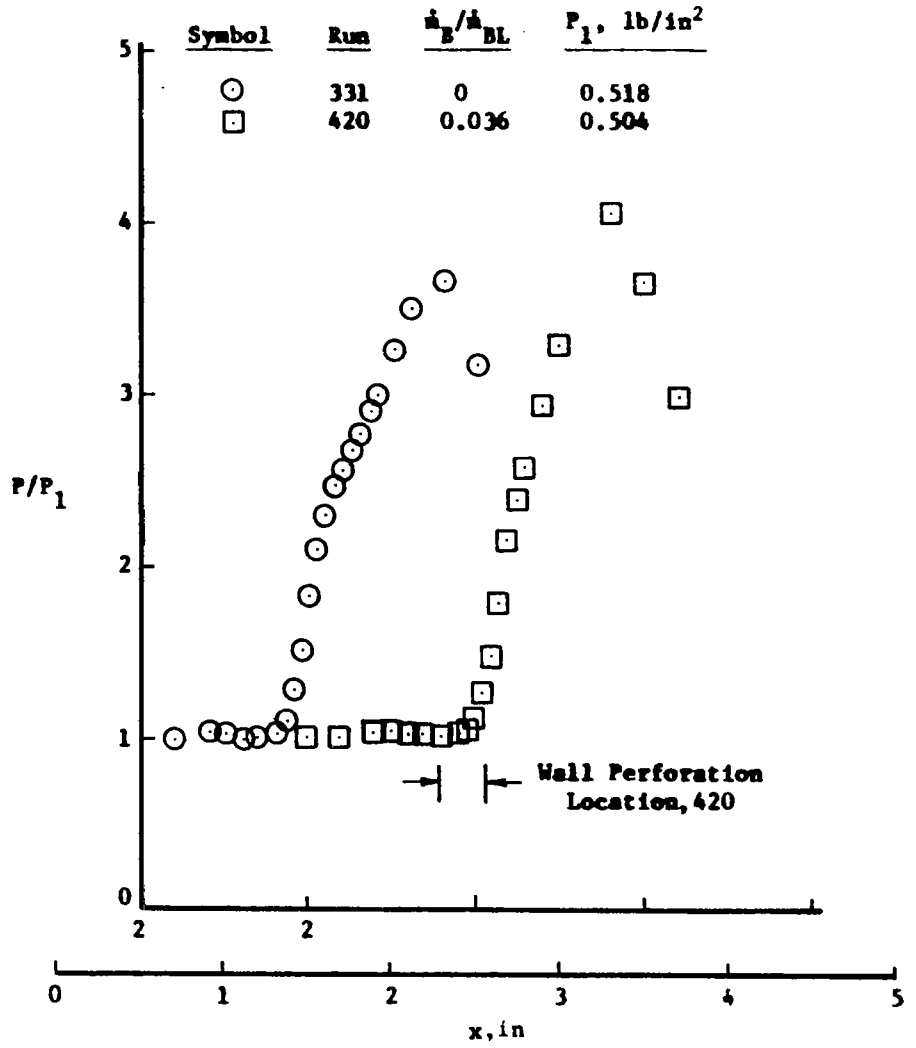

Figure 61. Effect of Suction Rate on Surface Static-Pressure Distribution, 15-Degree Cone at M_∞ = 3.78 with Suction Upstream of Interaction Region.

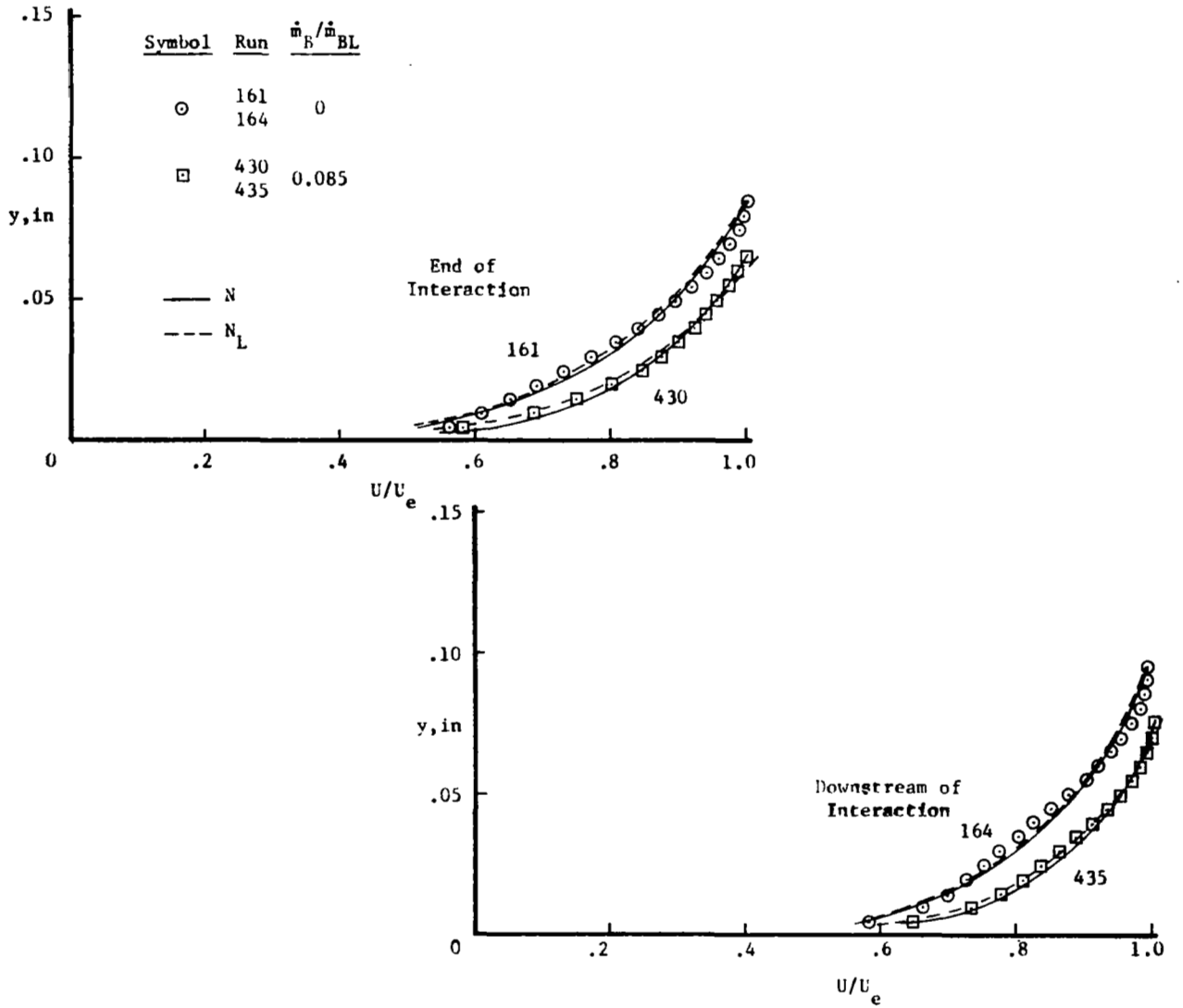

Figure 62. Typical Boundary-Layer Velocity Profiles, 10-Degree Cone with Perforated Wall, M_∞ = 3.78.

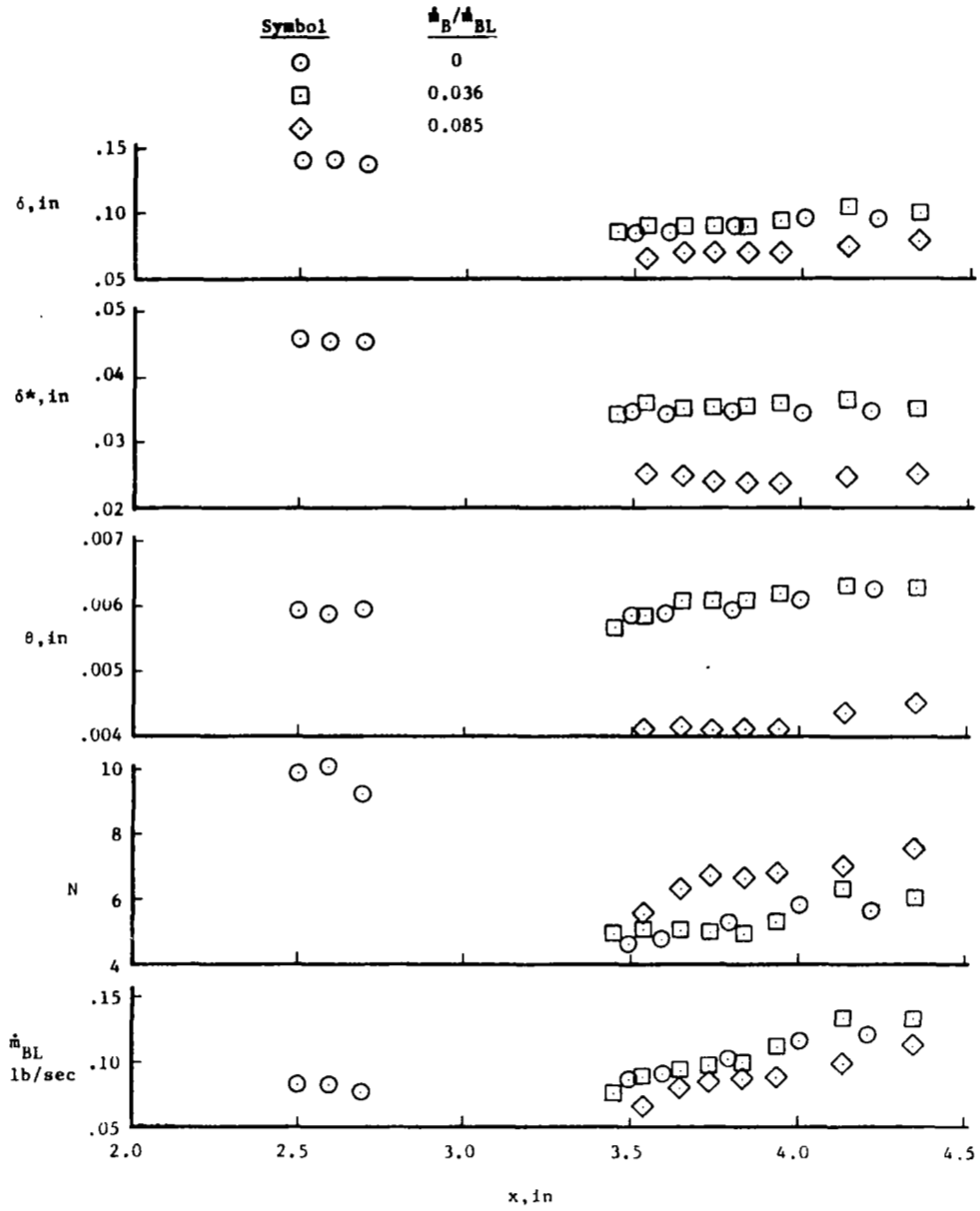

Figure 63. Summary of Boundary-Layer Properties, 10-Degree Cone with Perforated Wall, M_∞ = 3.78.

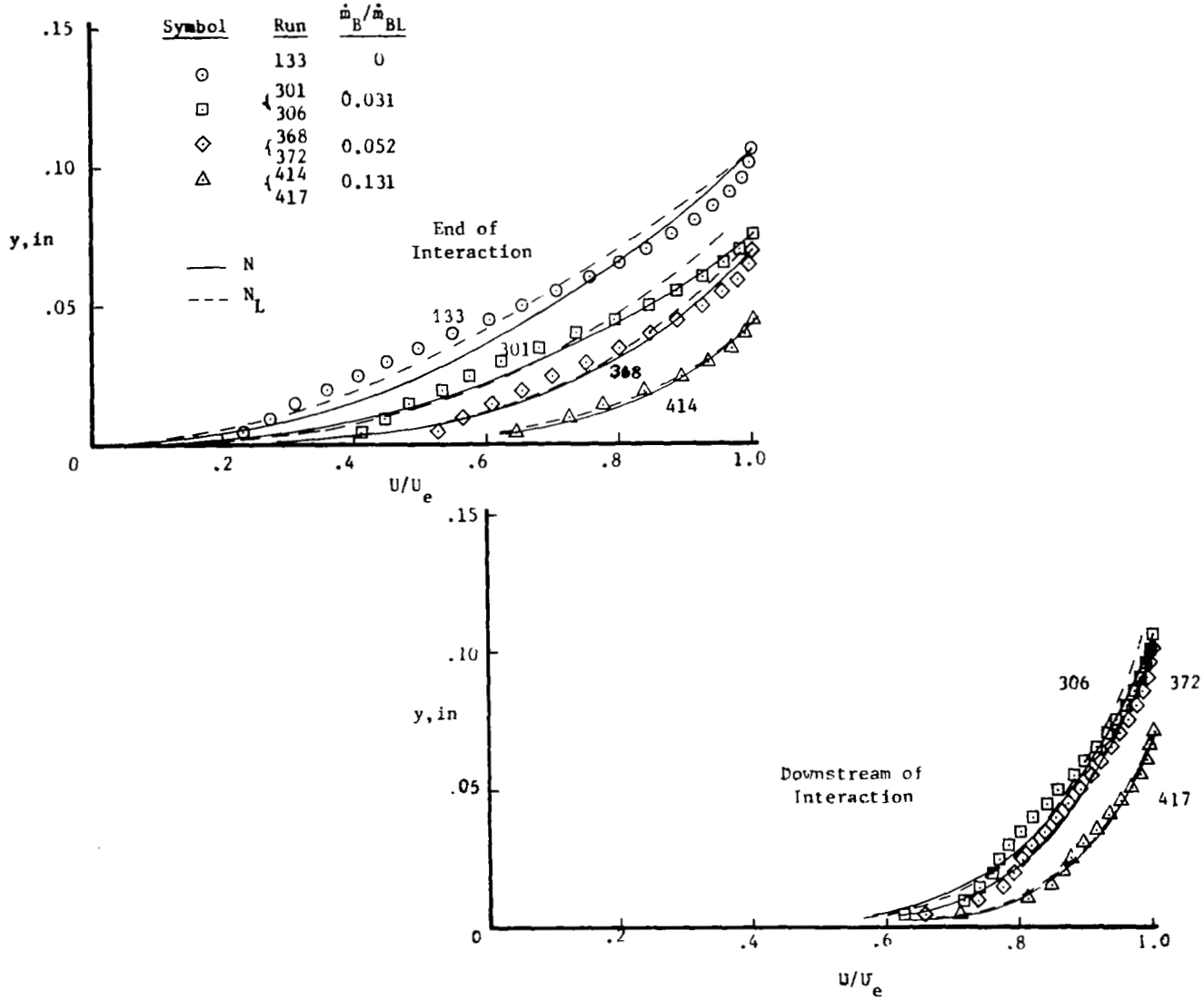

Figure 64. Typical Boundary-Layer Velocity Profiles, 15-Degree Cone with Perforated Wall, M_∞ = 3.78.

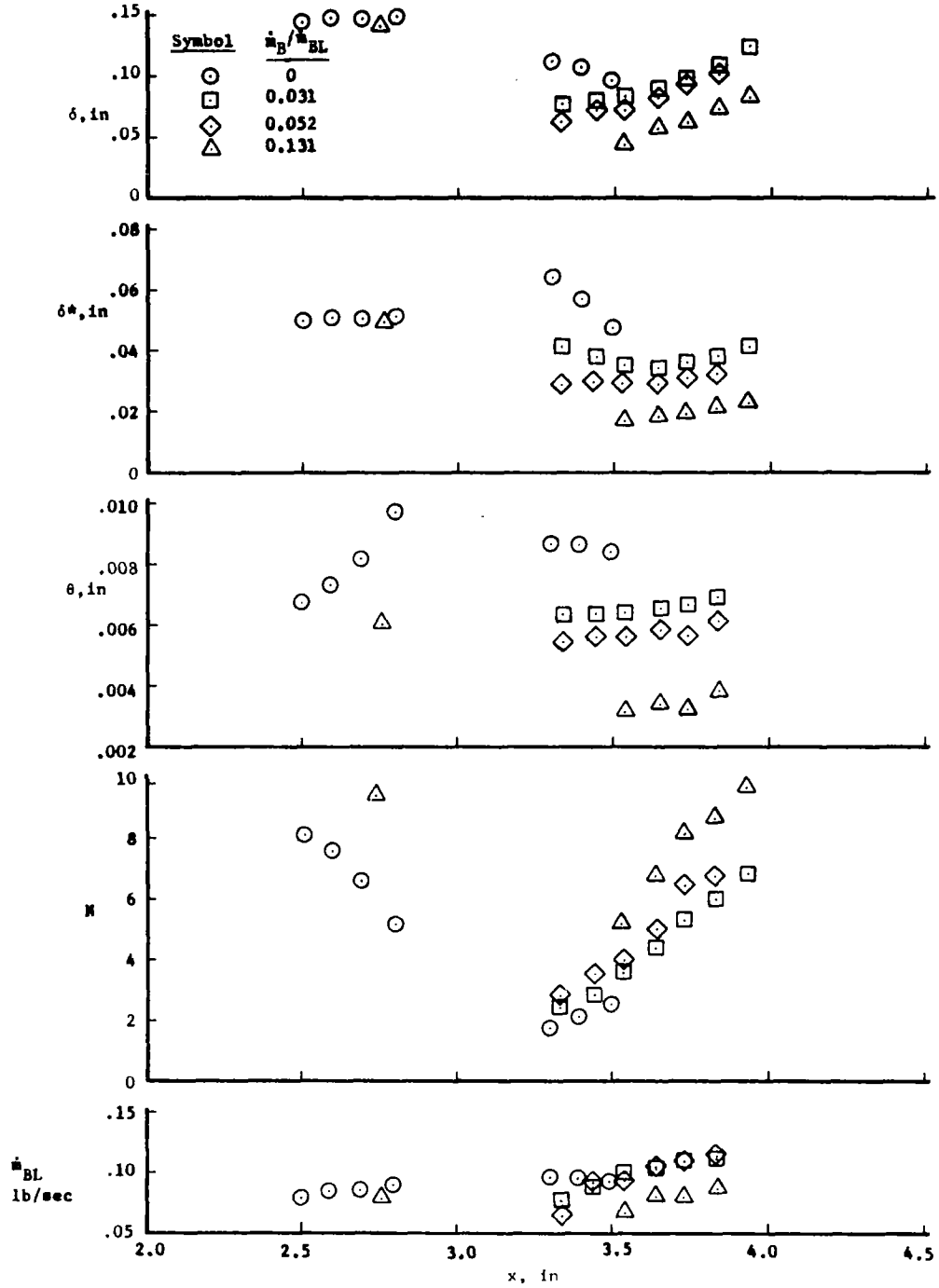

Figure 65. Summary of Boundary-Layer Properties, 15-Degree Cone with Perforated Wall, M_∞ = 3.78.

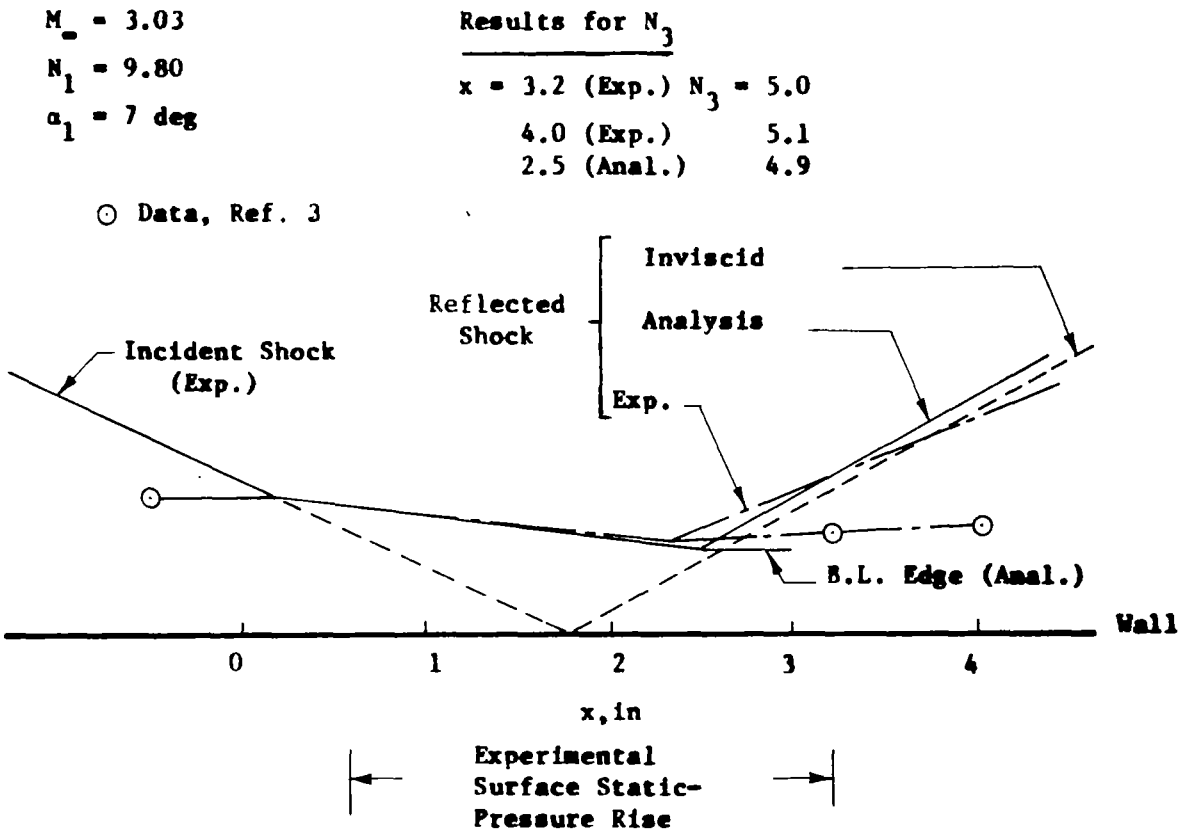

Figure 66. Predicted and Measured Results for Shock Interaction with Solid Wall, 6-Degree Wedge at M_∞ = 3.03.

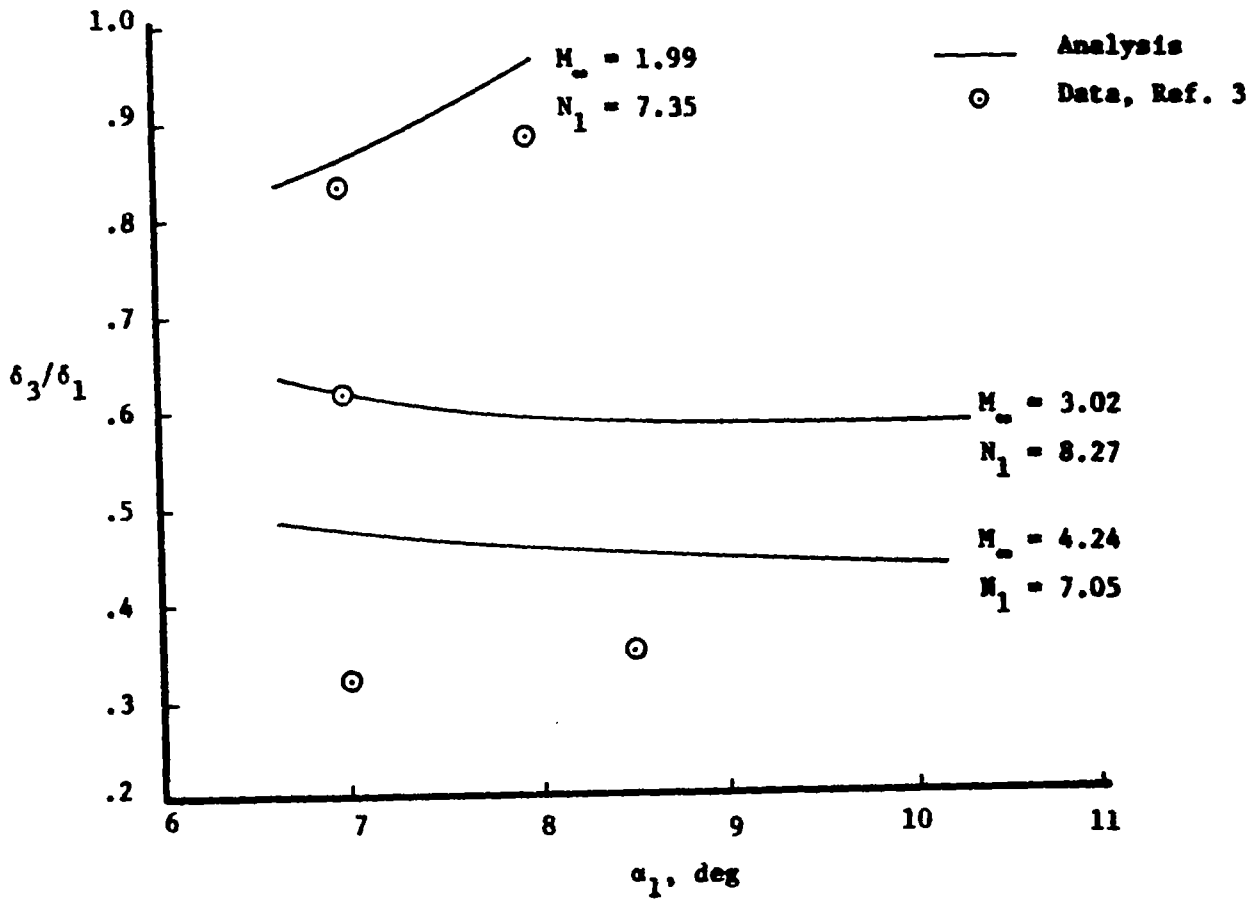

Figure 67. Comparison of Analysis and Data of Pinckney for Two-Dimensional Interactions with Solid Wall.

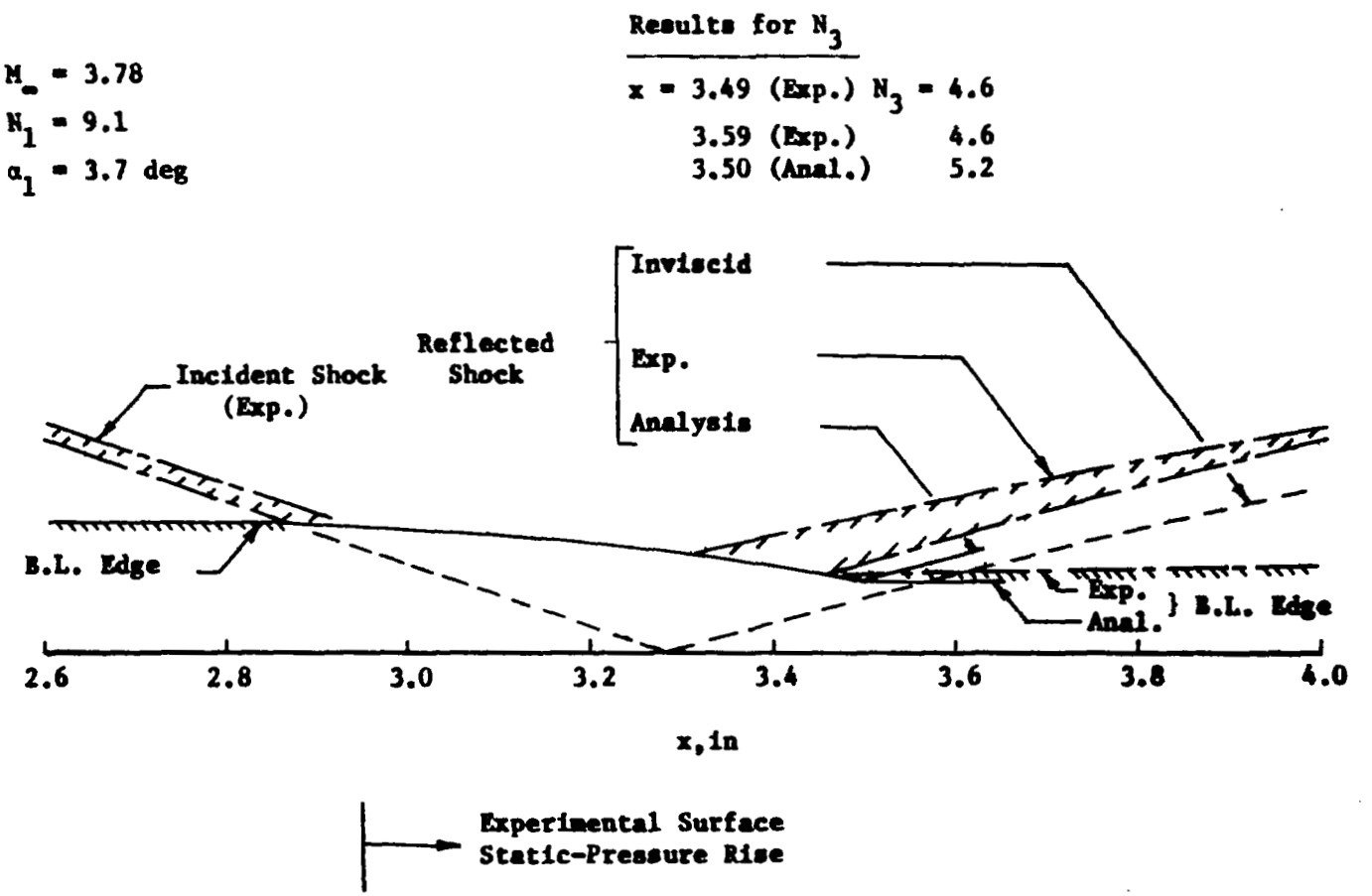

Figure 68. Predicted and Measured Results for Shock Interaction with Solid Wall, 10-Degree Cone at M_∞ = 3.78.

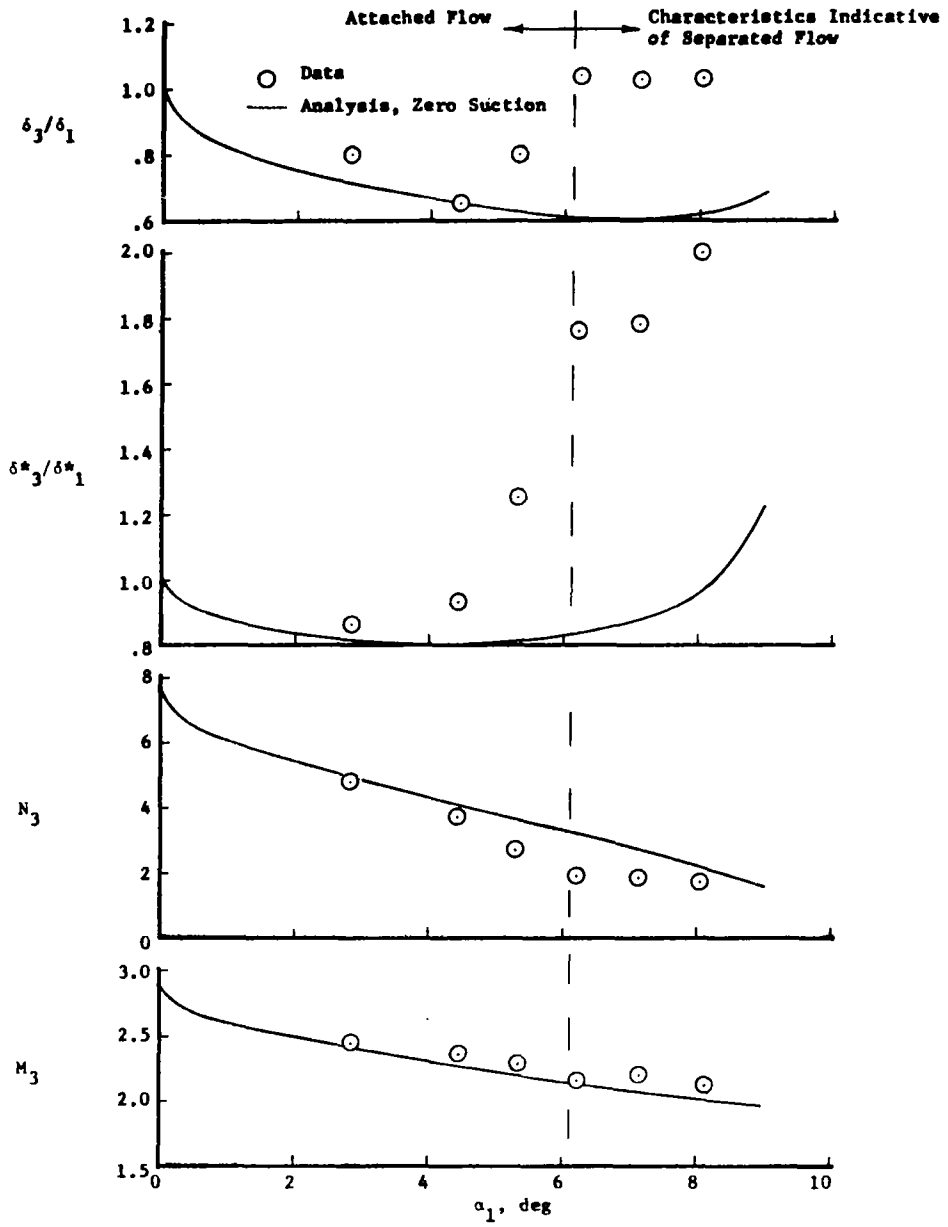

Figure 69. Comparison of Analysis and Data for Axially Symmetric Interactions with Solid Wall, $M_\infty = 2.82$.

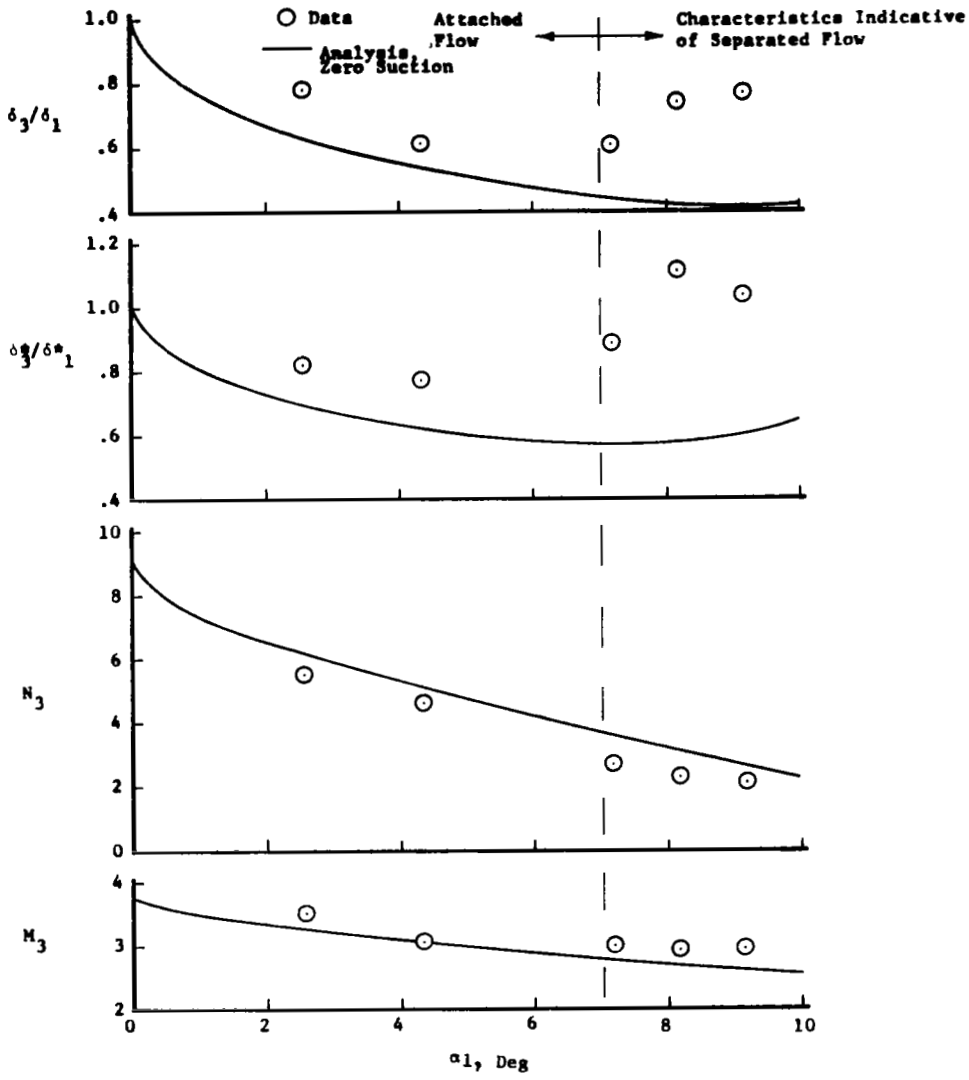

Figure 70. Comparison of Analysis and Data for Axially Symmetric Interactions with Solid Walls, $M_\infty = 3.78$.

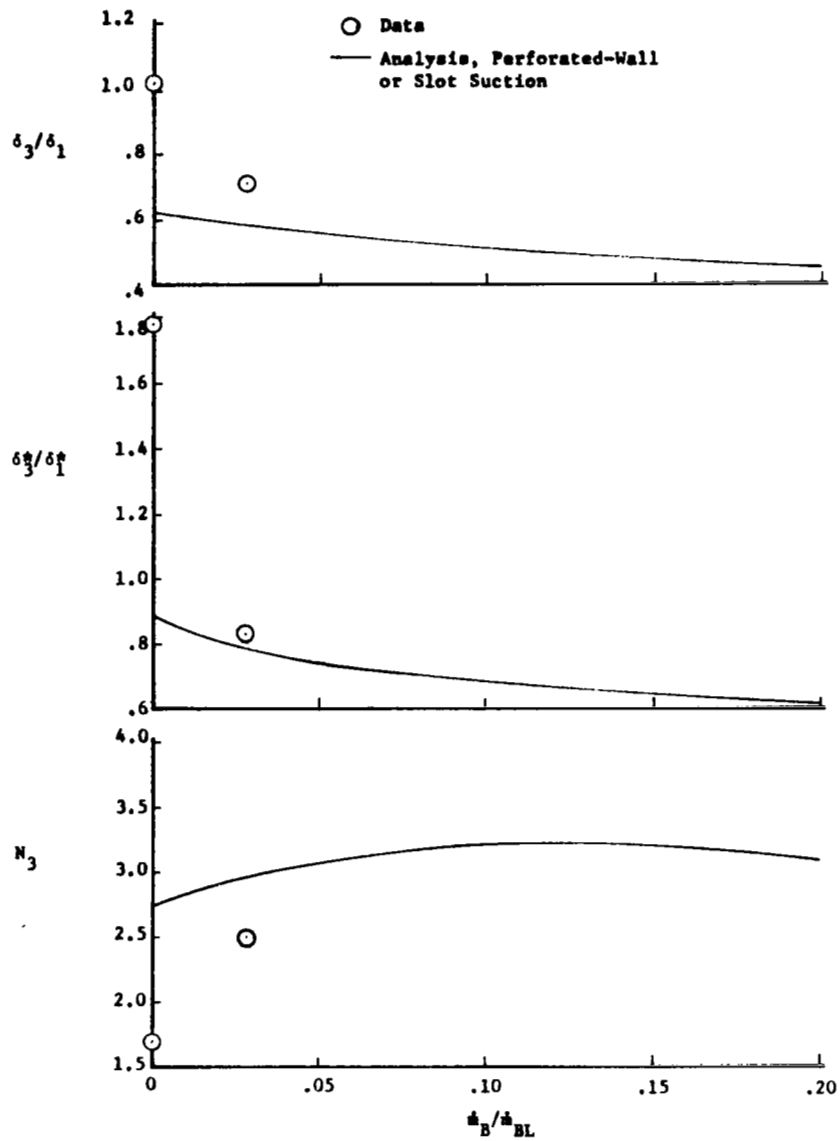

Figure 71. Comparison of Analysis and Data for Axially Symmetric Interactions with Suction, 15-Degree Cone at $M_\infty = 2.82$.

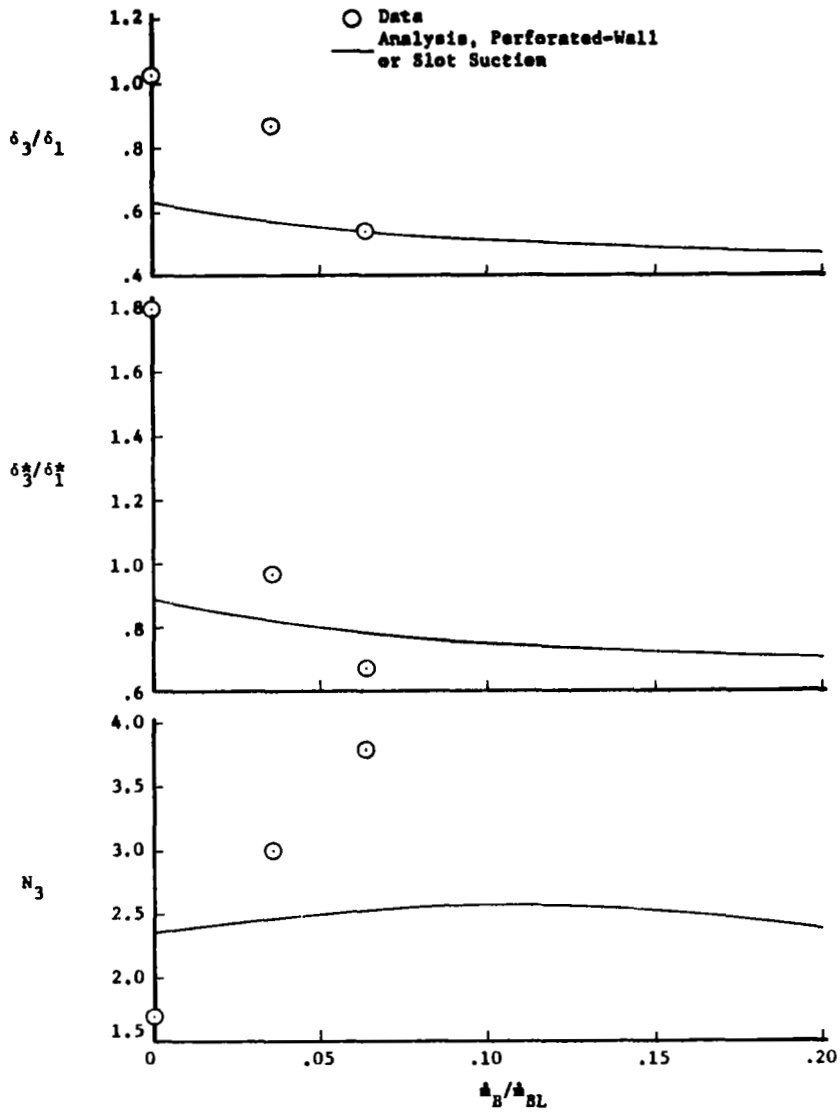

Figure 72. Comparison of Analysis and Data for Axially Symmetric Interactions with Suction, 16-Degree Cone at $M_\infty = 2.82$.

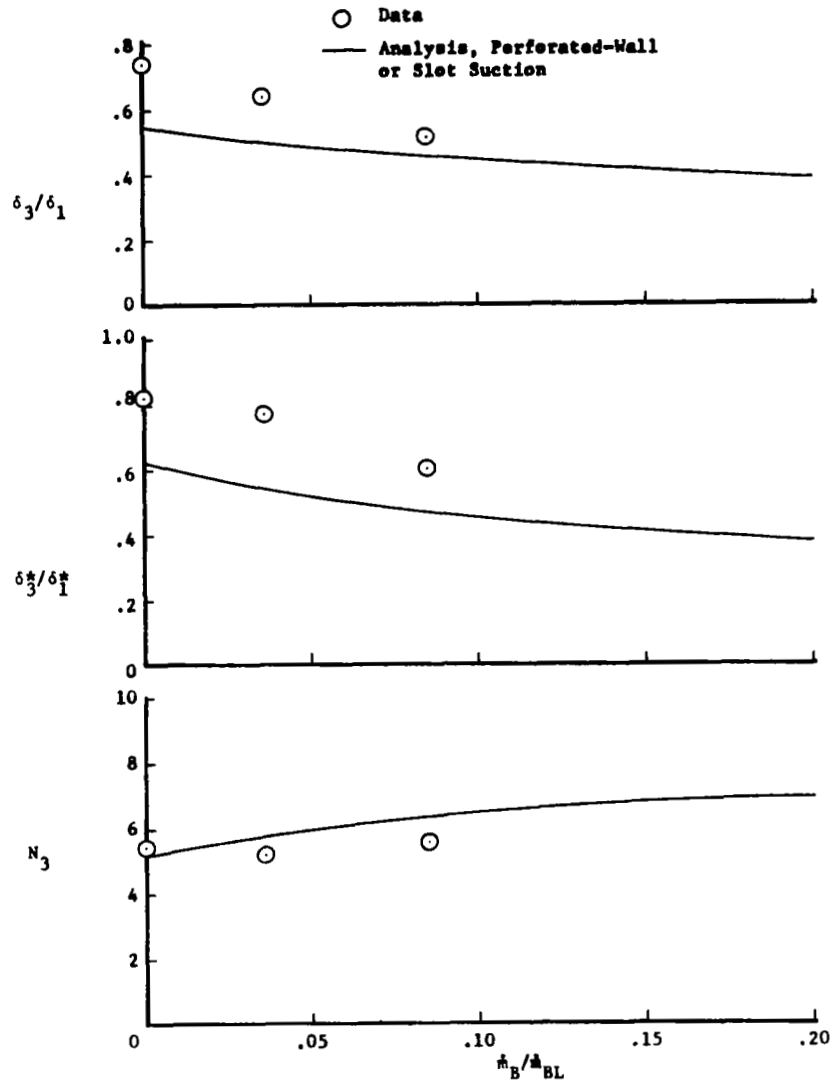

Figure 73. Comparison of Analysis and Data for Axially Symmetric Interactions with Suction, 10-Degree Cone at M_∞ = 3.78.

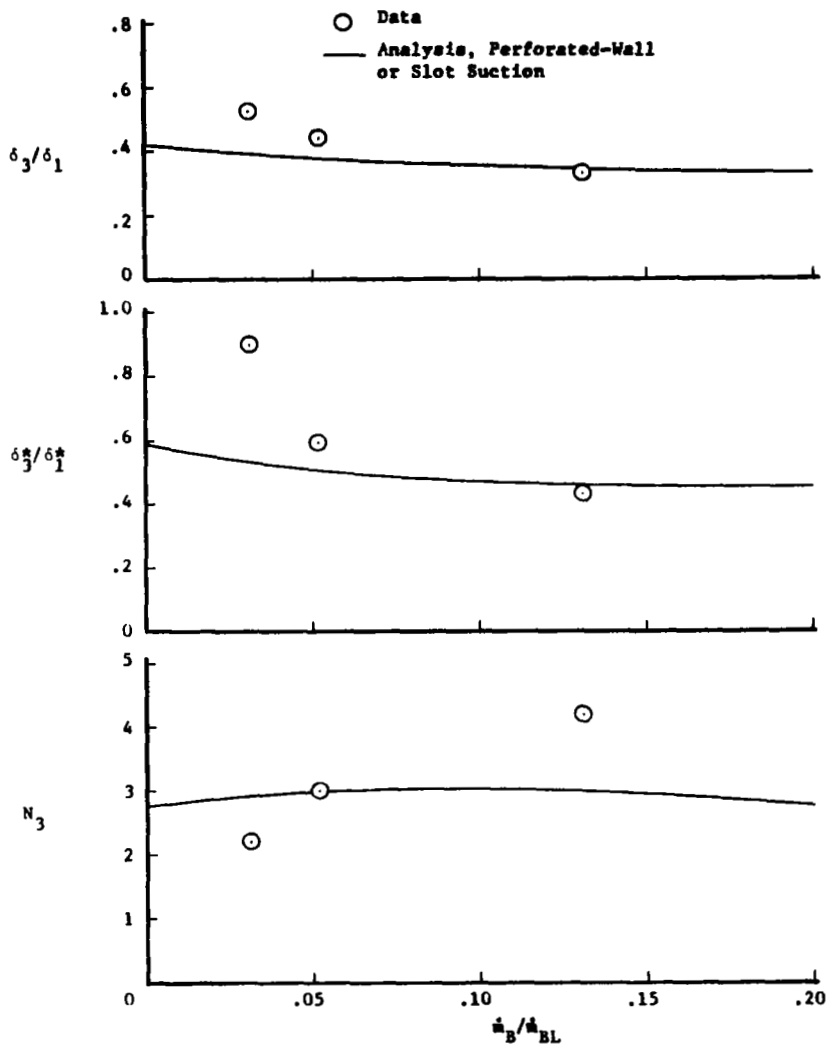

Figure 74. Comparison of Analysis and Data for Axially Symmetric Interactions with Suction, 15-Degree Cone at M_∞ = 3.78.